McGill

Quantitative Magnetization Transfer Evaluation of the Knee Joint in Magnetic Resonance Imaging

Mikaël Simard

Medical Physics Unit

McGill University, Montreal

August, 2016

A thesis submitted to McGill University in partial fulfillment of the requirements of the degree of Master of Science.

Abstract

QUANTITATIVE magnetization transfer (QMT) imaging is a quantitative magnetic resonance imaging technique that can probe the macromolecular content of tissues. It does so by providing estimates of model parameters that describe the process of magnetization transfer between the semi-solid pool of protons in macromolecules and free protons in water, as well as the characteristics of these proton populations. QMT has been useful in the study of neurodegenerative disease, as it can detect macromolecular degeneration. Because QMT can detect changes in the macromolecular content of tissues, QMT is a promising potential biomarker of early knee osteoarthritis (OA), as macromolecular degeneration is the hallmark of early OA. This thesis presents an adaptation of the QMT framework to cartilage tissues, and a QMT analysis in 4 knee cadaver specimens. We report the first QMT analysis of knee meniscus, and demonstrate that the excision of menisci and immersion before re-scanning has a significant impact on the restricted pool fraction and T_1 relaxation time of the free pool. The QMT analysis of articular cartilage provided QMT parameters similar to previously published studies. A methodology to optimize sequence parameters in MT acquisitions for future studies is also presented.

Résumé

L'IMAGERIE par transfert de magnétisation quantitatif (TMQ) est une méthode quantitative d'imagerie par résonance magnétique qui peut sonder le contenu macromoléculaire des tissus. Ceci est accompli en fournissant des estimés de paramètres d'un modèle qui décrit le processus du transfert de magnétisation entre le réservoir semi-solide de protons dans les macromolécules avec les protons libres dans l'eau, en plus des caractéristiques de ces populations de protons. Le TMQ a été utile pour l'étude des maladies neurodégénératives considérant qu'il peut détecter la dégénérescence macromoléculaire. Étant donné que le TMQ peut détecter des changements dans le contenu macromoléculaire des tissus, celui-ci est un biomarqueur potentiel prometteur pour l'ostéoarthrose (OA) précoce des genoux, puisque la dégénérescence macromoléculaire est une caractéristique principale de l'OA précoce. Ce mémoire présente une adaptation du cadre de TMQ pour des tissus cartilagineux, ainsi qu'une analyse de TMQ dans 4 genoux de cadavres. Nous rapportons la première analyse de TMQ des ménisques des genoux et démontrons que l'excision des ménisques ainsi que l'immersion avant l'imagerie produit un impact significatif sur la fraction macromoléculaire et le temps de relaxation T_1 du réservoir de protons libres. L'analyse TMQ du cartilage articulaire a fourni des paramètres de TMQ similaires aux études antérieures publiées sur le sujet. Une méthodologie pour l'optimisation des paramètres de la séquence d'IRM pour les acquisitions de données en TM pour de futures études est également présentée.

Acknowledgements

I am grateful to many people who have helped me to make this thesis possible. Emily McWalter for sharing her expertise on the disease of osteoarthritis and quantitative MRI in musculoskeletal systems, as well as for the contouring of meniscus data and providing invaluable feedback on my work ; Marianne Black for the contouring of cartilage regions, and my colleagues Véronique Fortier, Zaki Ahmed and Stella Xing for useful discussions. I would also like to acknowledge the contributions of Marcus Alley for the SPGR pulse sequence used in this work, Braggi Sveinson for the method to map the B1 field, as well as John Sled and Bruce Pike for supplying the original code from which the analysis software was derived.

I am extremely grateful to my supervisor, Ives Levesque, for his inestimable mentorship throughout the project. The two years during which we collaborated helped me to become an overall better physicist and scientist.

I also acknowledge fellowship support from the Fonds de recherche sur la nature et les technologies (FQRNT), the Natural Sciences and Engineering Research Council (NSERC) and partial support by the CREATE Medical Physics Research Training Network grant of the NSERC.

Contribution of the authors

This thesis includes the contribution of multiple authors, notably for chapter 4, which is written in the form of a manuscript to be submitted to the journal *Magnetic Resonance in Medicine*. I have written chapters 1, 2, 3, 5, 6 as well as the appendices, with review and contributions by Ives Levesque.

The contributions of various authors for chapter 4 are listed as follows.

As the first author of the study, I implemented and validated the methodology to analyze the acquired MRI data. I performed the data analysis and drafted the paper.

Contributions of the co-authors :

Emily J. McWalter : co-designed the study, performed all data acquisition and tissue extractions, segmented the data into regions of interest, and reviewed the manuscript.

Garry E. Gold : co-designed the study and reviewed the manuscript.

Ives R. Levesque : As the candidate's supervisor, Prof. Levesque provided essential guidance and mentorship through the project, co-designed the study, implemented the image acquisition methods, contributed to the data acquisition and analysis, and reviewed the manuscript.

Table of Contents

List of Figures

List of Tables

1 Introduction

Magnetic resonance imaging (MRI) is a non-invasive technique that can be used clinically to assess articular cartilage damage, joint morphology changes and meniscal tears. This is useful specifically for the diagnosis of osteoarthritis (OA), a degenerative joint disease that leads to joint pain, stiffness and loss of function in weight-bearing joints such as the knee and is characterized by the loss and erosion of articular cartilage and menisci degradation.

However, these macroscopic degenerative changes are absent in early stages of the disease, and conventional MRI cannot be used for the prevention or early diagnosis of OA. Early OA is characterized by changes in the macromolecular structure (collagen and proteoglycans) of cartilage. Thus, there is significant interest to develop techniques that can measure macromolecular changes in articular cartilage for the early diagnosis of OA, as well as for monitoring and evaluating the progress of therapies to control joint tissue degradation. Probing the microstructure and composition of joint tissues with MRI can be challenging : macromolecules such as collagen and proteoglycans have very short T_2 relaxation times owing to bound protons in the macromolecules, making their direct observation difficult.

Quantitative magnetization transfer (QMT) MRI is a technique that can probe the macromolecular content of tissues by exploiting to the exchange of magnetization between the semi-solid pool of protons contained in macromolecules, and the free pool of protons in mobile water. The exchange occurs mainly through dipolar interactions (otherwise known as the nuclear Overhauser effect) and proton chemical exchange. The tissue components can be characterized with physically meaningful parameters related to the MT

effect. Hence, QMT is an interesting candidate as a potential biomarker of early joint tissue degeneration, the hallmark of early OA.

For QMT metrics to be used as biomarkers of early joint tissue degeneration, comparisons with histology and biochemical markers must be carried out. Whole cadaveric knee specimens can be used to correlate quantitative MRI with biochemical and histological markers. To carry out these analyses, tissues of interest are extracted from the knee sample, and scanned in hydrogen-free fluids. As such, a first step for the validation of QMT metrics consists of quantifying the impact of extracting and conserving joint tissues, as histology and biochemical studies are performed with extracted tissues (*ex situ*), while the QMT analysis will ultimately be performed *in situ*. Our hypothesis was that measuring QMT model parameters *in situ* or *ex situ* would yield the same parameters.

The main objectives of this thesis were : 1) to develop a feasible method for evaluation of MT model parameters in the whole knee joint, 2) to perform initial measurements of QMT parameters of meniscus using this technique, 3) to perform measurements *in situ* and *ex situ* to evaluate the impact of extraction and conservation using 4 knee specimens, and 4) to evaluate MT parameters in cartilage and compare these with published studies. The menisci were the main target of this work, as they might degenerate in early OA, and the QMT properties of this tissue have yet to be reported.

Background information on MRI, OA, and MT imaging is provided in chapter 2. Because QMT has been typically done in brain, the first objective was to establish a QMT processing framework adapted to joint tissues. In chapter 3, this adapted framework for soft tissues of the knee joint is presented and characterized. In chapter 4, we present, in the form of a manuscript, the QMT analysis of 4 cadaveric knee specimens and a comparison of measurements between *in situ* and *ex situ* menisci. We demonstrate, in chapter 5, how the data acquisition scheme can be improved and optimized for cartilage and meniscus data and suggest improvements to the QMT framework to guide future

studies in cartilage and meniscus towards the early diagnosis of OA.

The problem of optimizing the acquisition scheme is nonlinear and requires estimates of QMT parameters in the tissues of interest as an input. Therefore, the optimization cannot be performed before doing initial scans to obtain MT parameters. To the best of our knowledge, MT parameters in the meniscus have not been reported in the literature. Therefore, the measurements performed in chapter 4 are used as an input to optimize the acquisition scheme in chapter 5.

2 Background

2.1 Basics of Magnetic Resonance Imaging

2.1.1 Origin of the MRI signal

Basic MRI concepts and the broad description of MT can be understood with classical arguments, although a rigorous description requires quantum mechanics. Most ideas in this work are derived from classical notions, but quantum mechanical considerations are frequently used to provide a deeper understanding of concepts. The following review is based on the work of Brown *et al.* [2] and C.P. Slichter [8]. Bold variables represent vectors.

The main idea behind MRI is to extract information on a given material (e.g. the human body) by exploiting the nonzero intrinsic angular momentum (*spin*) $\boldsymbol{S}$ that arises from nuclei with odd numbers of protons and/or neutrons. The most commonly used nucleus in MRI is the hydrogen proton, ^{1}H, although ^{23}Na and ^{31}P are also naturally abundant enough to be probed. From the nonzero spin of such nuclei arises a magnetic dipole moment $\boldsymbol{\mu}$ related to the spin through the relationship

$$\boldsymbol{\mu} = \gamma \boldsymbol{S} \tag{2.1}$$

where γ is the gyromagnetic ratio, and $\gamma/2\pi$ is equal to 42.58 MHz/Tesla for hydrogen nuclei. In the context of NMR and MRI, we do not consider each proton separately but rather an ensemble of protons, in order to use macroscopic quantities. Consider a microscopic volume V that contains a large number of protons. The magnetization vector,

$\boldsymbol{M}$, is defined as the sum of each magnetic moment normalized by the volume, that is

$$\boldsymbol{M} = \frac{1}{V} \sum_{\text{i : protons} \in \text{V}} \boldsymbol{\mu_i} \tag{2.2}$$

The set of spins (or protons) in V is called a spin isochromat and represents a collection of spins that resonate at the same frequency. Within a MRI voxel, there can be many spin isochromats. The net magnetization $\boldsymbol{M}$ is used to describe the effect of magnetic fields on the ensemble of spins. Without the presence of a magnetic field, the protons in an isochromat are randomly aligned due to thermal motion and their magnetic dipole moments $\boldsymbol{\mu_i}$ cancel each other out. As a result, $\boldsymbol{M}$ will be zero.

To obtain a nonzero magnetization, a magnetic field $\boldsymbol{B_0}$ is applied. In this situation, an isochromat is described as an aggregate of protons that experience the same magnetic field. In the presence of $\boldsymbol{B_0}$, each nuclear dipole can take different quantized orientations (spin states) with respect to $\boldsymbol{B_0}$. These orientations correspond to various energy levels and in the case of the ^{1}H nuclei of spin $s = 1/2$, the number of possible orientations is $2s + 1 = 2$, and can be represented as parallel and antiparallel to the axis of $\boldsymbol{B_0}$. At a given temperature T, the ratio of the number of parallel to antiparallel spins depends on field strength and can be modelled by the Boltzmann distribution :

$$\frac{N_\uparrow}{N_\downarrow} = \exp\left(-\frac{\gamma B_0 \hbar}{k_B T}\right) \tag{2.3}$$

The ratio depends on the relative importance of difference in the magnetic energy between the two quantum states, $\gamma B_0 \hbar$ (where $\hbar$ is the reduced Planck constant) and the thermal energy $k_B T$, where k_B is Boltzmann's constant. For typical MRI fields (1.5 to 3 T) at room temperature (295 K), there is a small excess (a few parts per million) of spins in the lower energy state, which results in the net magnetization of the voxel. Although this is a small proportion, the large number of nuclei in the human body will overall give rise to a measurable magnetization, which is at the origin of the MRI signal.

Classically, the motion of a spin can be represented by a microscopic magnet in an external field $\boldsymbol{B_0}$ and is described by the equation of motion :

$$\frac{d\boldsymbol{\mu}}{dt} = \boldsymbol{\mu} \times \gamma \boldsymbol{B_0} \tag{2.4}$$

Equation 2.4 describes the net torque on a magnetic dipole in a constant magnetic field. By considering an isochromat (summing over all magnetic moments, thus using the magnetization vector) and neglecting any interaction between the spins, one can obtain the most basic form of the Bloch equation, which describes how the magnetization of a sample evolves in the presence of a static magnetic field $\boldsymbol{B_0}$:

$$\frac{d\boldsymbol{M}}{dt} = \boldsymbol{M} \times \gamma \boldsymbol{B_0} \tag{2.5}$$

The solution to this set of differential equations is a motion of precession of $\boldsymbol{M}$ around the axis of $\boldsymbol{B_0}$ at the so-called Larmor frequency $\omega_0 = \gamma B_0$. By convention, $\boldsymbol{B_0}$ is applied along the z-axis, and the resulting time-varying magnetization vector is aligned along the z axis and precessing in the $x - y$ plane. This precession movement can be detected with a coil orthogonal to the transverse plane : the rotating magnetic field created by the precession of $\boldsymbol{M}$ can induce an electric current in the coil by Faraday induction. The induced signal oscillates at the Larmor frequency. Regions with a higher density of protons will have a larger $\boldsymbol{M}$ leading to a stronger signal in the coil. Figure 2.1 represents schematically the creation of $\boldsymbol{M}$ as well as the detection of the signal.

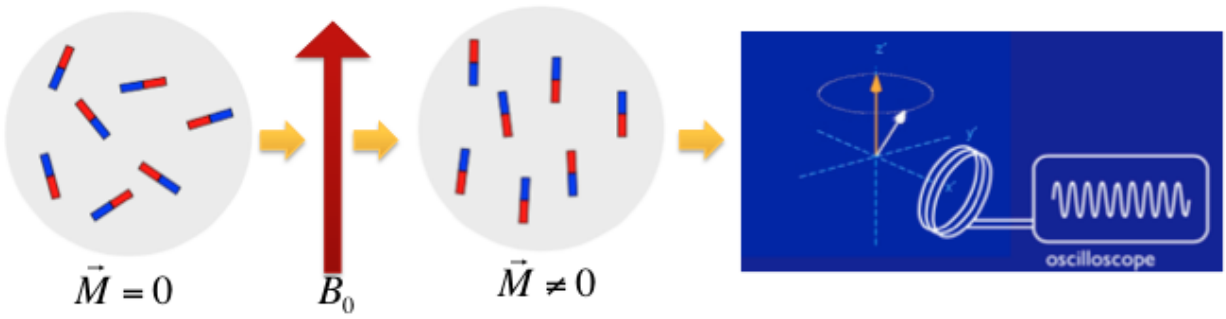

Figure 2.1 – Representation of ^{1}H nuclei in a sample a) before and b) after the application of $\boldsymbol{B_0}$. The resulting precession is shown in c), with the detection coil. Adapted from [1].

2.1.2 Excitation

The amplitude of the detected signal depends on components of $\boldsymbol{M}$ in the x-y plane, which is zero when only B_0 is applied along the z-axis. To maximize the signal and probe the sample adequately, the magnetization vector must be tipped towards the $x-y$ plane by applying a second magnetic field of lower intensity, $\boldsymbol{B_1}(t)$. Following the previously established equation of motion for $\boldsymbol{M}$ in the presence of a magnetic field, the use of another field in the transverse plane will tip the magnetization towards the $x-y$ plane. The effect is maximized when the $\boldsymbol{B_1}$ field is time-varying at the frequency ω, and is tuned to the Larmor frequency ($\omega = \omega_0$). The nutation of $\boldsymbol{M}$ after the application of the $\boldsymbol{B_1}$ pulse (called the excitation pulse) is schematically represented in figure 2.2.

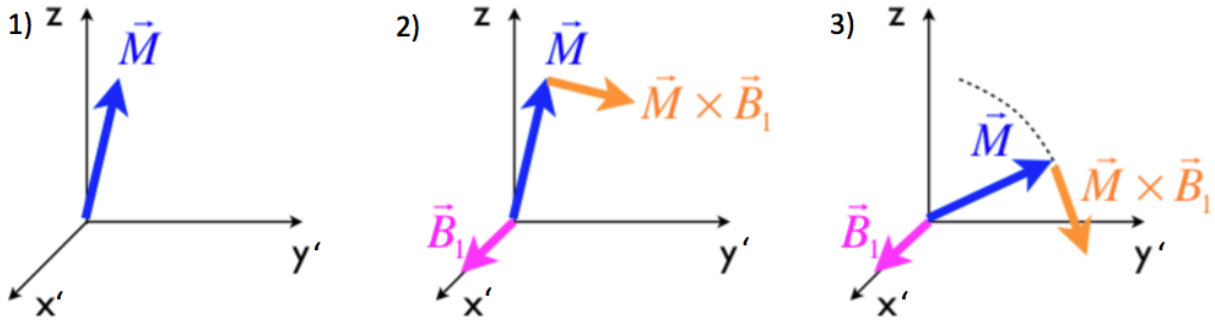

Figure 2.2 – Representation of the nutation of $\boldsymbol{M}$, shown in a frame of reference rotating at ω_0 around the z axis. 1) Magnetization vector precessing with frequency ω_0 after the application of B_0. In 2), $\boldsymbol{B_1}(t)$ is applied at the Larmor frequency, and then 3) the magnetization vector is tipped towards the transverse plane.

The tip angle α, defined as the angle between the z-axis and the magnetization vector after the application of $\boldsymbol{B_1}$, can be obtained from equation 2.6 :

$$\alpha = \gamma \int_0^\tau B_1(t)dt \tag{2.6}$$

Where τ is the duration of the pulse, and here $\boldsymbol{B_1}(t)$ is the envelope of the pulse. Increasing the tip angle up to 90° by either increasing the pulse duration τ or the pulse amplitude will provide a higher signal, but at the cost of a longer acquisition time. Additionally, the amplitude of $\boldsymbol{B_1}(t)$ cannot be arbitrarily high for RF power deposition concerns in the human body. As we will see in section 2.2, in magnetization transfer imaging, MT

preparation $\boldsymbol{B_1}$ pulses are often applied off-resonance ($\omega \neq \omega_0$) and at high pulse power or duration to maximize the MT effect. In this situation, there are more often specific absorption rate (SAR) concerns. The excitation step has two main effects : the spins are tipped in the $x - y$ plane and are set in phase, which leads to a precessing transverse magnetization around the axis of $\boldsymbol{B_0}$.

2.1.3 Relaxation mechanisms

After the $\boldsymbol{B_1}$ field is applied, the magnetization vector will return to its initial state through relaxation processes. There are two distinct relaxation mechanisms :

— Longitudinal, or T_1 relaxation : the re-orientation of the spins along the axis of $\boldsymbol{B_0}$ leading to a recovery of the z component of $\boldsymbol{M}$ towards its initial value M_0 ;

— Transverse, or T_2 relaxation : related to the interaction between the spins giving rise to phase shifts and a loss of transverse coherence, which leads to the decay of the $x - y$ component of $\boldsymbol{M}$.

In longitudinal relaxation, the spins re-align with the external field by exchanging energy with the surrounding lattice. The rate of change of the longitudinal magnetization, $dM_z(t)/dt$, is proportional to the difference $M_0 - M_z(t)$, with an empirically determined proportionality rate constant $R_1 \equiv 1/T_1$:

$$\frac{dM_z(t)}{dt} = \frac{1}{T_1}\left(M_0 - M_z\right) \tag{2.7}$$

The constant T_1 is the spin-lattice relaxation time, typically ranging from hundreds of milliseconds to a few seconds in human tissue. T_1 depends on the amplitude of $\boldsymbol{B_0}$ and varies with the type of tissue. The solution to equation 2.7 is of the form

$$M_z(t) = M_z(0)e^{-\frac{t}{T_1}} + M_0\left(1 - e^{-\frac{t}{T_1}}\right) \tag{2.8}$$

and is characterized by an exponential recovery of M_z towards M_0. Here, $M_z(0)$ is defined as the initial value of the longitudinal magnetization.

The transverse magnetization, often expressed as $M_{xy} = M_x + iM_y$, decays through spin-spin relaxation. The spins will individually experience a local magnetic field that is the vectorial sum of the applied field $\boldsymbol{B_0}$ and the dipolar fields $\boldsymbol{B_D}$ produced by all neighbouring spins. Each spin will thus experience an effective (and different) magnetic field $\boldsymbol{B} = \boldsymbol{B_0} + \boldsymbol{B_D}$. As the precession frequency is a function of the local magnetic field, individual spins will precess at different speeds and tend to fan out with time, leading to dephasing and a loss of coherence with each other. The transverse magnetization vector tends towards zero as the spins lose coherence in the transverse plane. The fanning out is schematically shown in figure 2.3.

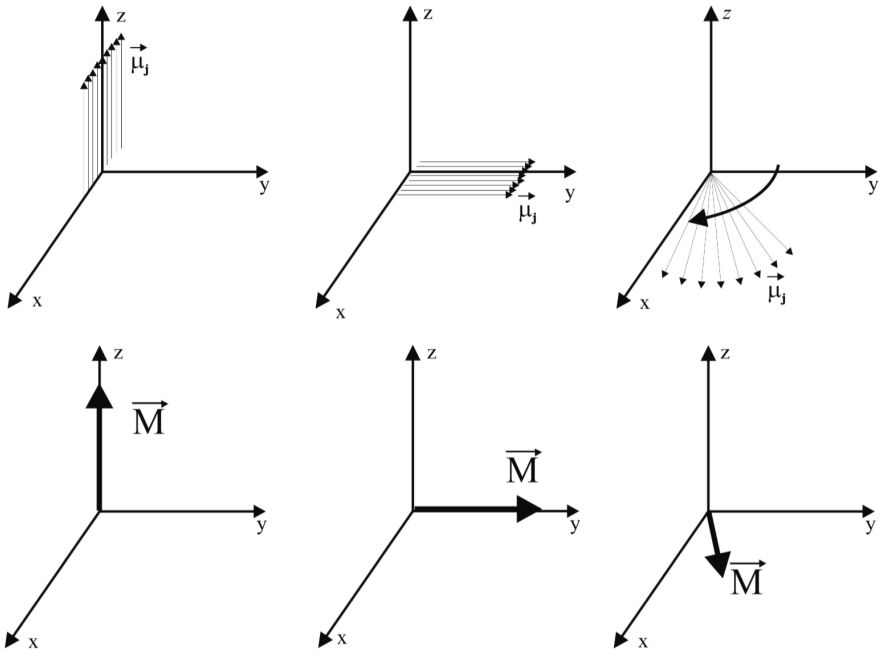

Figure 2.3 – Transverse relaxation of the magnetization, shown in the laboratory frame of reference. The set of spins are tipped towards the x-y plane with a 90° pulse, and start to fan out because of the interaction between spins. The resulting magnetization vector in the x-y plane reduces as the spins lose coherence (from [2]).

The decay of M_{xy} can be described empirically with the introduction of the T_2 relaxation time, which leads to an exponential decay of M_{xy} :

$$\frac{dM_{xy}(t)}{dt} = -\frac{M_{xy}}{T_2} \Rightarrow M_{xy}(t) = M_{xy}(0)e^{-t/T_2} \tag{2.9}$$

Because the detected signal in MRI depends on the amplitude of the transverse magnetization, T_2 relaxation influences the signal and contrast obtainable in MRI. In MRI, the pre-

sence of B_0 field inhomogeneities, caused by imperfect instrumentation and susceptibility-induced distortions of the magnetic field by tissues, leads to additional dephasing of M_{xy}, which translates into a different relaxation time T_2^*. Attributing the effect of the field inhomogeneities to a separate relaxation time T_2', the shorter total relaxation time, T_2^*, can be defined as

$$\frac{1}{T_2^*} = \frac{1}{T_2} + \frac{1}{T_2'} \tag{2.10}$$

The loss of M_{xy} due to T_2' can be recovered in specific MRI sequences. Therefore, MRI can be weighted either in T_2 or T_2^* depending on the sequence.

The basic signal detected in NMR, the free induction decay (FID), has an amplitude that decays with the relaxation time T2*. Current MRI hardware can record FIDs with associated T2 in the order of milliseconds. Mobile protons, usually associated with water in the human body, have transverse relaxation times in the order of tens to hundreds of milliseconds [2] and are the main source of the signal in MRI. Typically, the detected signal in MRI comes from these mobile protons, with $T_2 > 10$ ms [9].

The transverse relaxation time T_2 is on the order of tens of milliseconds for most human tissues and also depends on B_0, although less importantly than T_1. The relaxation time T_1 is larger or equal to T_2 : this is reflected in the Bloembergen-Purcell-Pound (BPP) theory of relaxation [8, 10]. Both relaxation mechanisms are depicted in figure 2.4.

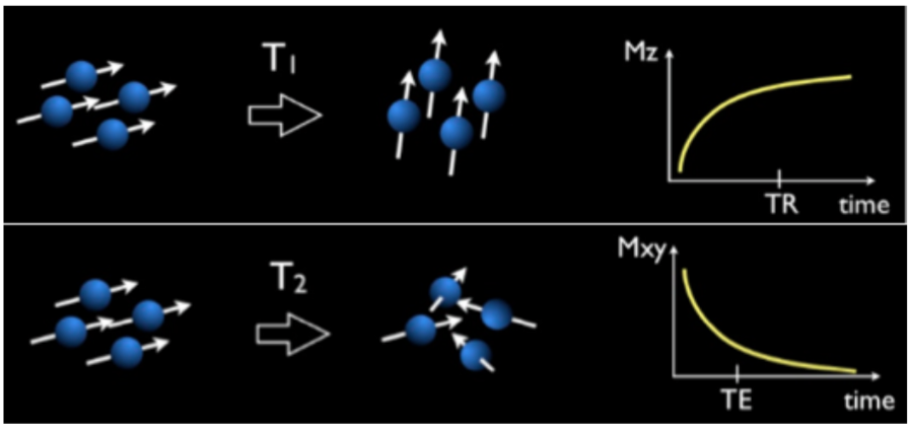

Figure 2.4 – Longitudinal (top) and transverse (bottom) relaxation mechanisms with the associated recovery and decay curves of the magnetization vector. Adapted from [1].

The complete Bloch equations taking in account the relaxation mechanisms can be expressed by combining equations 2.4, 2.7 and 2.9 :

$$\frac{d\boldsymbol{M}(t)}{dt} = \boldsymbol{M} \times \gamma \boldsymbol{B_{ext}} + \frac{M_0 - M_z}{T_1}\hat{\boldsymbol{z}} - \frac{M_x\hat{\boldsymbol{x}} + M_y\hat{\boldsymbol{y}}}{T_2} \tag{2.11}$$

The external field $\boldsymbol{B_ext}$ field is the combination of the B_0 and B_1 fields. Conventionally, the B_0 field is static in time and oriented along the z-axis and the B_1 field is time-dependent and along the x'-axis, giving a total external field :

$$\boldsymbol{B_{ext}} = B_0\hat{\boldsymbol{z}} + B_1(t)\hat{\boldsymbol{x}} \tag{2.12}$$

In the case of MT, we will revisit the Bloch equations with additional complexity. The B_1 field can be off-resonance and magnetization transfer terms between different pools of protons will be considered as additional mechanisms that can influence the magnetization.

In practice, the relaxation in simple materials and pure substances is accurately described by the presented T_1 and T_2 relaxation mechanisms. A more complete and less phenomenological approach to relaxation in simple substances is the BPP theory of relaxation, which states that relaxation mechanisms are dominated by dipolar interactions between spins and takes in account the tumbling motion of molecules in local field inhomogeneities [10]. Additionally, in more complex environments such as the human body, ^{1}H relaxation is more convoluted - there are multiple molecular environments where protons reside (different physical compartments, and within membranes, proteins, lipids, etc.) and the protons from different environment can interact with each other. These protons in different environment can have different associated T_1 and T_2.

The previous sections have covered how to excite an ensemble of spins in a sample and detect its signal. In MRI, additional steps of spatial and phase encoding with the use of magnetic field gradients can encode the localization of spins in a given sample to reconstruct an image, which is typically done with Fourier transforms. By applying magnetic

field gradients, one can incorporate spatial dependence of the Larmor frequency of isochromats in a given sample and selectively excite different regions of a sample. More details on imaging methods and the derivation of a signal equation relating the measured raw data with the spatial distribution of magnetization can be obtained elsewhere [2]. Further details on the spatial encoding process are omitted here for brevity and focus.

Before exploring the concept of magnetization transfer, we establish quantitative imaging tools that are required to perform quantitative magnetization transfer imaging, namely B_1 and T_1 mapping techniques.

2.1.4 B_1 mapping

Quantitative MRI techniques such as QMT fit models to data and extract meaningful quantitative parameters. This can be done on a voxel-wise basis to produce quantitative parameter maps. In many models, accurate knowledge of the excitation flip angle, α, must be included in the expression being fitted. An example is given in section 2.1.5 where the equation that describes the signal in variable flip angle T_1 mapping experiments (equation 2.17) includes this parameter.

There are B_1 field inhomogeneities present in MRI at 3.0 T that leads to a non-homogeneous distribution of flip angles α in an acquired volume, following equation 2.6. In other words, at a given voxel, the prescribed flip angle α_p at the scanner might differ from the true angle α due to inhomogeneities. As such, in quantitative experiments where the value of the flip angle must be known precisely to allow an unbiased estimation of quantitative parameters, B_1 mapping, i.e. estimating the value of $|B_1|$ or α at each voxel might be required. This is the case in QMT and variable flip angle T_1 mapping.

For B_1 mapping, we present briefly the method used in this work, the double angle (DA) mapping technique [11]. There are other B_1 mapping techniques each with their own advantages, such as the Bloch-Siegert method [12]. In the double angle method, two

gradient-echo acquisitions are obtained, each with different flip angles α_1 and α_2. Voxel-wise, the signal obtained in each gradient echo acquisition for this purpose can essentially be represented by

$$S_i = A \sin(\alpha_i), \mathrm{i} = \{1, 2\}. \tag{2.13}$$

where A is a proportionality constant that includes terms such as T_2 relaxation and proton density, and is estimated to be the same in the two acquisitions. By taking $\alpha_2 = 2\alpha_1$ (hence the name double angle), the ratio of the signals becomes

$$\frac{S_1}{S_2} = \frac{A \sin(\alpha_1)}{A \sin(\alpha_2)} = \frac{\sin(\alpha_1)}{2 \sin(\alpha_1) \cos(\alpha_1)} = \frac{1}{2 \cos(\alpha_1)} \tag{2.14}$$

The flip angle α_1 can then be estimated as

$$\alpha_1 = \cos^{-1}\left(\frac{S_2}{2S_1}\right) \tag{2.15}$$

This flip angle, α_1, is not necessarily equal to the prescribed angle, α_p, on the MRI scanner, and is taken as an estimation of the real flip angle α. Typically, a multiplicative constant correction map

$$\kappa = \frac{\alpha_1}{\alpha_p} \tag{2.16}$$

is calculated from the measured angle α_1 and the prescribed angle α_p and is used to correct the flip angle in other acquisitions. In QMT experiments, the prescribed angle is multiplied voxel-wise by the value of κ to use a more precise estimate of the flip angle that accounts for inhomogeneities. In this work, we used $\alpha_1 = 60^\circ$ ($\alpha_2 = 120^\circ$) in the dual angle measurement, as the gradient of equation 2.14 is higher for large values of α_1 : small differences in the signals S_1 and S_2 translate to a larger variation of α_1 as the value of the prescribed angle increases.

2.1.5 T_1 mapping

In QMT, an independent measurement of T_1 is required in addition to the MT-weighted data, as will be detailed in section 2.2.3. We describe the approach used in this work for

T_1 mapping.

There are multiple techniques for T_1 mapping such as the inversion recovery (IR) sequence, the Look-Locker technique and the variable flip angle (VFA) approach. While the IR sequence is considered as the gold standard, we use the VFA technique (specifically DESPOT1), detailed in [13] for its simplicity and shorter scan times than the IR approach.

Throughout this document, the T_1 value obtained from a VFA experiment is referred to as T_{1obs}, the observed (or apparent) T_1, to clearly establish a difference between the observed T_1 from T_1 mapping experiments and the T_1 values specific to pools of protons described in MT. The VFA approach can be affected by magnetization transfer effects which influence T_1 values obtained from the fitting procedure. This is discussed more in details in chapter 3.

The method described here is a brief summary of Deoni's method detailed elsewhere [13]. In VFA experiments, a series of gradient recalled-echo (SPGR) images are acquired over a range of flip angles α using a constant repetition time TR.

The signal S in VFA experiments, which depends on the flip angle, the proton density M_0 and the relaxation time T_{1obs}, is described by the Ernst equation [14] :

$$S\left(\alpha, t = TR, M_0, T_{1obs}\right) = \frac{M_0\left(1 - E_1\right)\sin\left(\alpha\right)}{1 - E_1\cos\left(\alpha\right)} \tag{2.17}$$

Where E_1 is defined as $\exp\left(-{}^{TR}/_{T_{1obs}}\right)$. In this work, four volumes with angles $\alpha = 5, 10, 20$ and 30° are acquired. Voxel-wise, M_0 and T_{1obs} can then be fitted from the four signal values (at different flip angles) either with a nonlinear least squares approach or by linearizing equation 2.17 and evaluating the slope, proportional to T_{1obs}. The linearized approach, described in [13], was used in this work. We also corrected the flip angles with the B_1 mapping technique described previously.

2.2 Magnetization Transfer

2.2.1 Introduction to MT

The phenomenon of magnetization transfer (MT), or cross-relaxation, which can be observed in magnetic resonance experiments, can be broadly described as the exchange of magnetization between spins in two (or more) distinct environments through a combination of processes of chemical exchange and dipolar interactions.

More specifically, in the context of MRI and in vivo imaging, we are interested in the exchange between two types of protons in human tissue : protons residing in the free pool, and others in the semi-solid pool (also called the restricted or bound pool). The free pool consists of protons on mobile and free water molecules, which contributes to traditional MRI signal, and the semi-solid pool is composed of protons more tightly bound to other molecules (not water) in human tissue. These semi-solid protons are found in protein matrices, cell membranes and macromolecules such as collagen. The protons in the semi-solid pool experience a reduced rotational mobility, similarly to a gel or solid, which leads to longer correlation times between spins, and corresponding longer T_1 and shorter T_2 relaxation times, as described by the Bloemberg-Purcell-Pound theory of relaxation in NMR [10]. The T_2 relaxation time of the semi-solid pool is in the order of microseconds, meaning that the ensemble of spins in the semi-solid pool of protons loses its coherence too quickly to be imaged directly with most MRI techniques. As such, this restricted component of tissues is MRI-invisible when imaged with conventional sequences.

The restricted pool of protons is understood to be composed of protons attached to the various macromolecules present in biological tissue, such as cholesterol and collagen [15]. The macromolecules of interest are typically larger than water molecules, with enough hydrogen to produce net magnetization. In the context of MT, it is important to note that the relevant macromolecules are fixed in the matrix of biological structures, such as

cellular membranes. Indeed, it is widely reported that cross-linking between macromolecules (*i.e.* any covalent or ionic bond that ties polymeric chains together) is necessary to produce the MT effects investigated in this work [15], [16]. Therefore, the molecules that participate to MT are better described as the restricted pool. In human tissues, we consider the aggregate effects of the cross-linked macromolecules that are involved in MT.

Probing the semi-solid pool of protons is of interest, as it contains information about the restricted component of tissues. By taking advantage of MT between the free and semi-solid pools, one can indirectly infer the properties of the semi-solid pool through its effect on the free pool. MT contrast imaging is a MRI technique that generates contrast based on the amount of MT in a given voxel and allows indirect imaging of the semi-solid pool of protons.

MT quantification in tissue has been shown in literature to improve, for example, the characterization of the pathologically heterogeneous lesions of multiple sclerosis (MS) by providing a measure of demyelination [17]. It is also a promising technique for the early diagnosis of cartilage degeneration diseases such as osteoarthritis (OA), which is currently diagnosed in late stages of the disease, most often in the knee [6, 7]. MT MRI is currently at an intensive research stage and promises to be an excellent way to demonstrate the potential of MRI in probing macromolecular degeneration that occurs in diseases such as MS and OA.

2.2.2 A qualitative interpretation of MT

The two pools of protons can exchange magnetization via chemical exchange and dipolar interactions (the nuclear Overhauser effect). Chemical exchange is related to the physical motion of spins or molecules that is caused by chemical interactions. The nuclear Overhauser effect is a proximity effect - when spins are in proximity, their magnetization can be exchanged through space, without the need for a chemical bond.

Here, we establish how to obtain MT weighted images in a MRI experiment. The contrast in such images is based on the amount of MT that occurs between the two pools in each voxel, as well as on the relative size of each pools and their respective relaxation properties.

The differences between both proton pools can first be highlighted in terms of their respective absorption lineshapes, which reflects how much energy can be transferred from the magnetic field to the magnetization vector as a function of the frequency of the magnetic field. The higher the amplitude of the lineshape at a given frequency, the more saturated the pool becomes : the z component of its magnetization vector is reduced.

Free protons, which are accurately described by the Bloch equations 2.11, can be shown to have a narrow, Lorentzian-shaped absorption spectrum, centered at the Larmor frequency ω_0. The pool thus absorbs electromagnetic radiation only close to ω_0. Semi-solid protons, being less mobile, will interact for a longer time with each other, leading to a wider absorption spectrum. The two pools and their associated absorption spectra are represented in figure 2.5.

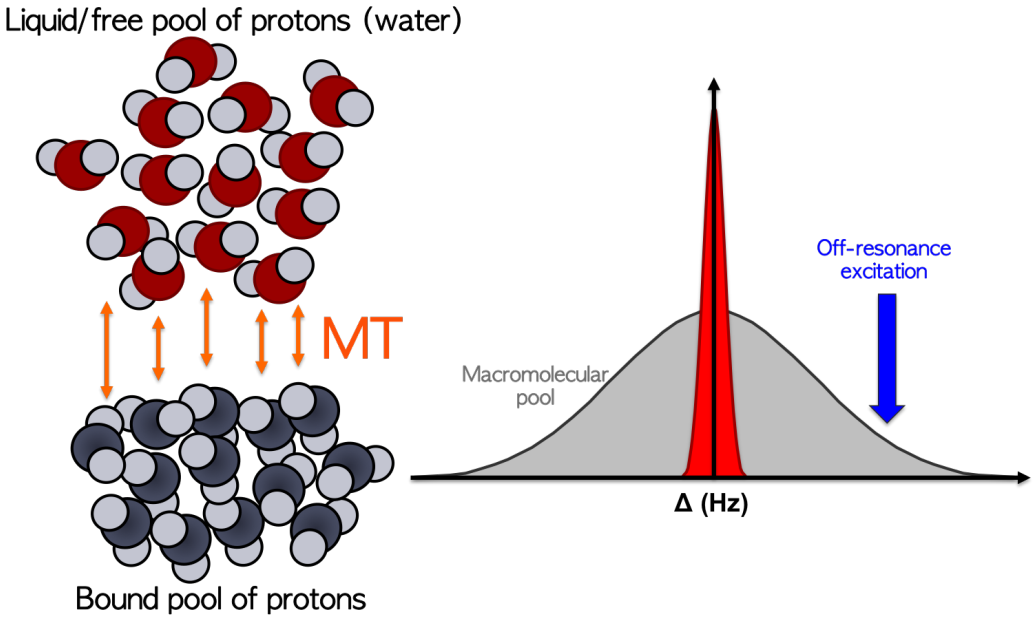

Figure 2.5 – Semi-solid and free pools of protons in human tissue and their associated absorption lineshapes. The linewidths are tens of Hz for the free pool and tens to a hundred of kHz for the semi-solid pool [3]. The linewidth of the free pool is greatly exaggerated for illustrative purposes.

An MRI sequence using an excitation pulse at the Larmor frequency (on resonance) can saturate both pools, but only the free pool is detected, as the other decays too quickly. Here, MT occurs when using on resonance pulses, but the effect is small : to obtain noticeable MT, sequences with high power pulses and short repetition times (TR) can be used.

An excitation pulse that is produced off-resonance, at a given offset frequency $\Delta = \omega - \omega_0$ (as depicted in blue in figure 2.5), will preferentially saturate the semi-solid pool due to the respective linewidths of each pool, while having a much smaller effect on the free pool. From this, one can create a simple experiment to obtain MT contrast.

Consider a typical imaging sequence repeated until steady state is reached (such as a spoiled gradient recalled-echo, SPGR) that produces an image M_0, as shown in figure 2.6a). The z components of the magnetization vectors of the free ($\boldsymbol{M_f}$) and semi-solid ($\boldsymbol{M_r}$, for restricted) pools are represented at the beginning of the sequence.

To obtain MT contrast, one adds a single MT saturation pulse per repetition to achieve the desired contrast in the steady state. Thus, the imaging protocol is repeated and an off-resonance MT pulse is added before each SPGR sequence, as shown in rectangle of figure 2.6b). This off-resonance pulse preferentially saturates the magnetization of the semi-solid pool, while the free pool is left relatively unaffected (1). When the magnetization vector of the semi-solid pool is saturated (2), this stimulates the transfer of magnetization from the free pool to the semi-solid pool, which results in a reduced magnetization of the free pool (3). If the SPGR sequence is performed at this moment, an image with reduced signal, M_{SAT}, is acquired. This is because the available magnetization of the free pool is reduced at the beginning of the SPGR sequence due to MT. It should be noted that in MT, the signal will always be reduced in the free pool, as the restricted pool acts as a sink for the polarization. By calculating the relative difference between images M_0 and M_{SAT}, a map of the so-called magnetization transfer ratio (MTR) can be obtained. A higher MTR signifies a lower signal in the MT-prepared image, thus reflecting a higher

amount of MT. The MTR image is the most common MT contrast image.

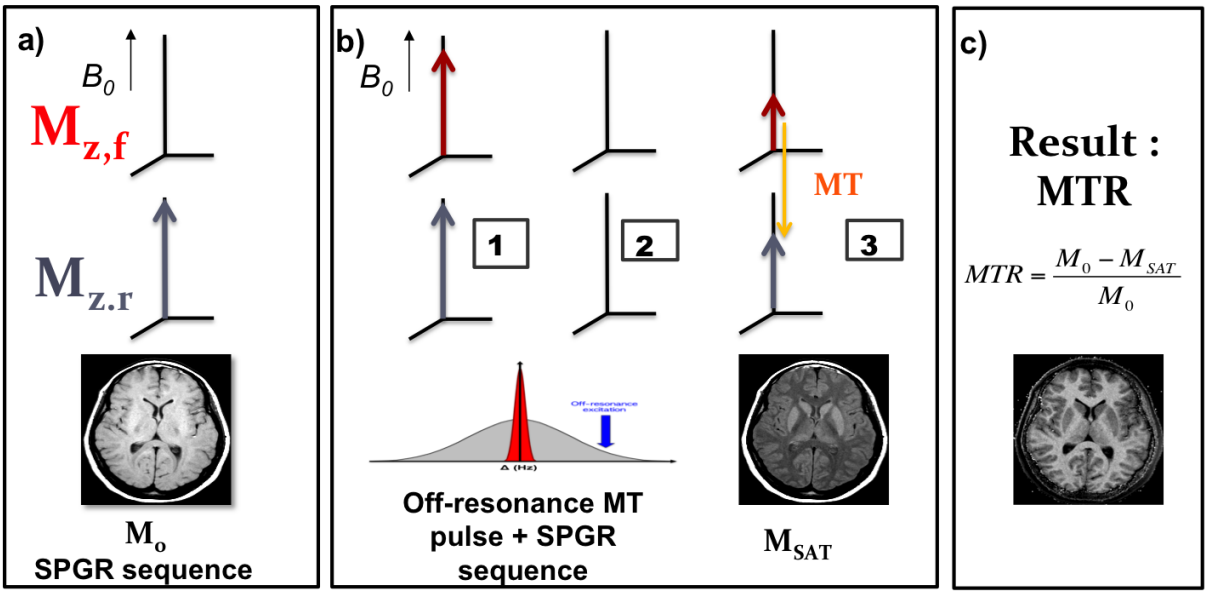

Figure 2.6 – A methodology to obtain MT contrast. In a), a conventional SPGR sequence provides an image M_0. In b) a MT-prepared SPGR sequence provides the image M_{SAT}. The MTR is obtained in c) as the relative difference between the two images. Only z components of the magnetization vectors are shown, as MT is an effect on the z component.

While the use of magnetization transfer contrast images in many studies have produced interesting results, for example, to track the progression of lesions and changes in the normal-appearing white matter in MS [18, 19], the MTR reduces the entire phenomenon of MT to a single value. In addition, the MTR is a complex combination of sequence parameters and relaxation properties of the tissue. For these reasons, the MTR is a non-specific measurement that oversimplifies MT and variations in this parameter should be interpreted carefully [17]. The semi-qualitative nature of the MTR has led to the development of a more robust and quantitative description of MT, detailed next.

MT contrast can also be obtained with on resonance pulses using sequences such as balanced steady state free precession (bSSFP) [20] and selective inversion recovery (SIR) [21]. Such sequences were not used in this work.

Chemical exchange saturation transfer (CEST) is a technique conceptually related to magnetization transfer. While chemical exchange is present in both CEST and MT, the

major difference between the two techniques resides in the population of targeted molecules. In MT, we are interested in all restricted macromolecules that participate in a transfer of magnetization. In CEST, specific molecules which have narrow resonances are targeted with off-resonance irradiation at their resonant frequency, usually different from that of water [22]. CEST contrast, similarly to MT contrast, is achieved by selective saturation of the CEST molecule, which transfers magnetization to the water pool and results in a signal reduction.

2.2.3 A quantitative interpretation of MT

The binary spin bath model and the Bloch equations

In QMT, for most methods, we can derive an expression for the steady state magnetization in a MT experiment that depends on a number of quantitative parameters describing the MT effect and the associated pools of magnetization. These parameters, which can be obtained voxel-wise by fitting the acquired data to the QMT model, are then used to produce parametric maps of regions of interest in order to evaluate the MT properties of tissues. First, we present the modified Bloch equations based on the binary spin bath (BSB) model of MT that take in account magnetization exchange (*i.e.* cross-relaxation) between the free and the semi-solid pool. Then, the equations are solved for the specific sequences used in this work and an analytical expression for the magnetization is presented.

In the BSB model, spins can exist in one of two magnetic environments : the free pool and the semi-solid pool. The two-compartment model is schematized in figure 2.7 with its characteristic parameters.

One should note that the semi-solid pool of protons does not include the hydrogen protons in water that can be temporarily linked to the restricted pool (often referred to as the hydration layer). Such protons would be considered as an additional free pool of protons. The BSB model does not differentiate between different free pools of water protons as these cannot easily be differentiated experimentally, although other studies have propo-

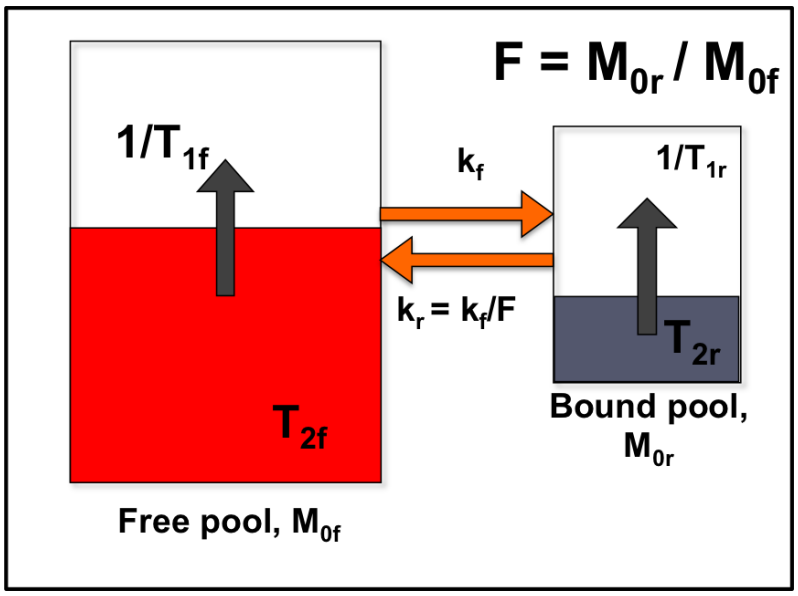

Figure 2.7 – Binary spin bath model of MT.

sed more complex models that considers more proton pools [23].

In the BSB model, each pool is characterized by its own T_1 and T_2 relaxation constants, with subscripts f and r representing respectively the free and semi-solid (r for *restricted*) pools. The transverse relaxation time of the semi-solid pool, T_{2r}, is typically on the order of microseconds. The relative size of each pool is defined by M_{0f} and M_{0r}. The semi-solid pool size ratio, F, is defined as the ratio of pool sizes (semi solid over free pool) : higher F is associated with greater macromolecular content. The semi-solid pool fraction can be in the order of 5 to 15% in brain tissue, and often up to 30% in cartilage [7, 24]. The exchange of longitudinal magnetization from the free pool to the restricted pool is described with a first order rate constant, k_f. To respect chemical equilibrium, the reverse constant $k_r = k_f/F$.

The behaviour of the magnetization of the free pool is described by the previously established Bloch equations, while that of the semi-solid pool is modelled with a rate of saturation by the MT pulse, W. This leads to a set of coupled Bloch equations, the

Bloch-McConnell equations :

$$\frac{dM_{x,f}}{dt} = -\frac{M_{x,f}}{T_{2,f}} - \Delta M_{y,f} - \mathrm{Im}\left\{\hat{\omega_1}\right\} M_{z,f} \tag{2.18}$$

$$\frac{dM_{y,f}}{dt} = -\frac{M_{y,f}}{T_{2,f}} + \Delta M_{x,f} + \mathrm{Re}\left\{\hat{\omega_1}\right\} M_{z,f} \tag{2.19}$$

$$\frac{dM_{z,f}}{dt} = R_{1,f}\left(M_{0,f} - M_{z,f}\right) - k_f M_{z,f} + \frac{k_f}{F} M_{z,r} + \mathrm{Im}\left\{\hat{\omega_1}\right\} M_{x,f} - \mathrm{Re}\left\{\hat{\omega_1}\right\} M_{y,f} \tag{2.20}$$

$$\frac{dM_{z,r}}{dt} = R_{1,r}\left(M_{0,r} - M_{z,r}\right) - \frac{k_f}{F} M_{z,r} + k_f M_{z,f} + W M_{z,r} \tag{2.21}$$

The subscripts x, y, z correspond to the transverse (x, y) and longitudinal (z) magnetization. Δ is the pulse frequency offset from resonance and $\hat{\omega}_1 = \gamma B_1$ is the complex and time varying MT pulse. W is the transition rate for the saturation of the restricted pool : it describes how a pulse saturates, as a function of time, the longitudinal magnetization of the semi-solid pool. Practically, the average rate of saturation $\langle W \rangle$ is used and is defined generally as [14, 25, 26] :

$$\langle W \rangle = \pi\gamma^2 \int_{-\infty}^{\infty} S(\Delta, \Delta') G(\Delta') d\Delta' = \pi\gamma^2 \frac{1}{\tau} \int_{-\infty}^{\infty} \left|\widetilde{B_1}(\Delta')\right|^2 G(\Delta') d\Delta' \tag{2.22}$$

where $S(\Delta, \Delta')$ is the power spectral density (PSD) of the RF saturation pulse that is applied at frequency Δ. For a finite pulse (in this case, applied at a frequency offset Δ), the PSD is given by the square of the modulus of the Fourier transform $|\widetilde{B_1}(\Delta)|^2$ of the given signal divided over the integration time τ (the pulse duration). $G(\Delta)$ is the absorption lineshape of the semisolid pool, and Δ' is an integration variable. Gaussian lineshapes have been shown to be appropriate for certain solids and gels, while a super-Lorentzian shape is more appropriate for biological tissues [4, 27]. The super-Lorentzian lineshape is defined as

$$G(\Delta) = T_{2,r} \int_0^1 \frac{1}{|3u^2 - 1|} \exp\left(-2\left(\frac{2\pi\Delta T_{2,r}}{3u^2 - 1}\right)^2\right) du \tag{2.23}$$

In the case of pulsed MT (where an off-resonance pulse is applied at the beginning of each repetition), the effective bandwidth of the PSD is much smaller than that of the lineshape [1]. From this observation and the use of Parseval's theorem (replacing the integral of $|\widetilde{B_1}(\Delta)|^2$ with that of the time-domain pulse, $|B_1(t)|^2$), one can obtain a simplified expression for the average saturation rate :

$$\langle W \rangle = \pi \frac{1}{\tau} \int_0^\tau \omega_1^2 G(\Delta) dt \tag{2.24}$$

This approximation is only valid when the bandwidth of the PSD is negligible with respect to the linewidth of the semi-solid pool. Note that this is not necessarily the case in MT sequences with much shorter pulses, such as bSSFP and saturation inversion recovery. Equations 2.18 to 2.21 can be rewritten the matrix form

$$\frac{d\mathbf{M}(t)}{dt} = \mathbf{A}(t)\mathbf{M}(t) + \mathbf{B}\mathbf{M}_0 \tag{2.25}$$

Where $\mathbf{M}$(t) is the magnetization vector

$$\mathbf{M}(t) = [M_{x,f} M_{y,f} M_{z,f} M_{z,r}]^{\mathrm{T}} \tag{2.26}$$

The transverse components of the semi-solid pool are assumed to be zero and neglected due to the extremely short relaxation time T_{2r}. The coefficients $\boldsymbol{A}(t)$ and $\boldsymbol{B}$ correspond to the terms of equations 2.18 to 2.21 and M_0 is the fully relaxed state of magnetization. One must solve this system of equations and obtain the steady-state magnetization of the free pool $M_{(z,f)}$ for a specific imaging sequence to obtain a model which can be fitted to MT-weighted data.

From this point, it is assumed that the sequence is an MT-weighted SPGR sequence (MT-SPGR), which was previously presented. The derivation of the signal equation for other types of sequences such as bSSFP and SIR can be found elsewhere [20, 21].

1. This can be verified by calculating the PSD of a typical MT preparation pulse such as a Gaussian pulse of duration 5-15 ms, and comparing it with the typical linewidth of the bound pool that is between 10-100 kHz.

Solving the coupled Bloch equations for a MT-SPGR sequence

For MT-SPGR, numerous groups have proposed different approaches and approximations to obtain an analytical signal equation from the Bloch equations [4, 28, 29, 30], as the coupled system cannot be solved analytically due to the time-dependence of the matrix A. In this work, the rectangular pulse (RP) model of Sled & Pike [17] is used. Although complex, the model was shown to be the most robust to noise as well as the most accurate with respect to numerical solutions of the Bloch equations [31, 32], although direct comparisons predate the most recent model of Müller [30]. In Portnoy's work [32] that systematically compared existing pulsed MT models, it was stated that one must proceed with care when comparing QMT parameters obtained with different models.

In Sled and Pike's model, the MT-SPGR sequence is broken down in more simple subsequences where the matrix $\boldsymbol{A}$ becomes times-independent. These situations can be concatenated together to approximate the complete repetition of the pulse sequence. Three situations are used :

— Instantaneous saturation (is) of the free pool ;

— Continuous-wave (cw) irradiation of the restricted pool ;

— Free precession (fp) of the magnetization.

In these cases, an analytic solution exists and the state of magnetization after a period τ for each situation, noted $\mathrm{F}_*(\mathrm{M},\tau)$, is given by [17] :

$$F_{fp}(\mathbf{M},\tau) = \mathrm{e}^{-\mathbf{A}_{fp}\tau}\mathbf{M} + \left[\mathbf{I} - \mathrm{e}^{-\mathbf{A}_{fp}\tau}\right]\mathbf{M}_0 \tag{2.27}$$

$$F_{cw}(\mathbf{M},\tau) = \mathrm{e}^{-\mathbf{A}_{cw}\tau}\mathbf{M} + \left[\mathbf{I} - \mathrm{e}^{-\mathbf{A}_{cw}\tau}\right]\mathbf{M}_{cw}^{ss} \tag{2.28}$$

$$F_{is}(\mathbf{M}) = \mathbf{S}\mathbf{M} \tag{2.29}$$

The magnetization vector $\boldsymbol{M}$ can be reduced to contain only the longitudinal components $\boldsymbol{M} = [M_{(z,f)} \;\; M_{(z,r)}]^T$, as the transverse magnetization of the free pool is decoupled

from the other components in these 3 situations. Transverse magnetization is assumed to disappear through relaxation and spoiling. $\boldsymbol{S}$ is a diagonal matrix with elements $[S_f \;\; S_r]$. The excitation pulse is approximated to have no effect on the semi-solid pool (i.e. $S_r = 1$), while the effect of the off-resonance pulse on the free pool is obtained through the saturation fraction S_f. The saturation fraction is defined as $M_f^+ = S_f M_f^-$, where M_f^- is the magnetization before the pulse and M_f^+ immediately after, and is mainly determined by the QMT parameter T_{2f}, and the power and shape of MT pulse. To accelerate the model fitting algorithm, S_f is pre-calculated in the Sled & Pike approach by solving the Bloch equations for the free pool in presence of the MT pulse for a wide range of pulse flip angles, frequency offsets and T_{2f}, all the while ignoring cross-relaxation and T_1 recovery, which can be shown to have a negligible impact on S_f. Other variables are defined in appendix A.

In the RP variant of the model of the MT-SPGR sequence, as shown in figure 2.8, the pulse sequence is approximated with the following steps [33] : instant saturation of the free pool from the MT saturation pulse and the excitation pulse, CW-irradiation of the semi-solid pool for a time $\tau/2$, a period TR-τ of free precession and a final CW-irradiation period of $\tau/2$. Concatenating all those steps and solving for the magnetization in the steady state ($\boldsymbol{M}(t) = \boldsymbol{M}(t + TR)$) yields a cumbersome expression for the magnetization that is a function of QMT parameters F,k_f,T_{1f},T_{2r},T_{2f},T_{1r} and sequence parameters Δ, the offset frequency of the MT pulse, $\alpha_M T$, the flip angle of the MT pulse, and α, the flip angle of the excitation pulse. Some authors use more often the term MT pulse power instead of MT pulse flip angle $\alpha_M T$. The two terms are often interchanged in this work, as they are closely related. In appendix A, a more detailed derivation of the signal equation is provided.

It should be noted that modelling the MT pulse as an instantaneous fractional saturation of the free pool is an approximation that might lead to errors in the magnetization of the free pool. However, as discussed in [32], the error is small if we consider off-resonance pulse above 1 kHz. In addition, a fully continuous model that would not make this approximation does not have an analytical solution and is then impractical for fitting purposes.

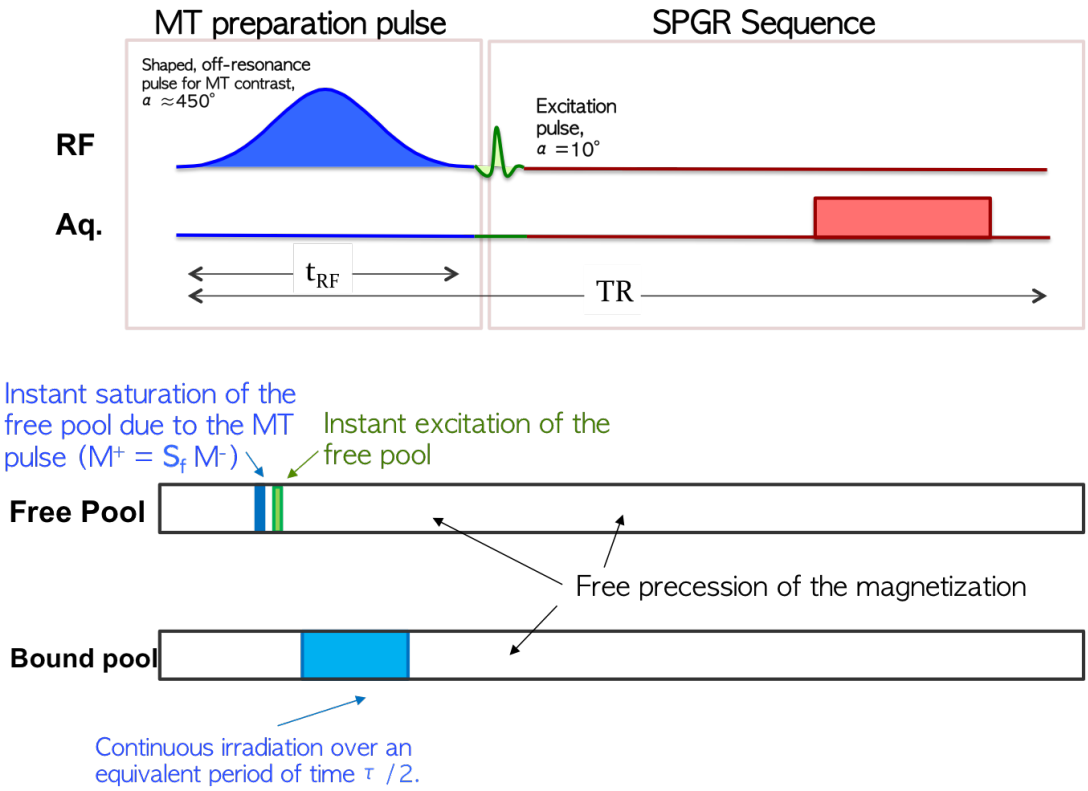

Figure 2.8 – Schematic of the MT-SPGR sequence and evolution of the magnetization of each pool according to the RP model. Here, τ is not equal to the pulse duration τ_{RF}, but represents the duration of a rectangular pulse of equivalent power to the off-resonance MT pulse.

Data acquisition and fitting procedure

The derived signal equation in appendix A, is practically independent of T_{1r}. A common practice is to fix T_{1r} either to T_{1f} or to 1 s. This was shown to have negligible effect on the signal equation [17]. In addition, T_{1f} is not uniquely determined by the signal equation, so one needs to obtain an independent estimation of T_{1f} [34].

Henkelman *et al.* [4] proposed to obtain an independent estimate of the apparent longitudinal relaxation constant, T_{1obs}, through an inversion recovery (IR) experiment and to recover T_{1f} from T_{1obs}. The procedure is detailed in [4]. As discussed earlier, T_1 values in this work were obtained with VFA measurements in the interest of faster scan time and efficient volumetric mapping. It has been shown recently [35] for VFA sequences that cross-relaxation (MT) affects the estimates of T_{1obs} in macromolecular-rich tissues such as cartilage, which are studied in this work. To account for the effect of MT, a global

fitting approach that fits the signal equation of Sled & Pike to both VFA and MT-SPGR data was used as detailed further below.

In QMT, multiple volumetric datasets are acquired and the model signal equation is fitted through a nonlinear least-squares approach to the data in order to provide an estimation of F, k_f, T_{1f}, T_{2f} and T_{2r}. The signal equation depends on sequence parameters Δ, α_{MT} and α. For VFA measurements, the data is acquired with no MT preparation pulse ($\Delta, \alpha_{MT} = 0$) and various flip angles α. The MT-SPGR data is usually obtained at fixed α, and with a combination of various Δ and α_{MT}. As the signal equation is nonlinear, the choices of Δ and α_{MT} influence the quality of the fit : this was explored further with simulations, in section 3.3.6.

The signal obtained from a single voxel as a function of Δ and α_{MT}, normalized to the signal without saturation, can be represented in a space called the Z-spectrum. On a voxel-wise basis, the signal equation is fitted to the Z-spectrum. An example of a Z-spectrum is presented in figure 2.9.

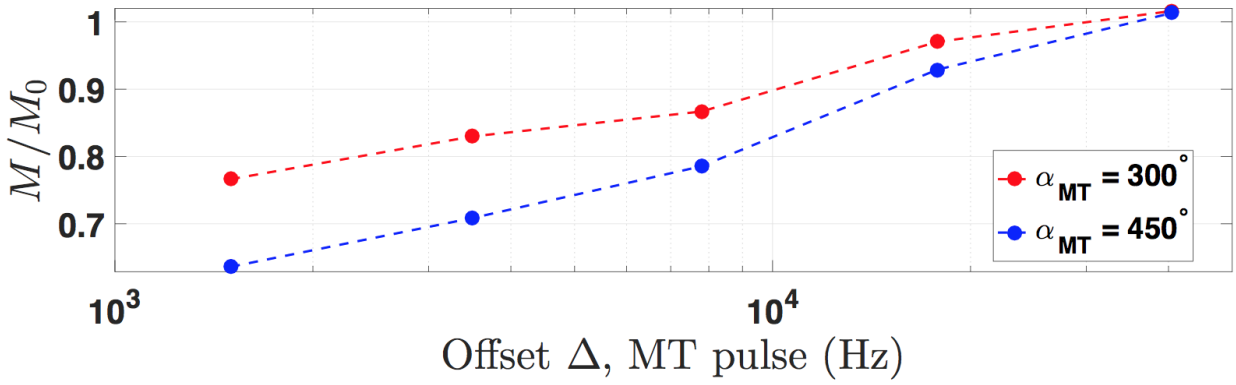

Figure 2.9 – Example of Z-spectrum for a meniscus voxel.

In the Z-spectrum, the relative signal M/M_0 is shown as a function of the frequency offset of the MT pulse and its flip angle, α_{MT}. To obtain the Z-spectrum, the signal is sampled at various combinations of (Δ, α_{MT}) and then normalized by a volume acquired with no MT contrast (the MT pulse is removed). The value M/M_0 shows the loss in signal due to MT only. In figure 2.9, a higher MT effect (increased signal reduction) is seen for larger

MT pulse powers and offsets closer to resonance.

A Levenberg-Marquardt algorithm was used to perform voxel-wise nonlinear least squares fitting to produce the best-fitting QMT parameters. An illustration of the data acquisition and fitting procedure is shown in figure 2.10.

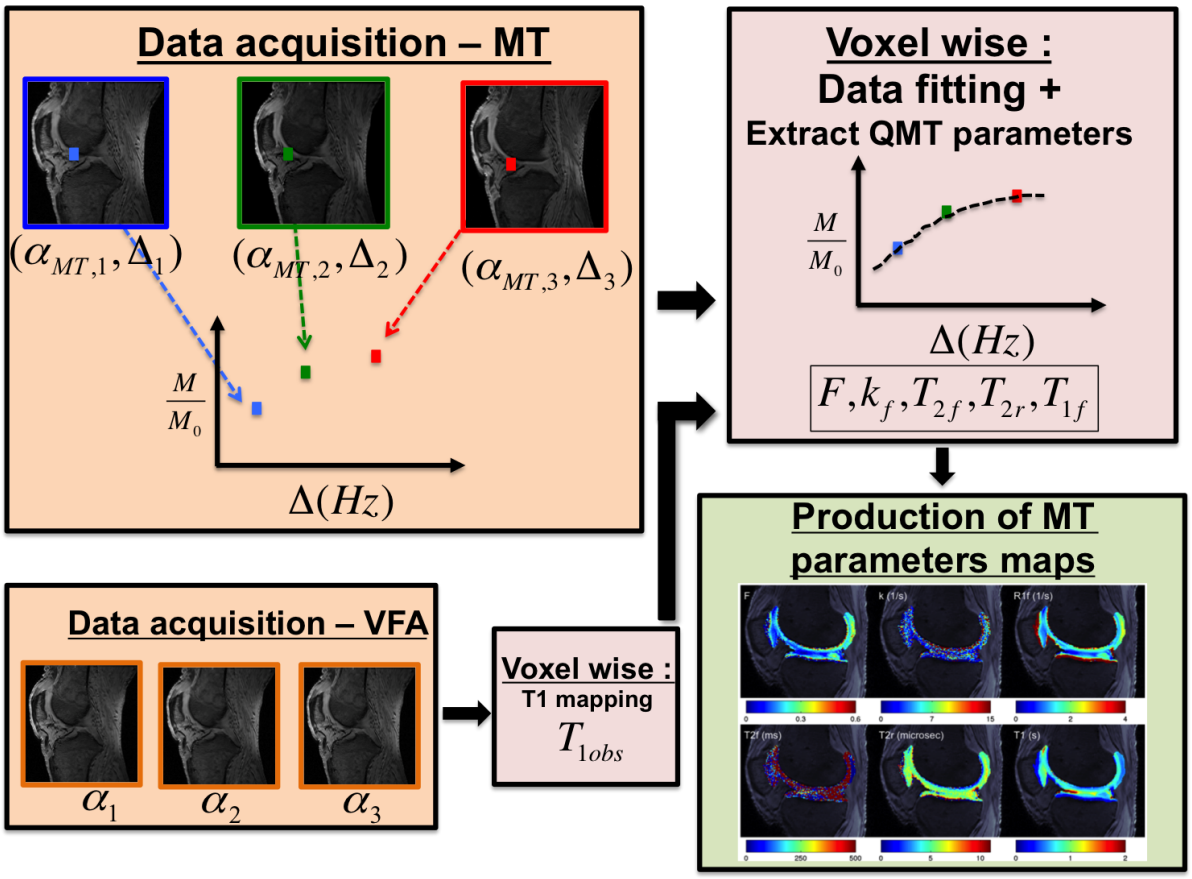

Figure 2.10 – Data acquisition and fitting procedure for MT and VFA datasets. Data acquisition - MT : Multiple volumes are acquired (only 3 shown) at various combinations of (Δ, α_{MT}). The Z-spectrum is created using the response of each voxel as a function of frequency offset and MT pulse flip angle and is then fitted. This allows the extraction of best-fitting QMT parameters to produce parametric maps. Data acquisition - VFA : this method demonstrates the original T_{1f} evaluation method proposed by Henkelman [4].

2.3 Osteoarthritis

In this section, we describe briefly the disease of osteoarthritis (OA) and focus on the microscopic changes that occur during OA, which MT might be used to probe. Other MRI techniques used to investigate early OA are discussed and compared to QMT.

2.3.1 Early changes in osteoarthritis

Osteoarthritis is a degenerative joint disease that leads to joint pain, stiffness and loss of function in weight-bearing joints such as the knees. OA can be described as the outcome of multiple types of disorders caused by a combination of biomechanical, biochemical, inflammatory and immunology factors [36, 37, 38, 39]. Some disorders include the loss and erosion of articular cartilage and meniscal degeneration [40].

On a macromolecular scale, articular cartilage is composed of an extracellular matrix (ECM) in which resides a network of collagen fibrils that grants the structural framework for the cartilage. Proteoglycans (PGs) are embedded within the collagen network and each PG is composed of a protein core with negatively charged glycosaminoglycans (GAGs) molecules covalently attached as side-chains. The rest of the tissue weight is composed of water containing various mobile electrolytes [41]. Early OA is characterized by changes in the macromolecular structure of the cartilage, specifically an increase in water content, a loss of PGs and a disruption of the collagen fiber network [42, 43, 44, 45]. This is shown schematically in figure 2.11.

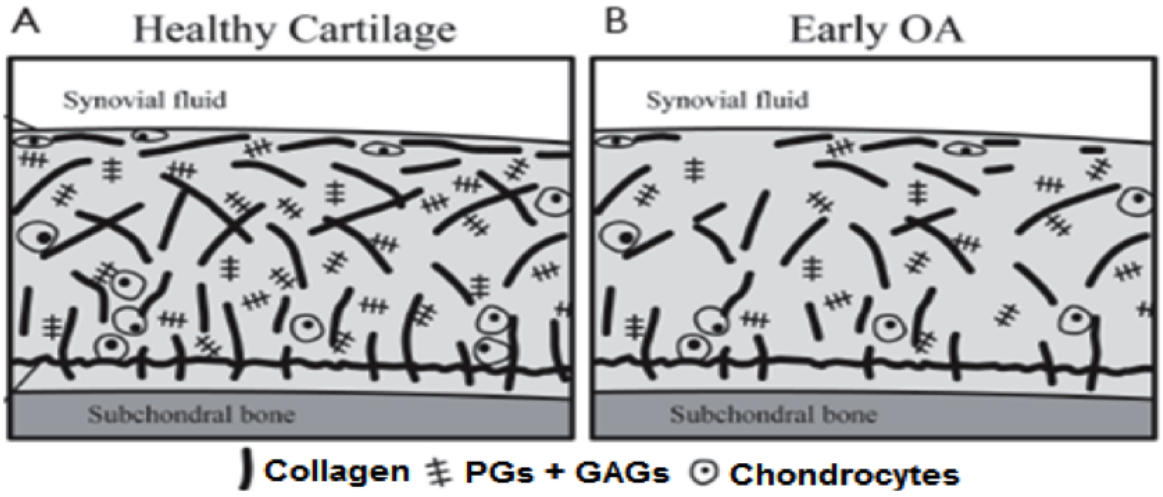

Figure 2.11 – Microscopic changes induced by early OA. Adapted from [5].

Therefore, there is significant interest to develop techniques that can measure macromolecular changes in articular cartilage for the early diagnosis of OA, as well as for monitoring

and evaluating the progress of current and future therapies that aim to control joint tissue degradation [46].

Recent research has shown that knee OA involves the degeneration of not only the cartilage in the joint, but also of other structures such as the subchondral bones, the ligaments, muscles and the menisci [47]. The menisci are crescent-shaped fibrocartilaginous structures attached to the tibial plateau and are mostly composed of water, circumferentially oriented collagen fibers and PGs [47]. Menisci are known to be vital for the health of the knee joint, having roles ranging from load distribution, shock absorption and providing nutrition as well as lubrication to the knee joint [47, 48]. It is unclear, however, if degradation of menisci is a cause or a consequence of OA. For example, meniscal lesions in healthy knees can lead to OA through the loss of meniscal functions, while OA might give rise to meniscal lesions such as tears, which will themselves accelerate the evolution of the condition. It is expected that the pathological processes which cause early OA in the joint cartilage should not be limited only to cartilage and might affect the meniscal tissues equally, as the tissues share similar components and properties and are subject to similar mechanical stress [47]. Thus, in addition to evaluating the health of articular cartilage, assessing the degradation of the menisci is of interest for early OA detection.

2.3.2 Assessment of early osteoarthritis with MRI

Conventional MRI and plain radiography are already widely used clinically to assess articular cartilage damage, gross joint morphology changes and meniscal tears [49]. However, as these macroscopic degenerative changes are typically absent in early stages of OA, other techniques must be used to detect early OA. These techniques must have the capacity to probe the microscopic structure and composition of the joint tissues, as changes in the ultra-structure and composition may be indicative of early OA [46]. This can be challenging : macromolecules such as collagen and PGs have very short T_2 relaxation time owing to the semi-solid protons in the macromolecules [49], which makes their direct observation difficult in conventional MRI.

There are multiple quantitative MRI techniques that can assess the microscopic structure and composition of the joint by increasing the dependence of the MRI signal to macromolecular content, specifically PGs and collagen. Techniques such as $T_{1\rho}$ relaxation imaging [50, 51, 52, 53], delayed gadolinium-enhanced MRI of cartilage (dGEMRIC) [54, 55, 56], sodium imaging [57, 58, 59, 60, 61] and chemical exchange-dependent saturation transfer (CEST) imaging [58, 62, 63, 64] have all been shown to be sensitive to the PG content in cartilage, while other techniques such as T_2 mapping [65, 66, 67], diffusion MRI (specifically diffusion weighted imaging (DWI) [68, 69, 70, 71] and diffusion tensor imaging (DTI) [72, 73]) are sensitive to the ultra-structure (orientation and content) of collagen.

Current quantitative MRI methods to assess the ultra-structure of collagen have their limitations. Interpretation of changes in T_2 values is ambiguous due to the number of competing processes that influence the nonspecific parameter T_2. It has been suggested [74] that 60% of the variation in T_2 values can be attributed to changes in collagen fibril orientation (following the magic angle effect [75]) and organization, while the remaining 40% is determined by a combination of changes in water content and concentration of other macromolecules [46]. For in vitro cartilage studies, different types of immersion fluids used to preserve human tissue before imaging might influence T_2 relaxation times [76]. In DWI, it was noted by the authors of a longitudinal study [71] that quantitative diffusion parameters such as ADC were difficult to obtain in cartilage, resulting in a semi-qualitative analysis. Presently, DTI is limited for the in vivo evaluation of cartilage due to long acquisition times and intensive data analysis [46].

2.3.3 Early osteoarthritis and magnetization transfer

QMT MRI is a technique that can indirectly probe the macromolecular content of tissues, typically unobservable in conventional MRI. By comparing the amplitude of the signal reduction in the Z-spectrum with in vitro samples of the different components of articular cartilage at various concentrations, it has been shown that the major contributor to the MT effect in cartilage is collagen [77, 78]. Within the same studies, it was also shown

that another smaller, still significant contribution to the MT signal is caused by modifications in PG concentration and tissue structure due to pathological and physiological perturbations [78]. This is supported by experimental NMR observations that the largest magnetization-exchanging subsystem in cartilage is collagen and water, followed by PGs and collagen [79]. As the MT signal is sensitive to collagen ultra-structure and content [77] as well as the PG content [78], it is an interesting candidate for the non-invasive assessment of cartilage and meniscal tissues.

QMT might provide insights on the macromolecular content of cartilage through physically meaningful parameters extracted from a quantitative model of MT. First, an estimation of the properties and size of the macromolecular pool of protons is obtained through the parameters F (also referred to in some publications as the bound pool fraction, BPF) and k_f (the first-order rate of magnetization exchange from the free pool to the restricted pool). Second, QMT also provides the T_1 and T_2 relaxation times of the free (T_{1f}, T_{2f}) and semi-solid (T_{2f}, T_{2r}) pools of protons. The bound pool fraction F is believed to be an indirect measurement of the macromolecular content, while k_f and $?_{2r}$ are indicative of, first, the efficacy of MT between the two proton pools, which is related to the organization of macromolecules [17, 28, 80] and, second, the diffusion of spins between proton sites in macromolecules, related to the ultra-structure [6, 17, 28, 80]. The relaxation time of the semi-solid pool, T_{2r}, has also been interpreted as a measure of the rigidity of the semi-solid (or macromolecular) structure [24].

Preliminary QMT studies have been performed in cartilage, mostly ex vivo. Li *et al.* have shown that F is strongly correlated with the GAG content in tissue-engineered cartilage [81]. This group has also shown that the magic angle effect is reduced in MT weighted images that are required for QMT mapping [82], an advantage over T_2 mapping techniques in cartilage. Stikov *et al.* have shown that moderate correlations exist in articular cartilage extracted from cadaveric knee specimens between F and PG content as well as between k_f and collagen, concluding that QMT parameters can be used as biomar-

kers to evaluate PG and collagen content in cartilage [7]. More recently, Sritanyaratana *et al.* have shown that patients with OA have significantly lower k_f and significantly higher T_{2r} values in patellar cartilage than asymptomatic volunteers, suggesting that QMT parameters can detect changes in the macromolecular component of degraded cartilage in vivo. However, the authors also concluded that further studies are needed to better understand the fundamental mechanisms responsible for changes in QMT parameters for patients with OA [6].

Preliminary studies have shown a possible link between OA and QMT parameters and identify QMT as a promising technique for the early detection of OA.That said, the use of MRI scans as a screening tool for OA is debatable, as the method is too expensive to be administered on all asymptomatic individuals. One possible methodology would be to identify individuals at high risk of developing OA based on known risk factors, leading to screening with QMT MRI. Established risk factors associated to the development of OA include low vitamin D intake, genetics, obesity and the participation in sports which lead to high-intensity and direct join impact with other participants or playing surface and equipment [39].

3 Quantitative magnetization transfer imaging in cartilage and meniscus

3.1 Introduction

QMT has previously been applied to brain, with a few recent studies in articular cartilage [6, 7], but none so far in the meniscus. As a result, QMT is not fully established in cartilage and meniscus and the QMT techniques might not be adapted to such tissues.

The purpose of this chapter is to investigate potential modifications to the QMT processing pipeline and to propose an adapted QMT algorithm for cartilage and meniscus. The modifications are presented in section 3.2. The performance of the adapted algorithm is then detailed in section 3.3, notably with respect to noise, the value of the fixed parameter T_{2f}, and the Z-spectrum sampling scheme.

To evaluate the performance of the adapted algorithm, we used the cadaver knee specimen data acquired in this study and Monte Carlo simulations. The methods to obtain QMT parameter maps from MT-SPGR datasets and the cadaver knee data acquisition in the cadaver knee specimens are described in the methods section of chapter 4, and are not repeated here for the sake of brevity. The methodology used for the Monte Carlo simulations is detailed in section 3.3.1.

3.2 Adaptation of QMT fitting to cartilage and meniscus

3.2.1 Joint fitting of T_1 and magnetization transfer data

In this work, the MT data was obtained with a MT-prepared SPGR sequence, while the required T_{1obs} was obtained from a variable flip angle (VFA) experiment.

Following the observations of Mossahebi *et al.* [35] that T_{1obs} estimation is affected in VFA experiments in macromolecular-rich tissues such as cartilage and meniscus due to MT, we fit simultaneously voxel-wise VFA and MT data to Sled & Pike's signal equation of MT, using a zero duration MT pulse for VFA measurements. This accounted for MT effects in VFA measurements. Therefore, instead of calculating T_{1f} analytically from an independent observation of T_{1obs} as proposed by Henkelman [4], T_{1f} was fitted conjointly with other QMT parameters. The procedure is illustrated in figure 3.1, which is a modified version of the QMT pipeline shown in figure 2.10.

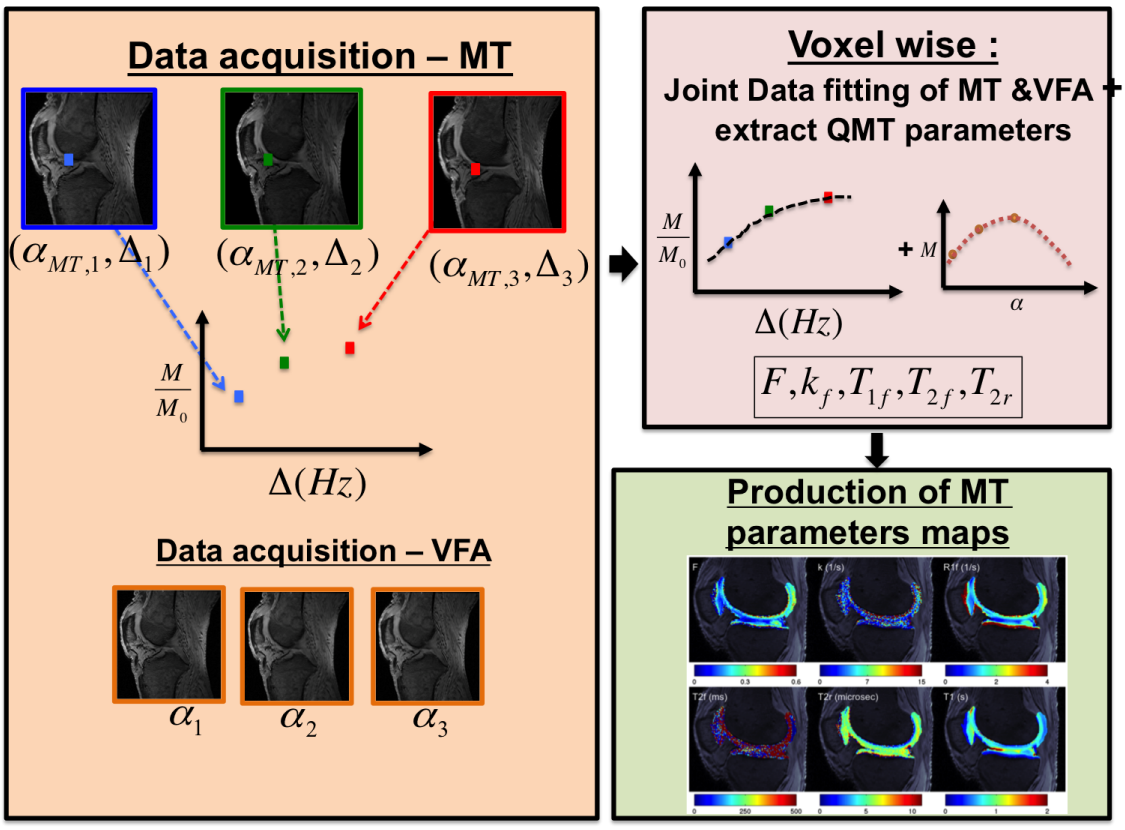

Figure 3.1 – Data acquisition and joint fitting procedure for MT and VFA datasets.

The MT data used in the least squares algorithm (the Z-spectrum) is normalized between 0 and 1 : each acquired MT volume is normalized by another obtained without a MT preparation pulse. By normalizing, the procedure removes the proton density dependence in the signal equation. In VFA measurements, no normalization procedure is typically performed and a factor proportional to the proton density, S_0, as well as T_{1obs} are fitted. The amplitude of the VFA signal in our datasets was typically between 500 and 1500 arbitrary units, much larger than the normalized MT signal between 0 and 1.

A consequence of the lack of normalization in VFA measurements when fitting both datasets simultaneously is the much larger amplitude of residuals for VFA measurements compared with normalized MT measurements. Ideally, both datasets should be normalized similarly to have an equal weight in the least squares fitting approach. Mossahebi *et al.* [35] suggested that the VFA data could be normalized by the same normalization volume as the MT-SPGR datasets, provided that some sequence parameters (TR,TE) and acquisition parameters (transmit and receive gains) are identical. The data in this work was acquired before joint fitting was explored and the TRs of MT and VFA datasets were different. As an alternative, we propose to normalize VFA measurements with a synthetic normalization volume, calculated as follows.

For each voxel, T_1 mapping was performed according to the procedure described in section 2.1.5 to extract estimates of T_{1obs} and S_0. Then, the Ernst angle $\alpha_E = \cos^{-1}\left(\exp\left(-TR/T_{1obs}\right)\right)$, which maximizes the SPGR signal, was calculated, followed by the evaluation of the maximum theoretical signal using equation 2.17, $M(\alpha_E, TR, S_0, T_{1obs})$, at each voxel. A synthetic volume with the theoretical maximum signal intensity at each voxel was then obtained. To obtain normalized VFA measurements between 0 and 1 and adequately perform the joint fitting approach, each acquired VFA volume was divided by the calculated synthetic volume.

3.2.2 Constraining the model with a fixed T_{1f}/T_{2f} ratio

During initial attempts at fitting QMT parameters, it was observed that robust estimates of F, T_{2r} and T_{1f} could be obtained, while the fit was relatively insensitive to T_{2f} and less robust to k_f. The reasons are discussed through chapter 3. To stabilize the fitting procedure, the number of free parameters in the model was reduced by fixing T_{2f}. The final four QMT parameters calculated were : the bound pool fraction F, the exchange rate k_f, the T_1 relaxation time of the free pool (T_{1f}) and the T_2 relaxation time of the restricted (T_{2r}) pool.

In Sled & Pike's RP model, the direct saturation of the free pool by the off-resonance MT pulse is modelled as an instantaneous fractional saturation of the magnetization. The amount of saturation depends on the absorption lineshape of the free pool and, thus, on the relaxation time T_{2f}. The saturation fraction becomes more important at high power MT pulses and closer to resonance. In the MT protocol used in this work, the measurements were acquired at low power and far from resonance. The consequence is that the fit of the MT model was not sensitive enough to T_{2f} with the current sampling. This is typically observed in QMT protocols with few sampling points, and T_{2f} is often fixed in quantitative models of MT [7, 6, 28]. In addition, most two-pool models of MT [17, 83] inaccurately reproduce the Z-spectrum when compared to the numerical solution to the Bloch-McConnell equations close to resonance, leading to potentially biased fits of T_{2f}.

One proposed practice is to fix T_{2f} to a specific ratio of T_{1f} [6, 7, 83]. Yarnykh and Yuan [83] have discussed that, in brain tissue, T_{2f} can be fixed voxel-wise by fixing the ratio T_{1f}/T_{2f} to a constant value, as the ratio is relatively constant in brain, even though T_{1f} and T_{2f} themselves may vary largely. Yarnykh and Yuan have proposed a fixed mean value of $T_{1f}/T_{2f} = 18.18$, based on QMT data from the literature giving ratios between 15 and 22 in the brain. This approach was adapted for the knee joint tissues.

Practically, values of T_{1f}/T_{2f} can be found in the literature for brain tissue at 1.5 T [83] and at 3 T [84, 85], but there are no published values in articular cartilage or in the meniscus at 3 T. A QMT study in tibial and patellar cartilage [7] fixed the ratio to 20 based on their own observations of T_{1obs} and T_{2obs} in the specimens. However, the value of T_{1f} can be significantly different from T_{1obs} [17, 35] and T_{2f} can differ from T_{2obs}, especially in tissues known to have multiple free water components where the mono-exponential fit of T_{2obs} is an inadequate representation of the proton pools in the tissue [17]. Therefore, the ratio T_{1f}/T_{2f} is not necessarily equal to T_{1obs}/T_{2obs}.

Here, we propose to evaluate the ratio T_{1f}/T_{2f} through a direct evaluation of T_{1f} in cartilage and menisci and an estimation of T_{2f} from T_{2obs} in the literature, being aware of a potential disagreement between T_{2obs} and T_{2f}.

Estimation of T_{1f} in cartilage and meniscus

When joint-fitting VFA and MT data, the dependence with respect to T_{1f} was mostly present in the VFA data points. Because there is no off-resonance pulse in the VFA datasets, there was no noticeable dependence on T_{2f} in the VFA datasets for the model of MT used in this work. A consequence is that the estimates of T_{1f} in the joint-fitting approach were practically independent of the fixed T_{2f} value, which is equal to a specific T_{1f}/T_{2f} ratio.

To illustrate this concept, the mean T_{1f} in the medial and lateral menisci from one of the specimen (*in situ*) was shown to vary by less than 2% on a wide range of T_{1f}/T_{2f} from 10 to 100, as seen in figure 3.2. Based on T_{1obs} and T_{2obs} values in the meniscus from the literature, an approximate value of T_{1f}/T_{2f} can be expected to be in the range of 60 to 90.

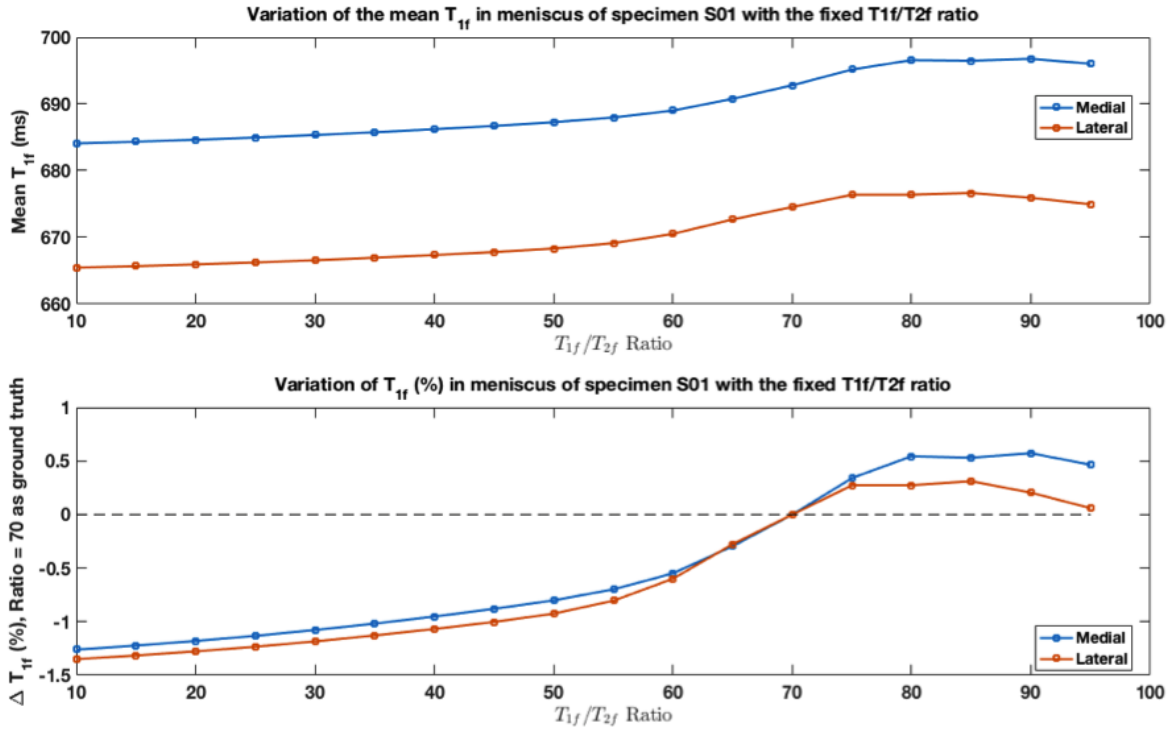

Figure 3.2 – Mean T_{1f} (top, in ms) and percent deviation from a ratio of 70 (bottom) in a typical sample for the medial and lateral menisci, as a function of the fixed ratio T_{1f}/T_{2f} . The variation is less than 2% for a range of T_{1f}/T_{2f} much larger than the expected variability from noise. This variation is representative of all other specimens and tissues (cartilage) evaluated in this study.

Thus, because the estimates of T_{1f} were essentially independent of the fixed T_{1f}/T_{2f} , the following procedure was proposed to estimate T_{1f} in a specific tissue :

1. Fix an approximate value of T_{1f}/T_{2f} based either on observations of T_{1obs} and T_{2obs} in the tissues of interest or on literature values ;
2. Produce QMT maps through voxel-wise fitting of the MT model with T_{2f} fixed through the chosen T_{1f}/T_{2f} at step 1 ;
3. Evaluate the mean T_{1f} in each tissue of interest by averaging all voxels and all samples.

This estimation of T_{1f}, for the specific QMT protocol used in this study, will be within 2% of the value that would be obtained with a theoretically correct ratio, as shown in figure 3.2. While the process of fixing T_{1f}/T_{2f} to obtain an estimate of T_{1f} might seem circular, the very weak dependence of T_{1f} with respect to the fixed T_{2f} demonstrates that the procedure is adequate. For additional precision on the value of T_{1f} to use in order to fix

the ratio, the previous 3 steps were iterated, although the additional precision obtainable was less than 0.5% after multiple iterations.

The mean T_{1f} in cartilage and meniscus (*in situ* and *ex situ*) obtained are listed in table 3.1. To produce these values, T_{1f}/T_{2f} was first approximated to respectively 25, 70 and 60 based on our own measurements of T_{1obs} and T_{2obs} in these tissues.

Table 3.1 – Mean values of T_{1f} in cartilage, *in situ* and *ex situ* menisci.

Tissue	**Mean T_{1f} (ms)**
Cartilage	1021
Meniscus - *in situ*	886
Meniscus - *ex situ*	1367

Estimating T_{2f} in cartilage and meniscus

The treatment of T_2 relaxation times is complex in tissues such as cartilage and meniscus, which are known to be characterized by multiple free water T_2 components [86, 87, 88]. In this situation, it is unclear how to relate T_{2obs} and T_{2f}.

Values of T_{2obs} reported in the literature are typically obtained through mono-exponential fits and assume a single pool of protons. The value of T_{2obs} obtained is then an average of all pools of water. Assuming that only a single free pool of protons exists, T_{2obs} is theoretically equivalent to T_{2f} ; however, significant differences were noted in agar gels supposedly composed of a unique free pool [17], showing that even in substances with a single free pool, T_{2obs} is not necessarily equal to T_{2f}.

Values of T_{2f} obtained in QMT experiments from the binary spin bath model also assume a single free pool of protons and is a simplification of human tissues, which are more complex. For example, in cartilage, NMR and MRI studies have identified bulk water and water more closely bound to proteoglycan as distinct pools of free water [89]. Therefore, a single relaxation time for the free water obtained in MT experiments will represent an

average of all free pools of water and is a simplification of a more complex reality.

Overall, T_{2obs} and T_{2f} can be interpreted as different weighted averages of the multiple free pools of water in tissues [17]. In addition, they are obtained from very different measurements : T_{2obs} from a characterization of the time-domain behaviour of the signal, and T_{2f} from a measurement of the width of the Lorentzian lineshape of the free pool. Because there are no published values of T_{2f} in the literature for cartilage or meniscal tissues and that robust fits of T_{2f} could not be obtained from the current dataset, an alternative was to replace T_{2f} by T_{2obs} measurements in the calculation of the T_{1f}/T_{2f} ratio while being aware that a bias might be introduced with this approximation. For example, in brain tissue, it was noted that T_{2obs} was consistently higher than T_{2f} and could even be twice the value of T_{2f} [17]. Therefore, the bias in estimating T_{1f}/T_{2f} might be significant when approximating the transverse relaxation time of the free pool through T_{2obs}. At the moment, it is unclear how a biased estimation of T_{2f} through an incorrect T_{1f}/T_{2f} ratio propagates in the model and biases other QMT parameters. If the bias is minimal, then an approximate ratio is appropriate. This is discussed in section 3.3.4.

Before choosing to use a mean T_{2obs} as an approximation to T_{2f}, we investigated if a mean T_{2f} could be inferred from published relaxation times of the free pool based on multiple components models. There are some, but few reports of free pool relaxation times obtained through multiple component models in the cartilage and meniscus. For example, Liu *et al.* [86, 87, 89] used the multi-component DESPOT [90] approach to obtain fast (T_{2F}) and slow (T_{2S}) components in cartilage and meniscus, which are thought to be two water components. However, it is not clear how the different relaxation times that characterize the free pools of MT should be combined and/or averaged to provide an effective estimation of T_{2f}. For those reasons, the T_2 relaxation times from multi component techniques were not used to provide an estimation of T_{2f}.

We proceeded by reviewing the existing values of T_{2obs} in order to fix a value for T_{2f}.

This fixed value was known to be biased, and the impact of choosing an incorrect ratio will be reported in section 3.3.4. Table 3.2 shows T_2 values for healthy cartilage and menisci at 3 T from various sources in the literature. The list of sources and values are listed in appendix C. In addition, we included a T_2 relaxation time in extracted meniscus from a recent study [91] at 3 T that used a CPMG sequence for T_2 mapping, as extracting and conserving the menisci may be expected to affect relaxation times. In that study, the meniscal tissues were scanned in perfluoropolyether (Fomblin) to prevent dehydration and minimize tissue-air susceptibility artefacts. This is similar to the fluid used in this work to scan the extracted menisci, another perfluorochemical (perflubron).

Table 3.2 – Average T2 values and standard deviation (SD) for various healthy knee joint tissues obtained from the literature at 3 T.

Tissue	**Mean T_{2obs} (ms)**	**SD (ms)**
Both menisci	11.0	0.5
Lateral meniscus	10.7	0.4
Medial meniscus	11.3	0.4
Whole cartilage	34.9	4.6
Femoral cartilage	37.9	5.7
Patellar cartilage	32.7	3.7
Tibial cartilage	32.6	4.5
ex situ menisci	20.2	5.3

In the literature, at 3 T, average values of 34.9 ± 4.6 ms were obtained for the cartilage, 11.0 ± 0.5 for the *in situ* menisci and 20.2 ± 5.3 ms for the *ex situ* menisci.

Because the range of T_2 values in the *in situ* menisci has a very small spread in the literature (0.5 ms), we use this mean value as an estimator of T_{2f}. Because the range of values is very small, the ratio is minimally affected by either the choice of the mean value or the smallest value. Taking the average value from 4 different studies gives more confidence in the estimate of T_{2obs} than using a single study that provides the smallest value. For the *ex situ* menisci, the only value of 20.2 ms found in the literature at 3.0 T for extracted and conserved menisci was used.

For the cartilage, a mean value of 34.9 ms was obtained by averaging 11 studies. The minimal value identified in any region of the cartilage was 27.0 ms, and the highest was 44.4 ms. We identified the mean value as our estimate of T_{2f} and will evaluate, in section 3.3.4, the impact of choosing an incorrect ratio based on the distribution of T_2 values from literature.

Final values of T_{1f}/T_{2f}

Table 3.3 summarizes the chosen values of T_{1f} and T_{2f} and the corresponding ratio for each tissue of interest. Different values for the ratios were found for the different regions analyzed, and the voxels must be processed separately whether they are identified as cartilage or menisci.

Table 3.3 – Estimation of T_{1f}/T_{2f} for various knee joint tissues at 3 T.

Tissue	$\boldsymbol{T_{1f}}$ **(ms)**	$\boldsymbol{T_{2f}}$ **(ms)**	$\boldsymbol{T_{1f}/T_{2f}}$
Menisci - *in situ*	886	11.0	80.5
Menisci - *ex situ*	1367	20.2	67.7
Whole cartilage	1021	34.9	29.3

First, it should be noted that the ratios used in chapter 4 are slightly different than the ones presented here due to the addition of a new knee specimen at the end of the project. It is of interest to note that the value of T_{1f}/T_{2f} is similar (≈15-20% difference) for *in situ* and *ex situ* menisci, although the values of T_{1f} and T_{2f} themselves vary. Concerning the whole cartilage, a potential issue with a single fixed ratio is the fact that T_{1obs} and T_{2obs} in cartilage are known to vary with cartilage depth. However, there have been multiple reports that both T_{1obs} [92, 93, 94] and T_{2obs} [95, 96, 93] decrease with depth in cartilage and thus a fixed ratio for the entire cartilage is a safe assumption.

Another issue is the uncertainty in T_{1f}/T_{2f} that comes from using various sources from the literature, and how this can affect QMT parameters. In cartilage, the range of T_{2obs} from the literature was between 27 and 44.4 ms. Assuming a correct estimation of T_{1f}, the

ratio T_{1f}/T_{2obs} then ranges from 23 to 38. Because of this possible variability in the ratio, we evaluate the impact on QMT parameters of attributing an incorrect ratio of 29 $\pm$ 10 in cartilage data. These results are presented in section 3.3.4. For meniscus, although the range of T_{1f}/T_{2f} is more constrained, we also evaluate the impact of attributing an incorrect ratio of 81 $\pm$ 10.

3.3 Evaluation of the adapted quantitative magnetization transfer method

We characterized our proposed QMT method, based on the model of Sled and Pike and adapted with joint fitting of VFA data and fixed T_{2f}, in terms of its performance in the presence of noise, variability with the fixed T_{2f}, and the sampling scheme.

3.3.1 Methodology for the simulations

We investigated the response to noise of the estimation method with the current Z-spectrum sampling scheme through Monte Carlo simulations. Two synthetic phantoms were created, each consisting of 2 sets of MT model parameters representing either cartilage ($F = 16.5\%$, $k_f = 2.33\ s^{-1}$, $T_{1f} = 1016$ ms, $T_{2r} = 5.09\ \mu$s) or meniscus ($F = 23.5\%$, $k_f = 1.75\ s^{-1}$, $T_{1f} = 886$ ms, $T_{2r} = 5.75\ \mu$s) based on mean values measured in our specimens. Note that due to the nonlinear nature of the model, the response to noise and sampling scheme is likely to vary with respect to the value of MT model parameters, which is why the simulations were performed for numerical phantoms of meniscus and cartilage.

A normalized, noiseless Z-spectrum signal was simulated with the RP model of Sled & Pike (equation A.12), and VFA data was simulated based on equation 2.17. Additive Gaussian noise with a standard deviation of 1/SNR was added to each Z-spectrum and VFA data point. 10,000 noise realizations were performed for each set of MT parameters to provide mean and standard deviations. The impact of different sampling schemes and

the sensitivity to the chosen ratio T_{1f}/T_{2f} was investigated with similar simulations. To evaluate the response to noise, the 10,000 noise realizations were done for SNRs of 50, 75, 100, 125, 150, 200, 250, 300 and 500.

Outlier removal was performed according to the procedure detailed in chapter 4.

3.3.2 Results : robustness to noise

The performance of the algorithm in the presence of noise is discussed in terms of accuracy and precision with the levels of SNR mentioned in section 3.3.1. The results provide insight on the achievable quality of fits for the specific sampling scheme used in this work and for the SNR observed in our data, which approximately 100. Simulated signals were generated as described in section 3.3.1. We refer to these simulations as cartilage and meniscus simulations. Figures 3.3 and 3.4 show the robustness to noise of the estimation method in these simulations.

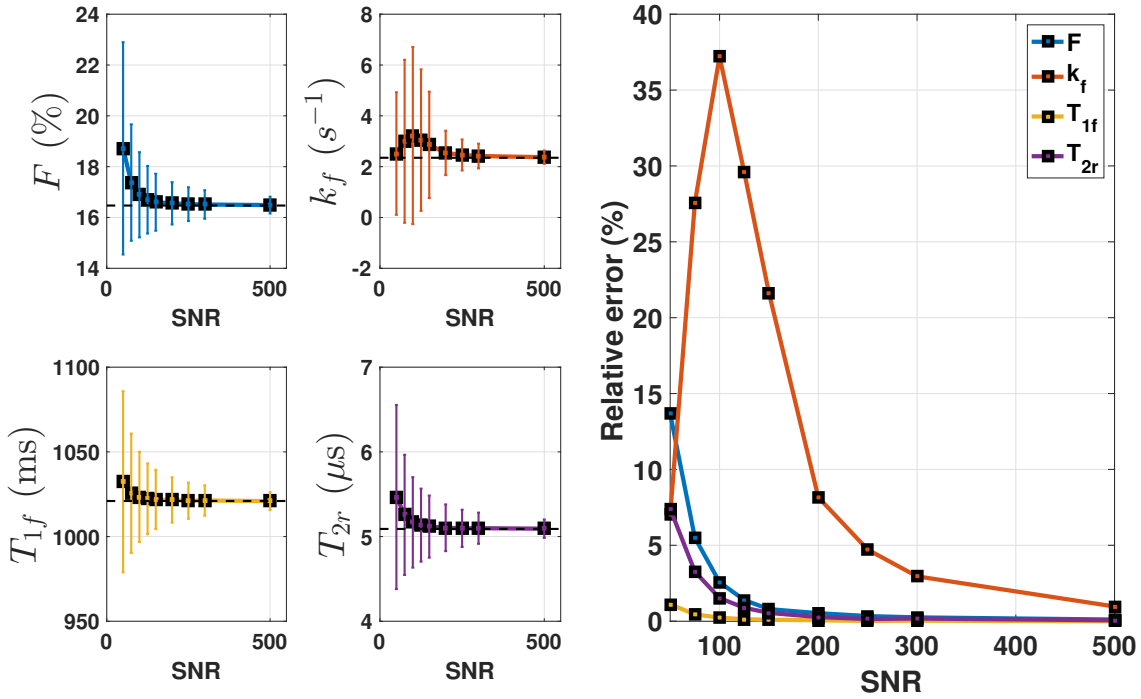

Figure 3.3 – Results of simulations evaluating the accuracy and precision of mean MT parameters as a function of the SNR for a model of cartilage. Left : mean values and standard deviation of parameters at each SNR, with the true value identified with a dashed black line. Right : absolute percentage relative error calculated from the true simulation parameters.

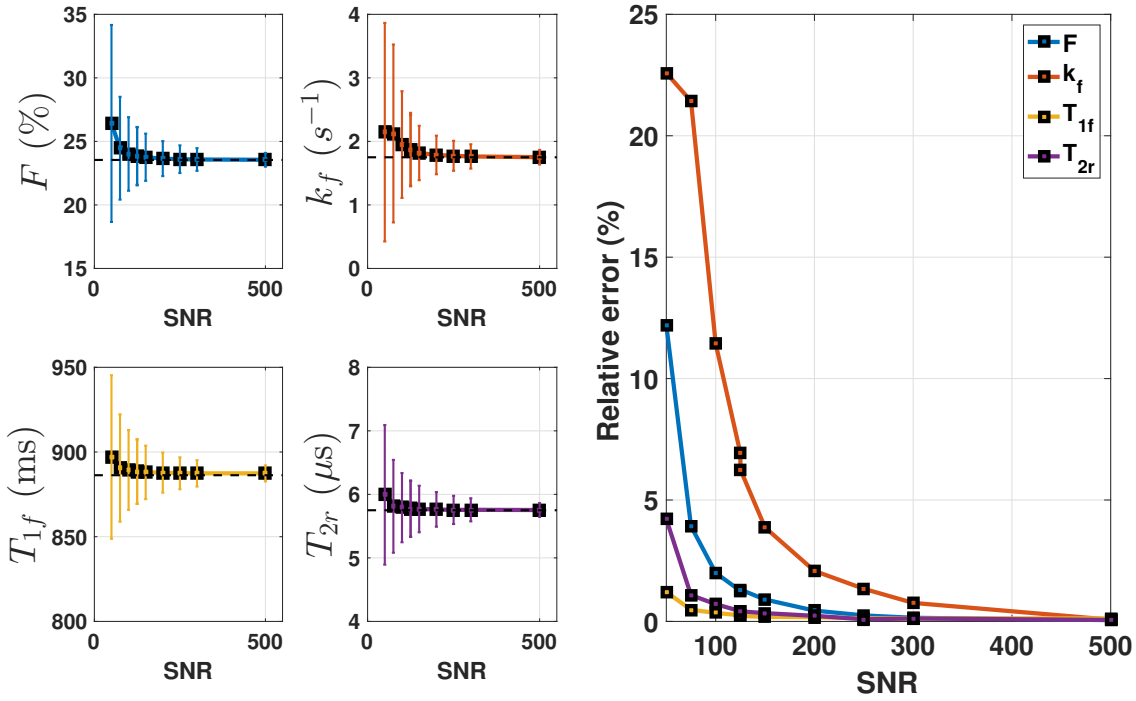

Figure 3.4 – Results of simulations evaluating the accuracy and precision of mean MT parameters as a function of the SNR for a model of meniscus. Left : mean values and standard deviation of parameters at each SNR, with the true value identified with a dashed black line. Right : absolute percentage relative error calculated from the true simulation parameters.

A major difference between figures 3.3 and 3.4 is that the bias introduced by noise as a function of SNR is systematically higher for all MT parameters in simulations of cartilage than in those of meniscus. More specifically, there are two important characteristics that can be observed at the observed SNR of 100.

First, all fitted QMT parameters (F, k_f, T_{1f}, T_{2r}) are overestimated in the presence of noise. For simulations in cartilage, parameters are overestimated respectively by 2.6, 37.2, 0.2, and 1.5%. The overestimation is 2, 11.4, 0.2, and 0.7% for the simulations in meniscus.

Second, for cartilage simulations in the range of SNR between 50 and 100, the relative error on k_f exhibits strange behaviour. The error is lowest at SNR = 50, increases until SNR = 100 is reached, and then decreases as the SNR increases towards 500. There are two opposed effects in this behaviour. First, increasing the SNR leads to an increase

both in the precision and accuracy of the fits : this lowers the error with increasing SNR, as is observed for all other parameters. Second, at lower SNRs, the outlier removal technique removed a larger percentage of voxels with k_f that become increasingly unstable at low SNRs, leaving a smaller portion of fitting results that converge to values closer to the truth. For cartilage and meniscus respectively, 25% and 11% of voxels are removed at a SNR of 50, while 7.8 and 1.5% of voxels are removed at a SNR of 100. Because large values of k_f are more often detected as outliers by the algorithm, a lower SNR leads to the removal of a larger number of high-valued k_f, which artificially decreases the mean k_f. At a low SNR of 50, the overestimation due to noise is compensated by the removal of a high percentage of outliers and the final QMT parameter is smaller. This behaviour is less noticeable for menisci simulations, where fewer outliers are removed.

In other words, the estimation of k_f at low SNR for cartilage simulations is not better : the apparent increase in precision and accuracy is caused by the removal of 25% of voxels due to unstable solutions. Furthermore, estimates of all other QMT parameters are worse at low SNR, which means that a lower SNR should not be used.

At an SNR of 100, it is shown that estimates of F, T_{1f} and T_{2r} are robust, with errors due to noise smaller or equal to 2.6% for cartilage and meniscal tissues. The simulations demonstrate that fits of k_f are not robust. This might be explained partially by an inability of the model to constrain k_f in the presence of noise with the current sampling. Indeed, in section 3.3.6, it is shown that k_f can be more robustly fitted with a different sampling scheme.

3.3.3 Discussion : robustness to noise

It was noted that the systematic overestimation of QMT parameters due to noise is lower for menisci simulations than cartilage simulations, for all parameters. The major difference in mean QMT parameters between the two tissues is the much higher semi-solid pool size ratio F for the meniscus : 23.5% against 16.5% , a relative difference of 42%.

A larger F means more magnetization transfer between pools and consequently a more reduced signal in the Z-spectrum, or higher MTR. A reduced signal in the Z-spectrum means a higher signal difference from non-MT signal. Therefore, for tissues with similar k_f and T_{2r}, the one with the highest F intrinsically provides more signal difference, and thus a higher apparent SNR, which can lead to a more accurate estimation of QMT parameters in such tissues. The confidence in QMT parameters appears to be intrinsically higher in meniscal tissue, richer in macromolecular content.

Following the observations in figures 3.3 and 3.4, one must be aware of the bias introduced by noise if comparing mean QMT parameters through different studies, which might be acquired at different SNRs, as the degree of overestimation is SNR-dependent. The current observations also motivate the removal of low SNR pixels described in appendix B for the *ex situ* menisci. In effect, a fair comparison of *in situ* and *ex situ* menisci, which is the main point of chapter 4, must be done with similar SNR distributions in the datasets. In the analysis, we want to remove extra variability that might be explained by different SNRs.

The odd behaviour of k_f in figures 3.3 and 3.4 can possibly be explained by the fact that lower SNR results in bimodal fit results, with one group of fits close to the true value, and one group of fits at exceedingly high error. As the SNR increases, these groups come together and merge into a single mode.

Any comparison between values of k_f in this work (such as cartilage vs. meniscus or *in situ* vs. *ex situ* meniscus) is tarnished by the high variability of this parameter with the current scheme. In addition, as it will be discussed in section 3.3.4, variability in the fixed ratio T_{1f}/T_{2f} between specimens adds extra variability to k_f. This limits the interpretation of changes in k_f between specimens. Nonetheless, the sampling scheme used provides an accurate estimation of all other MT parameters at an SNR of 100, which can be achieved clinically.

3.3.4 Results : variability of QMT parameters with T_{1f}/T_{2f}

To evaluate the impact of fixing T_{1f}/T_{2f} , the cadaver specimens (N=4, *in situ*) were analyzed using a range of ratios. Specimens were prepared and data were acquired as described in section 4.2. As discussed previously, in cartilage, the potential range of ratios is estimated to be within 29 ± 10, and 81 ± 10 in meniscus. Figures 3.5 and 3.6 show the variation for cartilage and meniscus, respectively.

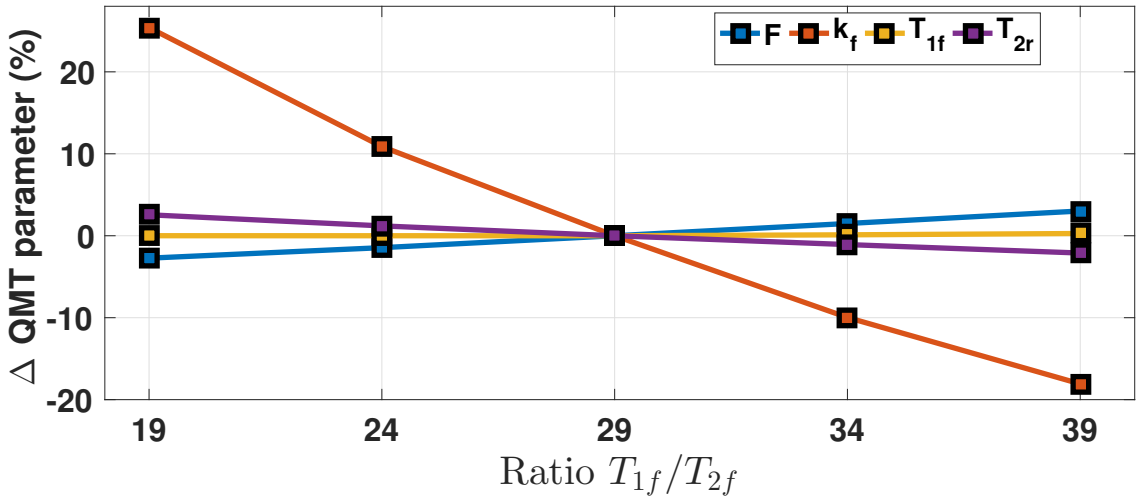

Figure 3.5 – Variation of mean QMT parameters in the whole cartilage (averaged over 4 specimens) for a range of T_{1f}/T_{2f} ratios. The percent variation is reported relative to the value with the best estimate of the ratio (=29).

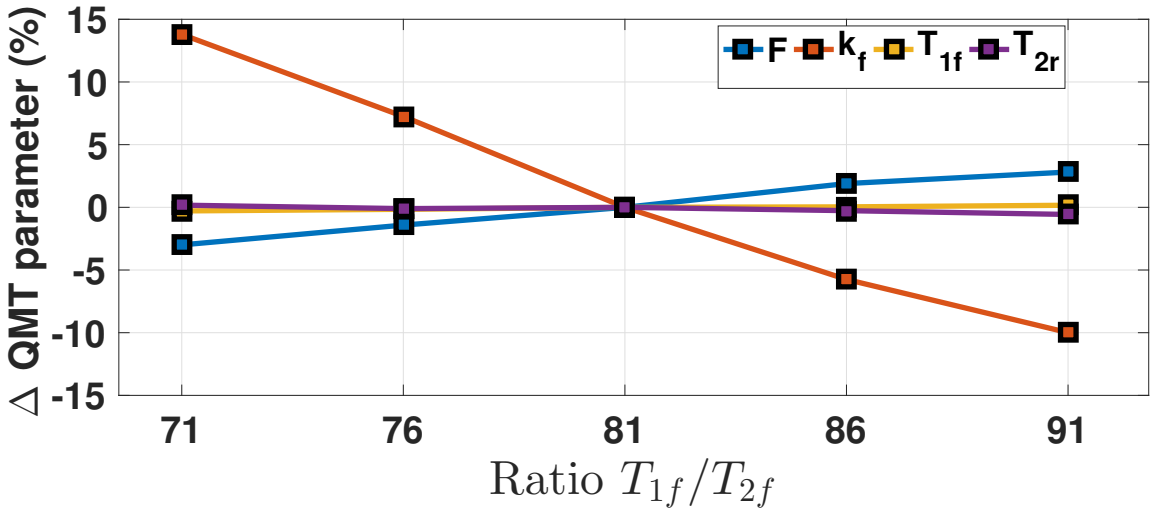

Figure 3.6 – Variation of mean QMT parameters in both menisci (averaged over 4 specimens) for a range of T_{1f}/T_{2f} ratios. The percent variation is reported relative to the value with the best estimate of the ratio (=81).

When the ratio is incorrectly estimated by ±10 in cartilage and meniscus, the mean F shows a relative variation respectively of ±2.5% and ±4%, while T_{1f} vary by less than 1%. For T_{2r}, the variation is less than 1% for the meniscus data, while the variation is higher (± 2%) for cartilage. The exchange constant k_f is more severely affected by an incorrect ratio, with a variation of ±20% for both tissues. The variability of QMT parameters is not symmetric with respect to the best estimate of the ratio : the variation is smaller for larger ratios.

It is unclear, however, if the variability observed in QMT parameters is intrinsically due to the RP model of MT or is a consequence of the specific sampling scheme use in this study. In other words, another sampling scheme with the same model might lead to a different variability in QMT parameters with respect to the fixed ratio. To answer these questions, Monte Carlo simulations were performed with the numerical MT models of the cartilage and the meniscus described in section 3.3, but this time with 3 different samplings of the Z-spectrum, detailed in table 3.4. Experiment 1 is the sampling scheme used in the rest of this work. Each experiment was done for the cartilage numerical phantom at ratios of 19, 29 and 39, and also for the meniscus numerical phantom at ratios of 71, 81 and 91.

Table 3.4 – Parameters used in Monte Carlo simulations to evaluate the impact of the ratio and the sampling scheme on QMT parameters estimates. Experiment 1 is the current sampling scheme, experiment 2 and 3 are inspired by the sampling schemes of [6] and [7], respectively.

Experiment	Sampling Scheme	MT sequence
1	Δ = 1.5/3.5/7.8/17.8/40.5 kHz at α_{MT} = 300,400°	8 ms Fermi pulse TR/TE/FA = 38/3/10
2	Δ = 2.5/5 kHz at α_{MT} = 890°, and Δ = 2.5/5/10/20 kHz at α_{MT} = 1550°.	18 ms Fermi pulse TR/TE/FA = 42/3.2/13
3	Δ = 3/9/15/21 kHz at α_{MT} = 670°.	8 ms Fermi pulse TR/TE/FA = 32/4/10

Figure 3.7 presents the variability of QMT parameters with different ratios and sampling schemes, for the cartilage simulations only, as similar results were obtained for the me-

niscus simulations.

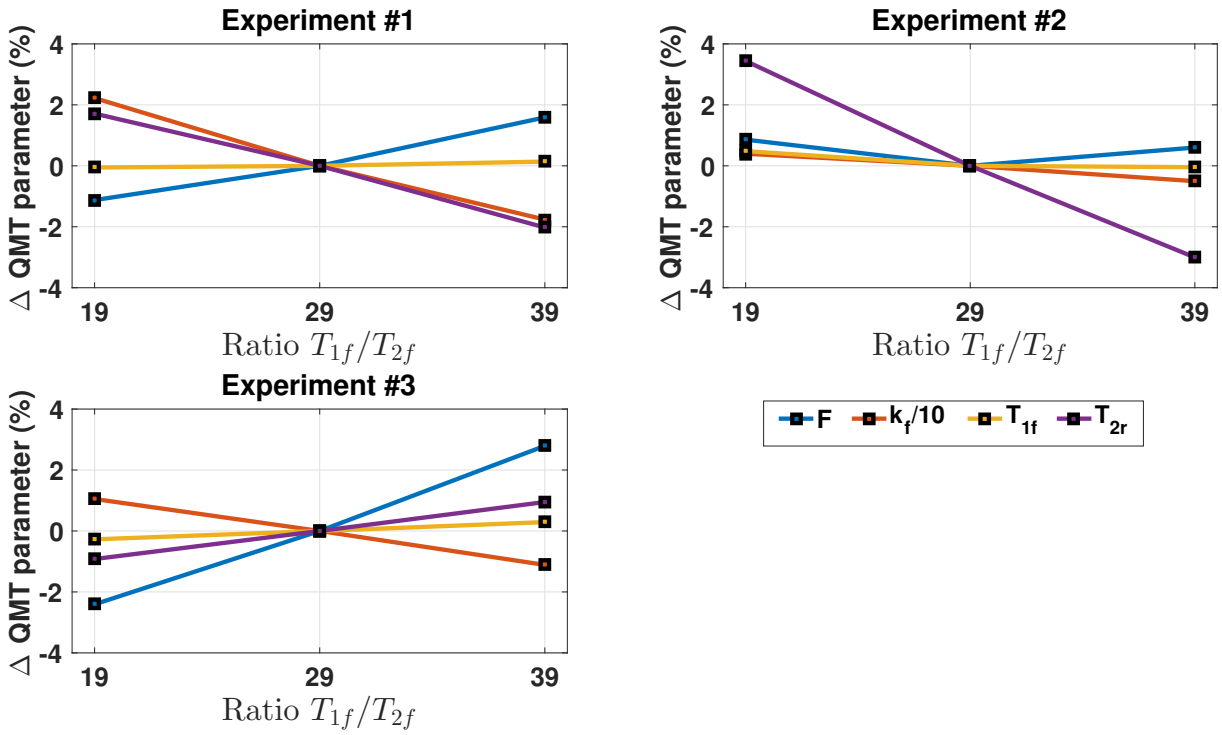

Figure 3.7 – Variation of mean QMT parameters in simulated cartilage for a range of T_{1f}/T_{2f} ratios, reported in the same manner as figure 3.5. The variation is presented for the three different sampling schemes of table 3.4. Note that the error on k_f was divided by 10 to allow a direct comparison of the sampling schemes.

First, from figure 3.7, we noted that the variability of QMT parameters differs significantly with the sampling scheme used. Second, the impact of the choice of T_{1f}/T_{2f} on QMT parameters changes considerably with the sampling scheme used. In experiment #2, the variability of k_f is reduced to less than 5%, as opposed to 20% in the current study. The variability of F is also reduced, at the price of twice the variation in T_{2r}. The variability is also different for most QMT parameters in experiment #3.

3.3.5 Discussion : variability of QMT parameters with T_{1f}/T_{2f}

Because T_{2f} is generally smaller than T_{2obs} [17], the ratio T_{1f}/T_{2f} obtained using the mean T_{2obs} as an estimate for T_{2f} is underestimated. According to figures 3.5 and 3.6, this means that, in addition to an overestimation of all QMT parameters due to noise, there is :

— an overestimation in k_f (0 to 20%) and T_{2r} (0 to 2%) due to the biased T_{1f}/T_{2f} ;

— an underestimation of F (0 to 4%) and T_{1f} (0 to 1%) due to the biased T_{1f}/T_{2f} .

Combining noise and fixed ratio effects, this leads overall to an overestimation of k_f and T_{2r} because both effects are biased positively. For F and T_{1f}, because the bias in T_{1f}/T_{2f} and the noise have opposed effects on these parameters, the overall behaviour is unclear and will depend upon the relative importance of each bias. For example, if the bias in the ratio is close to +10, then the biases approximately cancel out in simulations and the estimates of F and T_{1f} are more accurate. However, if the bias is larger than +10, then these two parameters will be underestimated.

The previous observations can be summarized as follows. At a SNR of 100, with the current sampling scheme and knowing that the ratio T_{1f}/T_{2f} is underestimated,

— F and T_{1f} will be underestimated. The magnitude of the bias increases with the bias in the ratio. We do not currently know the bias in this ratio.

— k_f and T_{2r} will be overestimated. This overestimation increases with the bias in the ratio.

This behaviour does not hold for different sampling schemes, as shown in figure 3.7.

It is apparent from figure 3.7 that sampling schemes that use higher MT powers and longer MT pulses, which leads to higher flip angles, show a greatly reduced variability for k_f, and that an optimal scheme that would minimize the variability of all parameters with respect to T_{1f}/T_{2f} could be eventually obtained by exploring different sampling schemes. The difference between MT signal and baseline is greatly enhanced when using higher saturation power and longer saturation pulses and this might stabilize the fits of k_f. This might explain in part why the variability of the exchange rate constant is reduced with respect to the ratio in higher power schemes. There is a compromise, however, in high power schemes and the maximum SAR in MRI experiments. A more global approach to evaluate the impact of the sampling scheme (MT offsets and powers) is required, as has

been proposed for brain tissue [85].

A consequence of the large variability of k_f with the actual sampling scheme is that differences in k_f that would arise in different samples that might be interpreted as physiological changes in the macromolecular content might be, in fact, caused by the variability of T_{1f}/T_{2f} between specimens. This would also suggest that, in addition to the acquisition of VFA data to map T_{1f}, T_2 mapping in cartilage and menisci may be required to investigate the variability of the ratio in these tissues. Until more studies are performed to quantify T_{2f} in cartilage and menisci, it is good practice to evaluate the variability of QMT parameters with the fixed ratio in a given sampling scheme. Alternatively, one must use a sampling scheme that is minimally sensitive to the choice of the ratio.

In addition, comparing mean QMT parameters between studies that use different sampling schemes and possibly different fixed ratios can be difficult due to the impact of the chosen ratio and sampling scheme on parameters estimates.

Overall, the possibly large variability in QMT parameters with the fixed ratio is not inherent to the RP model of MT, but a consequence of a sub-optimal scheme. In future studies, it is strongly recommended to follow one of the three suggestions that follows. One can either 1) use a scheme that can provide stable fits of T_{2f}, 2) provide robust estimates of T_{2f} to increase confidence in the fixed ratio or 3) use a sampling scheme minimally sensitive to T_{1f}/T_{2f} .

3.3.6 Results : variability of QMT parameters with the sampling scheme

In this project, a semi-logarithmic sampling scheme (for the offset frequencies) was used to cover the Z-spectrum. This has been the practice in previous work [4, 17, 29]. Because of the nonlinear nature of the model, the sampling scheme has an impact on the precision and accuracy of the quantitative parameters estimated. Through optimal design,

it is possible to find an optimal sampling scheme that might, for example, minimize the intrinsic variance of the estimated parameters. This section is not on optimization *per se*, but an exploration of the impact of different sampling schemes on the QMT parameters and might help in recommending what general trends in sampling schemes should be followed to produce robust fits of QMT parameters in the knee joint.

As noted in figure 3.7, the sampling scheme was shown to have a noticeable impact on the accuracy of QMT parameters. Here, we evaluate the intrinsic accuracy and precision of Sled & Pike's model of MT with different clinically used sampling schemes. We use the same acquisition parameters as described in table 3.4 and reproduce figure 3.5, the robustness to noise of the fitting algorithm for a simulated cartilage phantom, with the two other sampling schemes. A similar study was made using a simulated meniscus phantom, but is not shown for brevity, as the conclusions were similar.

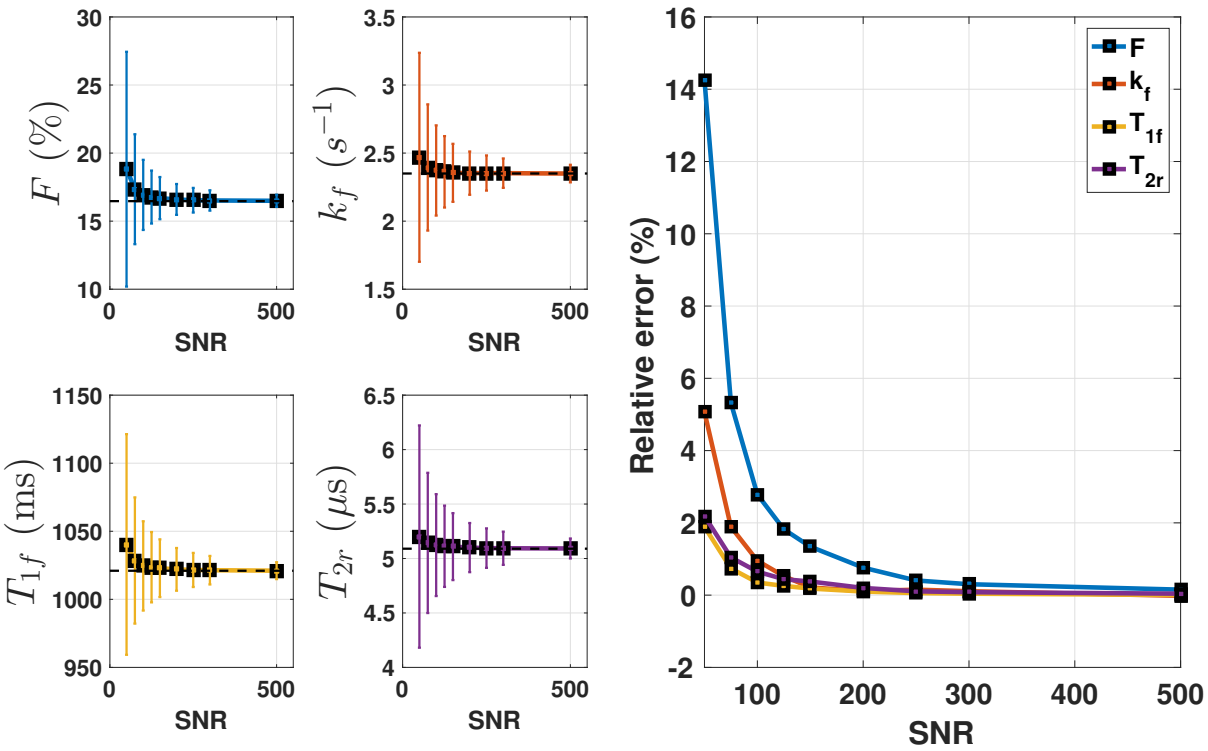

Figure 3.8 – Simulations (for a model of cartilage) evaluating the accuracy and precision of QMT parameters estimates with the sampling scheme of experiment # 2.

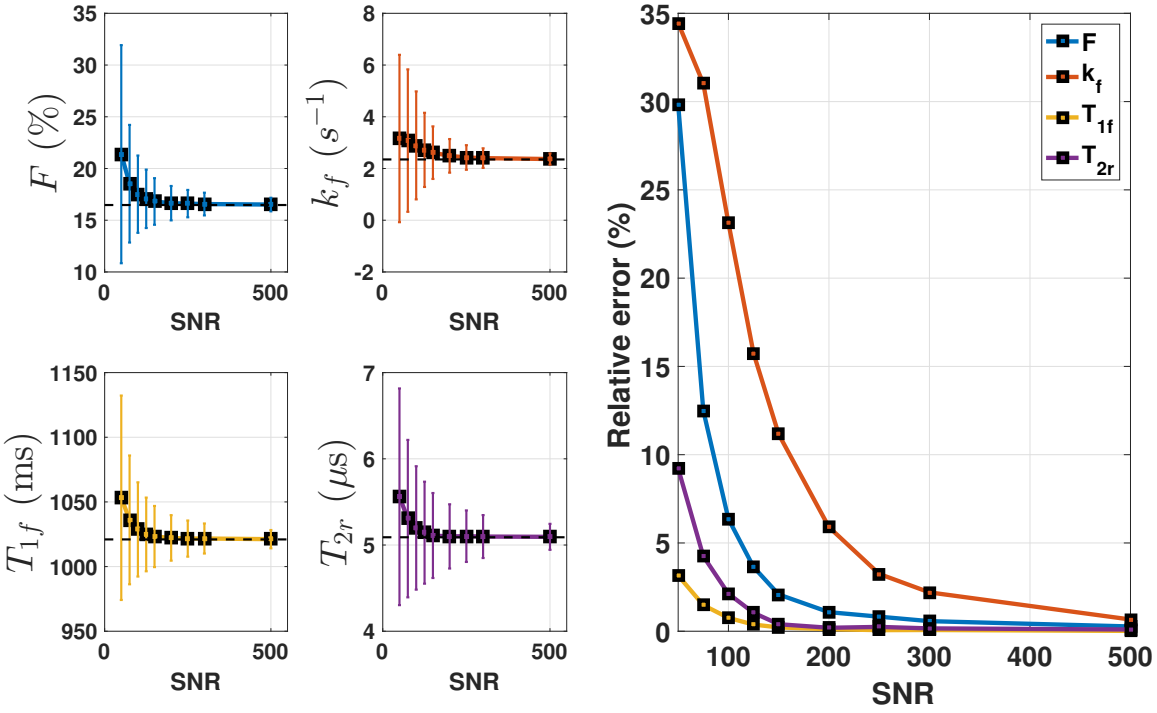

Figure 3.9 – Simulations (for a model of cartilage) evaluating the accuracy and precision of QMT parameters estimates with the sampling scheme of experiment # 3.

Experiment #3 was much less accurate and precise than the other two schemes for all SNRs. For experiment #2, the accuracy of k_f and T_{2r} increased. The precision is also higher for k_f. These characteristics are obvious when considering the distributions of QMT parameters in the three experiments in figure 3.10.

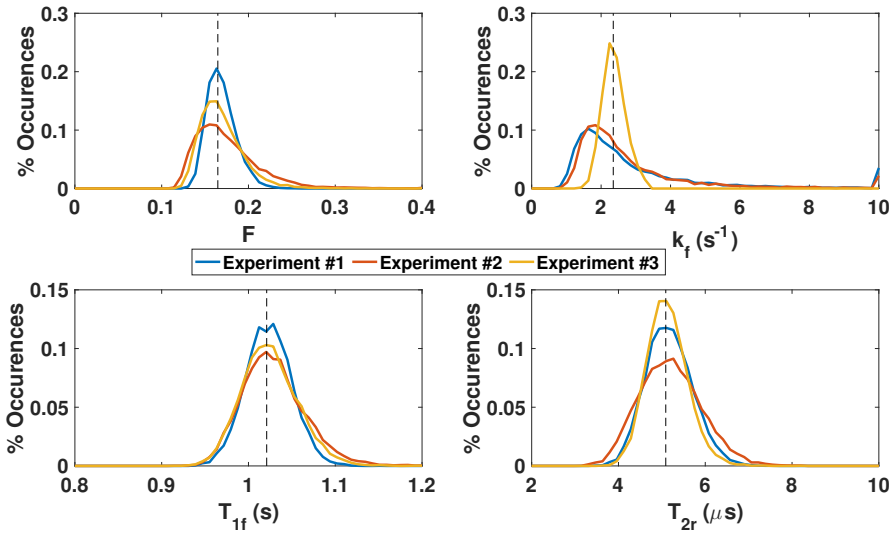

Figure 3.10 – Distribution of QMT parameters from Monte Carlo simulations using different sampling schemes. The real value is identified with a black dashed line.

3.3.7 Discussion : variability of QMT parameters with the sampling scheme

While the scheme used in this study (experiment #1) provides a slightly more precise and accurate fit of F than the other schemes, the scheme used in experiment #2 provides more accurate and precise fits of k_f and T_{2r}. It is of interest to note that the scheme in experiment #2 uses much higher MT pulse power and duration than the other schemes. A compromise between experiment #1 and #3, where a slightly reduced number of Z-spectrum points (less than 10) combined with the acquisition of data at higher MT powers seems promising and could lead to a potential reduction in scan time while conserving (or increasing) fit quality. Levesque *et al.* [97] recommend to use a minimum number of seven points in the Z-spectrum to obtain robust fits. This is consistent with the conclusions obtained here.

Experiment #2, which uses high MT powers (flip angles of 890 and 1550°) and a longer MT pulse duration provides the most accurate and precise QMT parameters estimates, although it uses fewer data points (8 vs 10) than the current sampling scheme. The 4-point scheme (experiment 3) does not perform well, possibly because the use of 4 points in the Z-spectrum cannot lead to robust fits of all QMT parameters [97].

Applying optimum design techniques in MT to optimize the sampling scheme in order to minimize the variance of QMT parameters has previously been done for brain [97, 85]. This might be required in cartilage and meniscus data, where QMT parameters considerably differ from brain. Since the sampling scheme optimization requires a specific set of QMT parameters to be performed, an optimal scheme in cartilage and meniscus is likely to differ from brain. The basic concepts for an optimization framework as well as preliminary results showing optimal schemes are presented in chapter 5.

3.4 Conclusion

A modified technique for QMT estimation based on the RP model of Sled and Pike for pulsed MT experiments was presented, where T_{2f} is fixed to a specific ratio of T_{1f} and QMT parameters F, k_f, T_{1f} and T_{2r} are obtained by joint fitting of the VFA and MT-SPGR datasets. Overall, it was shown that a robust estimation of T_{1f}, F and T_{2r} is possible in the current study and that sources of error such as noise and biased fixed T_{1f}/T_{2f} have a minimal impact on those parameters. This is the main point of the current chapter and validates the use of this modified QMT algorithm for the knee specimen datasets in chapter 4.

At a SNR of 100, achieved for the cadaver study (described in detail in section 4.2), it was shown that the modified model can produce robust and slightly overestimated estimates of F,T_{1f} and T_{2r}, with errors due to noise being smaller or equal to 2.6% for cartilage and meniscal tissues. Simulations have shown that the fits of k_f are not as accurate and show more variability. This might be explained partially by an inability of the model to constrain k_f in the presence of noise with the current sampling scheme.

Because T_{2f} is typically smaller than T_{2obs} [17], the ratio T_{1f}/T_{2f} is possibly underestimated. Combining the effects of noise and underestimation of T_{1f}/T_{2f} lead to overall underestimated F and T_{1f}, while k_f and T_{2r} are overestimated. The magnitude of the bias (overestimation or underestimation) cannot be quantified without reference T_{2f} values in joint tissues. As such, another important conclusion from this chapter is that the evaluation of T_{2f} in joint tissues will be critical for future QMT studies in these tissues.

It was shown that the amount of bias in QMT parameters is highly dependent on the sampling scheme and could be reduced with an optimal scheme. Indeed, using MT pulses at higher flip angle and pulse duration greatly reduced the variability in k_f, even for a lower number of acquired Z-spectrum points. The optimization of the Z-spectrum sam-

pling scheme will be explored further in chapter 5. For future studies, it seems mandatory to use a more optimal sampling scheme.

Finally, an important point discussed was that apparent changes in QMT parameters, which might be associated to variation in the ultra-structure and composition of tissues, could instead be a reflection of local variations in T_{2f} in tissues, as the value of T_{1f}/T_{2f} influences other QMT parameters. This is especially important for k_f, which was shown to vary largely with the fixed ratio in this work. One must then consider that local variation of T_{2f} in tissue might explain in part differences in QMT parameters in this study.

4

Quantitative magnetization transfer of *in situ* and *ex situ* knee meniscus

Preface

The core of this thesis consists of the manuscript :

Mikaël Simard, Emily J. McWalter, Garry E. Gold and Ives R. Levesque. "Quantitative magnetization transfer of in situ and ex situ knee meniscus".

At the time of writing, this manuscript is in preparation for submission to the journal *Magnetic Resonance in Medicine*. The methods section of this manuscript contains repetitive information from chapters 2 and 3, as the same datasets were used in the analysis.

Ethics approval was not required for this work on cadaveric specimens, as detailed in appendix D.

Quantitative Magnetization Transfer Imaging of *In Situ* and *Ex Situ* Knee Meniscus

Mikaël Simard[1], Emily J. McWalter[2,3], Garry E. Gold[2], Ives R. Levesque[1,4,5*]

1 Medical Physics Unit, McGill University, Montreal, QC, Canada.

2 Radiology, Stanford University, CA, United States.

3 Mechanical Engineering, University of Saskatchewan, SK, Canada.

4 Physics, McGill University.

5 Research Institute of the McGill University Health Centre.

** Correspondence to :*

Ives R. Levesque, PhD

Medical Physics Unit, McGill University

Cedars Cancer Centre - Glen Site, DS1.9327

1001 boul. Décarie

Montréal, QC H4A 3J1

ives.levesque@mcgill.ca

514-934-1934 ext. 43739

In preparation for submission to Magnetic Resonance in Medicine

Abstract

Purpose : Quantitative magnetization transfer (QMT) probes macromolecular content in tissue and might be a useful tool in the early detection of cartilage and meniscal degeneration, which are hallmarks of osteoarthritis. For QMT metrics to be used as potential biomarkers of early joint degeneration, extensive comparisons with histology and biochemical markers must be carried out. This can be done with cadaveric knee specimens. To carry out such analyses, cartilage and meniscus tissues must be extracted and conserved from the specimens before scanning. A first step towards the validation of QMT metrics consists of quantifying the impact of extracting and conserving joint tissues while the QMT analysis is to be performed in situ for validation purposes with cadaveric specimens.

Methods : QMT mapping of lateral and medial menisci was performed in 4 cadaver knee specimens *in situ*, and repeated *ex situ* following dissection and immersion in perfluorooctyl bromide (perflubron). QMT parameters of articular, patellar and femoral *in situ* cartilage were also obtained.

Results : After extraction and immersion in perflubron, a statistically significant decrease in the restricted pool fraction F was noted, while there was a statistically significant increase of the relaxation parameters T_{1obs} and T_{1f}. A trend towards lower values of the exchange constant, k_f, was noted after excision. T_{2obs} and T_{2r} were relatively constant. QMT parameters in cartilage *in situ* were comparable with other published values.

Conclusion : When comparing *in situ* and *ex situ* samples, a significant variation in F and T_{1f} can be expected and might be attributed to the diffusion of perflubron into the *ex situ* samples. Other QMT parameters were not significantly influenced by the extraction and immersion procedure.

Keywords : quantitative magnetization transfer ; cross relaxation imaging ; meniscus ; cartilage ; osteoarthritis.

4.1 Introduction

Osteoarthritis (OA) is a degenerative joint disease that leads to joint pain, stiffness and loss of function. OA can be described as a multifactorial disease involving biomechanical disorders, and a combination of biochemical, inflammatory and immunology responses [36, 37, 38, 39]. A hallmark of OA is the loss and erosion of articular cartilage and meniscal degeneration and tearing. In addition, there is no known cure and only limited treatment options for OA [40]. Recent research has shown that knee OA involves the degeneration of not only the cartilage in the joint, but also other of structures such as subchondral bones, ligaments, muscles and menisci [47].

Early OA is characterized by changes in the macromolecular structure of cartilage, specifically an increase in water content, a loss of proteoglycans (PGs) and a disruption of the collagen fiber network [42, 43, 44, 45]. There is significant interest in developing techniques that can be used as early biomarkers of OA, as this will allow the development and evaluation of new treatments for this debilitating disease [46].

Conventional magnetic resonance imaging (MRI) and plain radiography are already widely used clinically to assess articular cartilage damage, gross joint morphology changes, and meniscal tears [49]. However, as these macroscopic degenerative changes are typically absent in early stages of OA, other techniques must be used to detect early OA. These techniques must have the capacity to probe the microscopic structure and composition of the joint tissues, as changes in their ultra-structure and composition may be indicative of early OA [46]. This can be challenging : macromolecules such as collagen and PGs have very short T_2 relaxation time owing to the bound protons in the macromolecules [49], which makes their direct observation difficult in conventional MRI.

The menisci are crescent-shaped fibrocartilaginous structures attached to the tibial plateau and are mostly composed of water, circumferentially oriented collagen fibers and PGs [47]. It is expected that the pathological processes which cause early OA in the joint should not be limited only to cartilage and might affect the meniscal tissues equally, as the tissues share similar components, properties and are subject to similar mechanical load [47]. Thus, in addition to evaluating the health of the articular cartilage, assessing the degradation of the menisci is of interest for early OA detection.

There are multiple quantitative MRI techniques that can assess the microscopic structure and composition of the joint by increasing the dependence of the MRI signal to macromolecular content, specifically PGs and collagen. Techniques such as $T_{1\rho}$ relaxation imaging [50, 51, 52, 53], delayed gadolinium-

enhanced MRI of cartilage (*dGEMRIC*) [54, 55, 56], sodium imaging [57, 58, 59, 60, 61] and chemical exchange-dependent saturation transfer (CEST) imaging [62, 63, 64, 58] have all been shown to be sensitive to the PG content in cartilage, while other techniques such as T_2 mapping [65, 66, 67], diffusion MRI (specifically diffusion weighted imaging (DWI) [68, 69, 71] and diffusion tensor imaging (DTI) [72, 73]) are sensitive to the ultra-structure (orientation and content) of collagen.

Current quantitative MRI methods to assess the ultra-structure of collagen have their limitations. Interpretation of changes in T_2 values is ambiguous due to the number of competing processes that influence the nonspecific parameter T_2. It was suggested [74] that 60% of the variation in T_2 can be attributed to changes in collagen fibril orientation (following the magic angle effect [75]) and organization, while the remaining 40% is determined by a combination of changes in water content and concentration of other macromolecules [46]. For *in vitro* cartilage studies, different types of immersion fluids used to preserve human tissue before imaging might influence T_2 relaxation times Presently, DTI is limited for the *in vivo* evaluation of cartilage due to long acquisition times and intensive data analysis [46].

Magnetization transfer (MT) MRI is a technique that can probe the macromolecular content of tissues, which is typically unobservable in conventional MRI, as the signal produced by protons bound in macromolecules decays on the order of microseconds. The MT effect enables us to visualize the non-aqueous macromolecular content in tissues by exploiting to the exchange of magnetization between the restricted (or semi-solid) pool of protons contained in macromolecules, and the free pool of protons (in mobile water), which occurs mainly through dipolar interactions and proton chemical exchange. It has been shown that the contributors to the MT effect in cartilage are collagen [77, 78], and PGs [78]. As the MT signal is sensitive to collagen ultra-structure and content [77] as well as the PG content [78], it is an interesting candidate for the non-invasive assessment of cartilage and meniscal tissues.

Quantitative MT (QMT) MRI is a technique to quantify the MT effect. QMT can provide insights on the macromolecular content of tissues through physically meaningful parameters extracted from a quantitative model of MT. In QMT, a two-pool model with transfer of magnetization between the free and restricted pools is fitted to provide physical quantities characterizing both pools and their interaction. This includes the size of the macromolecular proton pool, the restricted pool size ratio F (sometimes referred to as the bound pool fraction) and the first-order rate of magnetization exchange from the free to the restricted pool, k_f. QMT also provides the T_1 and T_2 relaxation times of the free (T_{1f}, T_{2f}) and restricted (T_{1r}, T_{2r}) pools of protons. F is believed to be an indirect measurement of the macromolecular content, while k_f and T_{2r} are respectively indicative of, 1) the efficacy of MT between the two proton pools, which is related to the nature and organization of macromolecules and, 2) the diffusion

of magnetization between proton sites in macromolecules, related to the ultra-structure [6, 28, 17, 80]. The relaxation time of the bound pool, T_{2r}, has also been interpreted as a measure of the rigidity of the macromolecular structure [24].

Preliminary QMT studies have been performed in cartilage, mostly *ex vivo*. Li *et al.* have shown that F is strongly correlated with the GAG content in tissue-engineered cartilage [81]. Stikov *et al.* have shown that moderate correlations exist between F and PG content and between k_f and collagen in articular cartilage extracted from cadaveric knee specimens, concluding that these MT parameters can be used as biomarkers to evaluate PG and collagen content in cartilage [7]. More recently, Sritanyaratana *et al.* have shown that patients with OA have significantly lower k_f and significantly higher T_{2r} values in patellar cartilage than asymptomatic volunteers, suggesting that QMT parameters can detect changes in the macromolecular component of degraded cartilage *in vivo*, but that further studies are needed to understand the mechanisms responsible for QMT changes in patients with OA [6].

For QMT metrics to be used as biomarkers of early joint tissue degeneration, comparisons with histology and biochemical markers must be carried out. Currently, either whole cadaveric knee specimens or menisci obtained from total knee replacement surgeries can be used to correlate quantitative MRI with biochemical and histological markers. To carry out such analyses, the tissues of interest are first extracted from the knee sample. Then, these extracted specimens are often immersed in hydrogen-free fluids such as perflubron (perfluorooctyl bromide) for imaging to avoid compromising the dynamic range in the image and limit tissue-air susceptibility artefacts, or typically in phosphate-buffered saline (PBS) solutions [7]. As such, a first step for the validation of QMT metrics consists of quantifying the impact of extracting and immersing joint tissues, as histology and biochemical studies are performed *ex situ*, while the QMT analysis will ultimately be performed *in vivo*.

Additionally, most QMT studies concerning the knee joint have been performed on cartilage, and it is of interest to cover other joint tissues such as the menisci, which is also affected by early OA. Therefore, in this study, our interest was both in QMT of meniscal tissue and cartilage. Our hypothesis was that measuring QMT model parameters in the different setups (*in situ* and *ex situ*, in perflubron) would yield the same parameters. Our objectives were to 1) perform measurements of QMT parameters of menisci *in situ* (from whole cadaver knee specimens) and *ex situ* (extracted menisci in perflubron) to evaluate the impact of the extraction and conservation procedure and 2) evaluate QMT parameters of the articular cartilage *in situ* from the same cadaveric knee specimens in order to compare with published values to evaluate the QMT processing technique used in this work.

4.2 Methods

4.2.1 Data Acquisition

Magnetization transfer (MT) MRI data were acquired for four complete cadaver knee specimens with no history of musculoskeletal disorders (Anatomy Gifts Registry, Hanover, MD) at 3 T (GE MR 750, GE Healthcare, Waukesha, WI). Specimens were received frozen, and were thawed and scanned. Then, the menisci from the specimens were excised and immersed in perflubron for *ex situ* scanning. Specimens were scanned using a 16-channel receive-only coil (*in situ*) and a single channel surface coil (*ex situ*). A small agar phantom was included in the field-of-view of the *ex situ* specimens to increase the overall signal to enable the automatic scanner adjustments to complete sucessfully. All data were acquired with a spoiled gradient echo (SPGR) sequence (FA =10°, FOV = 160 × 160 mm^2, TR/TE=48/3 ms, 0.625 × 0.625 in-plane resolution) and a MT sensitizing pre-pulse (Fermi pulse of duration 8 ms). Slice thickness was different for the *in situ* and *ex situ* experiments : 3 and 2 mm, respectively. MT pulse flip angles of 300,450° and offset frequencies of 1.5, 3.5, 7.8, 17.8 and 40.5 kHz (semi-logarithmic sampling) were used for 10 total samples in the (α, Δ) sampling space (the Z-spectrum). The number of points in the Z-spectrum was set to 10 to balance between achieving a short acquisition time compatible with *in vivo* imaging and allowing a robust nonlinear fit with enough data points. We refer to the set of 10 MT weighted volumes at different offset frequencies and MT pulse angles as the sampling scheme. Three reference volumes were acquired with no MT pulse and averaged to normalize the MT data.

The observed T_1 (T_{1obs}) was mapped with DESPOT1 (utilizing a variable flip angle approach, VFA) [98], using a 3D spoiled gradient echo sequence (TR/TE = 20/3 ms) with four different flip angles (5, 10, 20, 30°). B_1 variations were mapped with the dual angle method [99].

4.2.2 Data Analysis

To produce QMT parameters maps, custom software was written (MATLAB 2016a, the MathWorks, Natick, MA) based on the rectangular pulse (RP) model of off-resonance saturation from Sled & Pike [17] modified for the Fermi pulse shape. A voxel-wise Levenberg-Marquardt (LM) nonlinear fit was used to find the best fitting QMT parameters. A constant T_{1r} of 1 s was assumed, as typically done in QMT studies due to the low sensitivity of the model to T_{1r} [6, 7, 17]. Following the observations of Mossahebi et al [35] that T_{1obs} estimation is biased in VFA experiments of macromolecular-rich tissues such as cartilage and meniscus due to MT, we fit simultaneously voxel-wise VFA and MT data to Sled and Pike's signal equation of MT, using a zero duration MT pulse for VFA measurements. This accounts

for MT effects in VFA measurements. Thus, instead of calculating T_{1f} analytically from an independent observation of T_{1obs} [4], T_{1f} is fitted conjointly with other QMT parameters. Because no normalization dataset was acquired for VFA experiments, a synthetic normalization volume was calculated for each specimen to normalize the datasets. The synthetic normalization volume is obtained as follows. For each voxel, the Ernst equation [14] was fitted with a nonlinear least squares algorithm to the VFA data, estimates of T_{1obs} and proton density S_0 were extracted and the maximum theoretical signal was evaluated at the Ernst angle. The VFA data were normalized voxel-wise by this maximum signal volume.

When fitting QMT parameters, it was observed that robust fits of F, T_{1f} and T_{2r} could be obtained, while the model was relatively insensitive to T_{2f} and less robust to k_f. To stabilize the fitting procedure, we reduced the number of free parameters in the RP model of MT by fixing T_{2f}. The final four QMT parameters calculated were F, k_f, T_{1f} and T_{2r}.

For T_{2f}, a typical practice is to fix T_{2f} to a specific ratio of T_{1f} [6, 7, 28]. Yarnykh and Yuan have discussed [83] that, in brain tissue, T_{2f} can be obtained voxel-wise by fixing the ratio T_{1f}/T_{2f} to a constant value, and have proposed $T_{1f}/T_{2f} = 18$. We use this approach with a different ratio, as the relaxation constants are different in brain and cartilage. A prior QMT study in the tibial and patellar cartilage [7] fixed the ratio to 20 based on their own observations of T_{1obs} and T_{2obs} in the specimens. However, T_{1f} can differ significantly from T_{1obs} [35], and T_{2f} from T_{2obs}, especially in tissues which are known to have multiple free water components where the mono-exponential fit of T_{2obs} is an inadequate representation of the proton pools in the tissue [17]. We obtained T_{1f}/T_{2f} through a direct fit of T_{1f} in cartilage and menisci and an estimation of T_{2f} through provided values of T_{2obs} in the literature.

We observed that T_{1f} estimates were essentially independent of the fixed value T_{1f}/T_{2f} . Thus, we propose the following procedure to estimate the average T_{1f} in a specific tissue. First, we fixed an approximate value of T_{1f}/T_{2f} based on observations of T_{1obs} in the tissues of interest and T_{2obs} from the literature. We fitted the data to the model using this initial ratio and evaluated the mean T_{1f} in each tissue of interest by averaging all specimens. The final average values of T_{1f} in cartilage, meniscus *in situ* and *ex situ* were respectively 883, 737 and 1314 ms.

The treatment of T_2 relaxation times is complex in tissues such as the cartilage and meniscus, known to have multiple free water T_2 components [86, 88, 89]. In this situation, it is unclear how to relate T_{2obs} and T_{2f}. Overall, T_{2obs} and T_{2f} can be interpreted as different weighted averages of the multiple free pools of water in tissues [17]. Because there are no published values of T_{2f} in the literature for cartilage or meniscal tissues and that the current dataset could not produce robust fits of T_{2f}, an alternative was

to replace T_{2f} by T_{2obs} knowing that a bias might be introduced through this approximation. In the literature, at 3 T, we found an average value of $T_{2obs} = 34.9 \pm 4.6$ for the cartilage by averaging 11 studies [100, 101, 102, 103, 104, 105, 106, 107, 108, 109, 110]. For the *in situ* menisci, an average value of $T_{2obs} = 11.0 \pm 0.5$ ms was obtained by averaging values from 4 references [109, 111, 112, 113] and a single value of $T_{2obs} = 20.2 \pm 5.3$ ms was obtained for the *ex situ* menisci (Chang 2015). The final ratios T_{1f}/T_{2f} used in this work were 67, 65 and 25 for the *in situ* menisci, *ex situ* menisci and whole cartilage.

Complete parameter maps were produced for *in situ* and *ex situ* specimens. Region-of-interest analysis was performed on meniscus and articular cartilage identified in the *in situ* images, obtained from a reference volume with no MT pulse. Medial and lateral menisci as well as femoral, patellar and tibial cartilage were segmented manually, in a slice-by-slice manner, for analysis purposes, in all specimens.

The surface coil for *ex situ* meniscus data provided a non-uniform SNR. Therefore, voxels for the *ex situ* meniscus with a SNR not comparable with the *in situ* meniscus were removed from the analysis to remove SNR variations as a source of differences in QMT parameters. The distribution of the SNR was evaluated [114] in both datasets and all *ex situ* voxels with a SNR lower than the first percentile of the *in situ* voxels SNR distribution were excluded from the analysis. This led to the removal of 40% of the voxels in the *ex situ* datasets.

Outliers were removed in the calculation of mean QMT values based on their error calculated from the trace of the variance-covariance matrix of parameters, obtained from the Jacobian at the solution. Voxels containing QMT parameters with an error 10 times the median QMT parameter in each ROI were removed from the analysis, as they indicated a highly unstable solution. A value of 10 times the median was chosen because 1) it is much higher than the maximum acceptable error on a fit and 2) choosing a different value (5 or 20 times the median) did not change final mean QMT parameters by more than 0.1% after outlier removal. This removed $\approx 5\%$ of all voxels, mostly containing physically unrealistic parameters such as values of F outside of the range [0, 1] and large, physically unrealistic k_f ($e.g. \leq 30s^{-1}$).

Statistical analysis

Differences in QMT parameters between the *in situ* and *ex situ* cases and lateral and medial menisci were determined using Friedman's two-way non-parametric test. This test was also used to evaluate differences between different ROIs in the cartilage and meniscus.

Variation of QMT parameters with depth

We investigated if QMT parameters varied with depth in tibial cartilage, as reported by Stikov *et al.* [7].

To map each tibial cartilage voxel to a relative depth in cartilage, the following analysis was done for every slice of each specimen. For every vertical line (in the direction top to bottom of the tibial cartilage), the surface was identified as a depth of 0, and the associated depth of each following vertical voxel was increased by the voxel size in this direction (0.625 mm) until the end of the cartilage is reached on the vertical line. By normalizing the depth of all voxels in a vertical line with the deepest in this line, the absolute depth can be transformed to relative depth.

4.3 Results

4.3.1 Comparison of *in situ* and *ex situ* menisci

QMT maps in the menisci before and after extraction are compared for one specimen in figure 4.1.

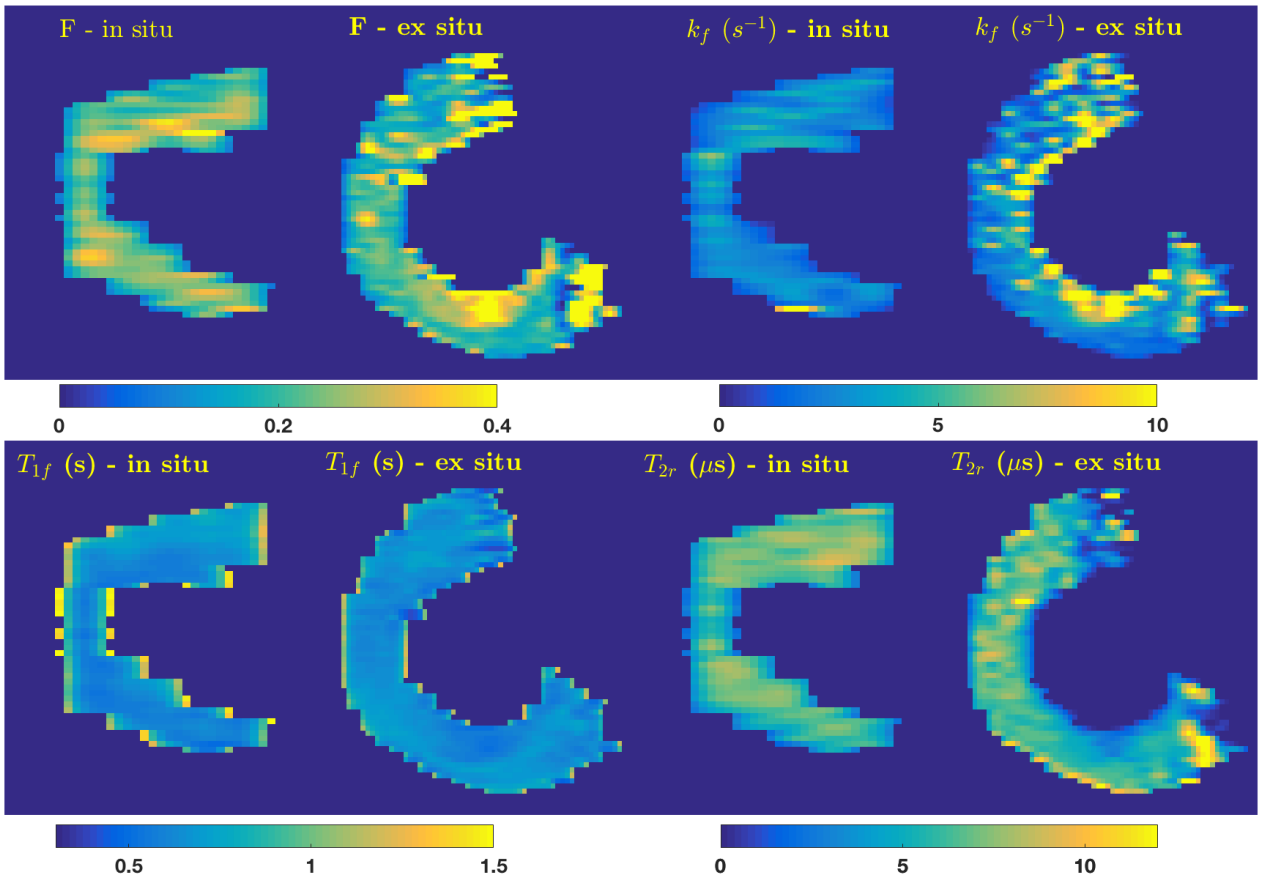

Figure 4.1 – Representative maps of QMT parameters in one axial QMT slice of lateral meniscus reconstructed and interpolated from the slices acquired in the sagittal plane. *In situ* and *ex situ* shown side-by-side. The apparent difference in resolution is due to the different slice thickness (2 vs 3 mm) used in volumetric acquisitions.

The mean QMT parameters for the three specimens with extracted menisci are shown in figure 4.2. For

each specimen, we present the mean QMT parameters for the *in situ* medial meniscus, *ex situ* medial meniscus, *in situ* lateral and *ex situ* lateral. For completeness, we also provide the mean values of T_{1obs}, obtained through VFA measurements.

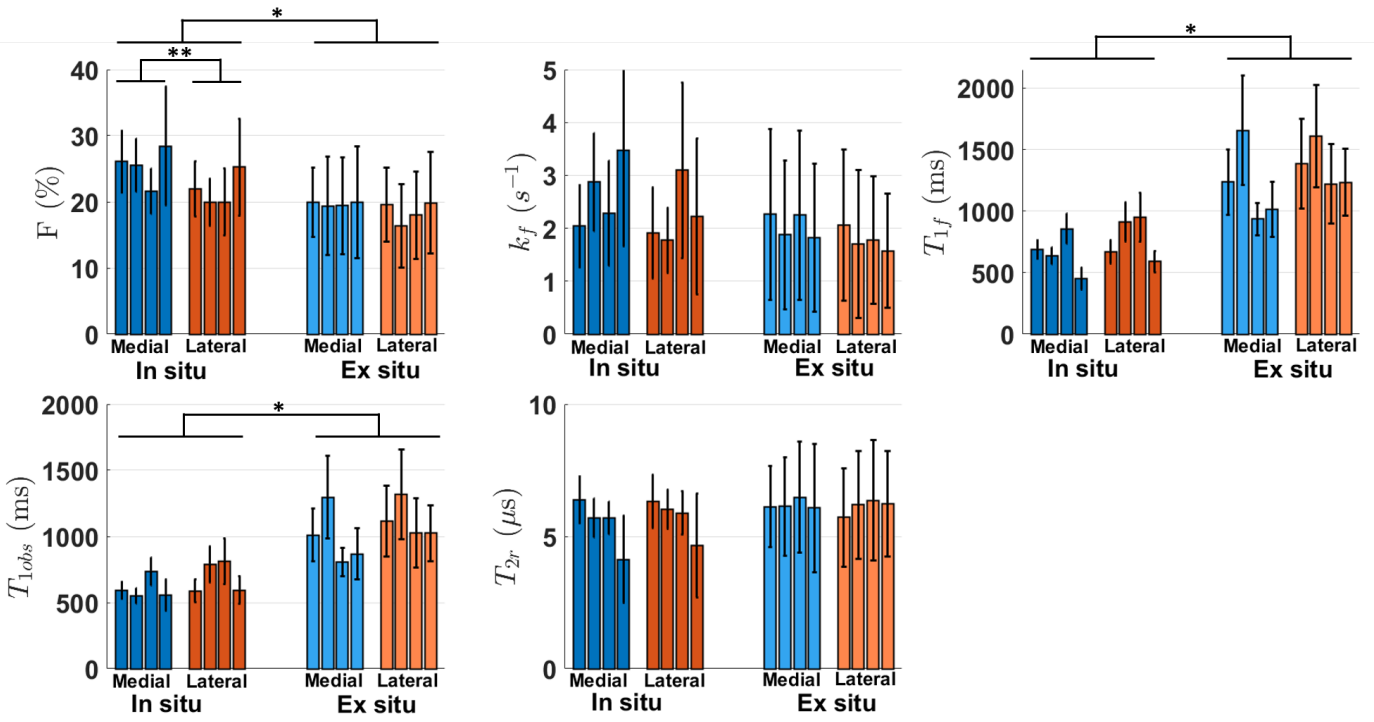

Figure 4.2 – Mean QMT and relaxation parameters values with standard deviations in the medial and lateral menisci for the *in situ* and *ex situ* specimens. * P $<$ 0.01, ** P = 0.04.

Mean F, T_{1obs} and T_{1f} varied significantly after extraction, while mean T_{2r} was relatively constant. Values of F were systematically lower (P <0.01) in the *ex situ* samples than *in situ* samples, and consistently lower in the medial menisci (P = 0.03). T_{1obs} and T_{1f} in the menisci increased in all specimens after excision (P <0.01 for both), and values of T_{1f} were systematically higher than T_{1obs}. T_{2r} showed no obvious variation after extraction or between lateral and medial samples. k_f decreased in 6 out of 8 ROIs, but the high variability of this parameter might limit the interpretation of this change.

4.3.2 QMT parameters of the post-mortem knee joint – *in situ*

Quantitative maps of F, T_{1f}, k_f and T_{2r} for a single slice of a lateral meniscus and whole cartilage are shown in figures 4.3 and 4.4. Maps of F and T_{1f} appear relatively homogeneous, while maps of T_{2r} and k_f are more heterogeneous. For cartilage, there is a similar heterogeneity when compared to meniscus maps, although structures can be identified - there is an apparent increase of F and decrease of T_{1f} with depth in tibial cartilage. Maps of k_f are noisy, while T_{2r} varies smoothly across cartilage regions.

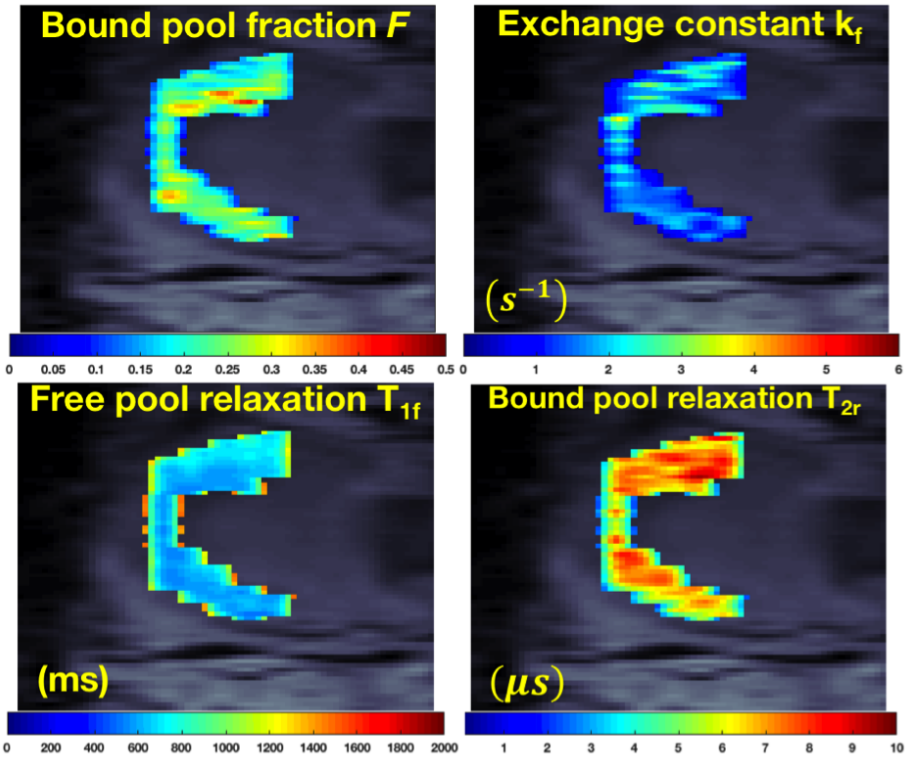

Figure 4.3 – QMT maps of an isolated lateral meniscus *in situ* post mortem overlaid on a reference volume for the MT-weighted images. Data were acquired in the sagittal orientation and reformatted in the axial direction for display.

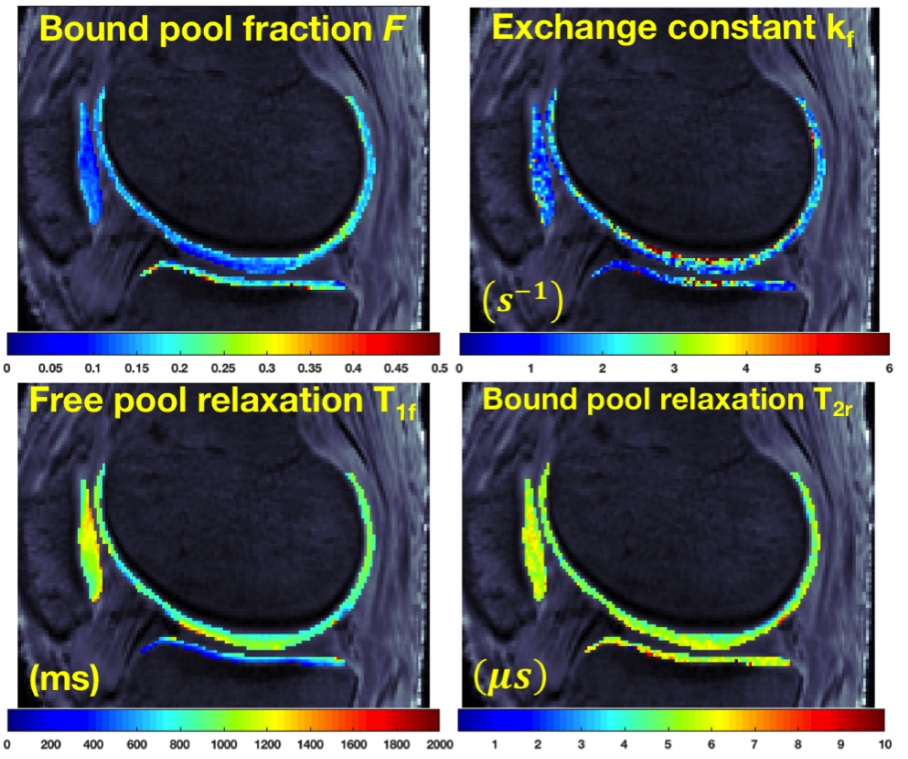

Figure 4.4 – QMT maps of isolated cartilage regions overlaid on a reference volume for the MT-weighted images. The femoral, tibial and patellar cartilage can be observed.

In addition to QMT maps, it is of interest to compare the distributions of QMT parameters in all specimens in order to evaluate the inter-specimen variability in distributions, as well as the heterogeneity of parameters in joint tissues. Figure 4.5 shows the distribution of QMT parameters in both menisci for each specimen. Similar distributions were obtained between specimens for F, k_f and T_{2r}, although specimen S04 has a broader distribution of T_{2r} values. The distributions of the longitudinal relaxation time of the free pool, T_{1f}, showed more variability specimen-wise. Distributions of QMT parameters in the whole cartilage are shown in figure 4.6. Overall, the distributions are similar for specimens S01, S02 and S03 for all QMT parameters. The distribution of T_{1f} between specimens is more homogeneous in cartilage than in meniscus. The distributions of T_{1f} and T_{2r} are different for S04 in cartilage. It is unclear if the difference is caused by biological variability or another external cause, although there was no noteworthy difference in the medical information available between specimens.

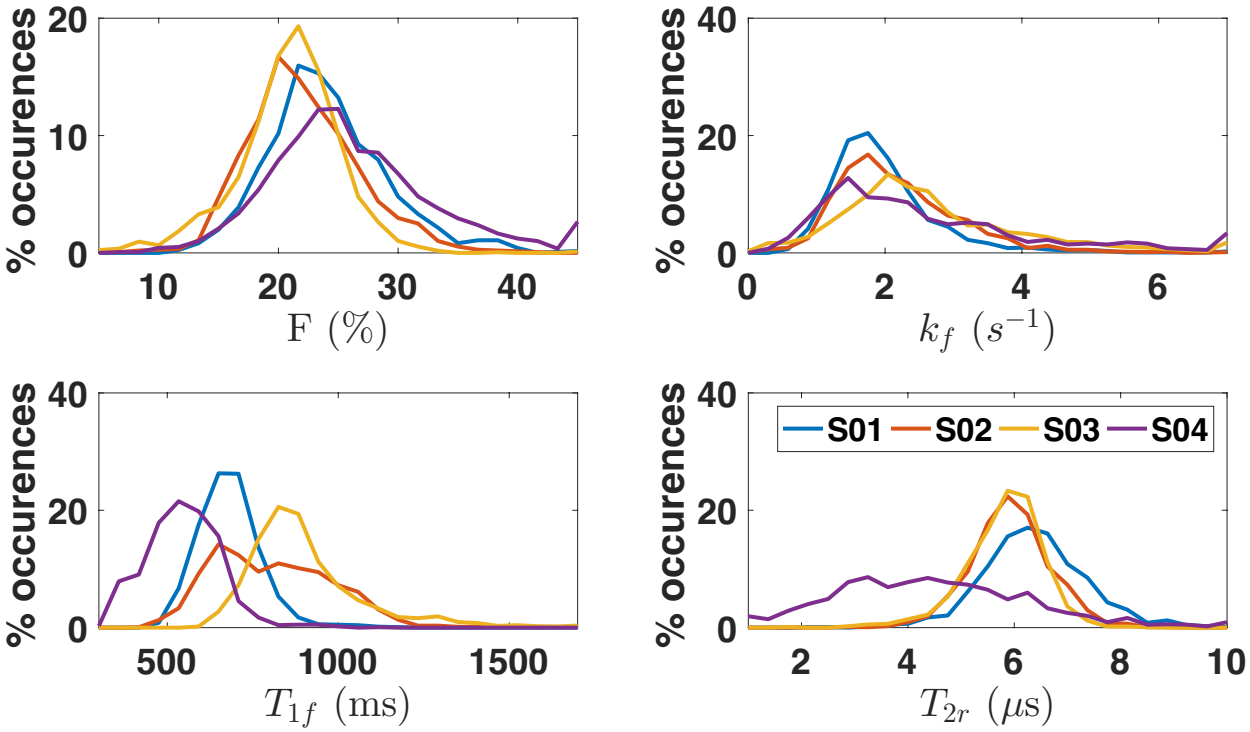

Figure 4.5 – Distribution of QMT parameters for all specimens in both menisci.

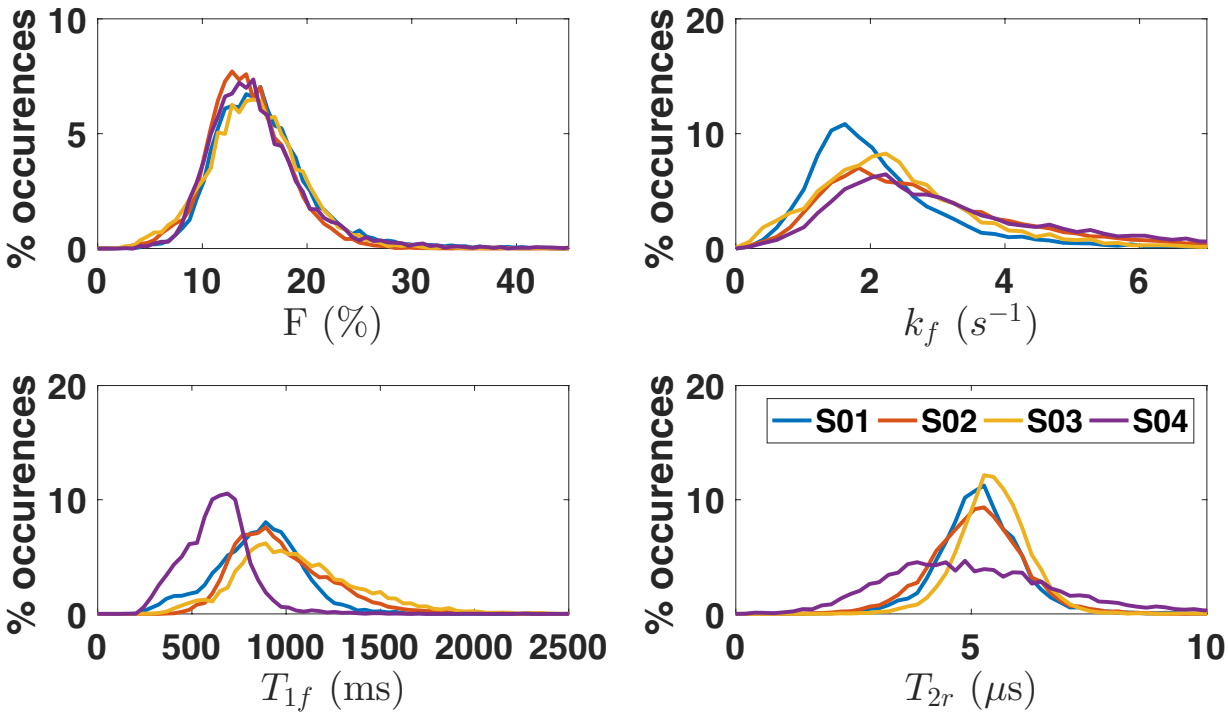

Figure 4.6 – Distribution of mean QMT parameters for all specimens in the whole cartilage.

Mean F, T_{1f}, k_f, T_{1obs} and T_{2r} in different regions of the knee joint at 3T are reported in table 4.1, and the specimen-wise values are reported in figure 4.7.

Table 4.1 – Magnetization transfer parameters at 3 T in various tissues of the knee joint *in situ* postmortem. The reported uncertainty is the standard deviation of the mean parameters across all samples. For both menisci, lateral and medial meniscus voxels were averaged together. Patellar, femoral and tibial cartilage voxels were averaged to produce whole cartilage values.

Tissue (N=4)	$\boldsymbol{F}(\%)$	$\boldsymbol{k_f}(\boldsymbol{s^{-1}})$	$\boldsymbol{T_{1obs}}(\boldsymbol{ms})$	$\boldsymbol{T_{1f}}(\boldsymbol{ms})$	$\boldsymbol{T_{2r}}(\boldsymbol{\mu s})$
Lateral meniscus	21.86 (2.51)	2.26 (0.59)	698.6 (120.0)	783.1 (177.3)	5.74 (0.74)
Medial meniscus	26.76 (2.82)	2.67 (0.64)	611.6 (85.9)	661.0 (166.6)	5.50 (0.95)
Both menisci	23.36 (2.41)	2.38 (0.35)	663.9 (90.9)	736.2 (156.0)	5.65 (0.81)
Tibial cartilage	16.24 (1.23)	2.87 (0.58)	763.0 (128.9)	815.8 (189.5)	4.97 (0.42)
Femoral cartilage	15.47 (0.68)	3.11 (0.78)	805.1 (128.9)	881.5 (191.3)	5.37 (0.36)
Patellar cartilage	12.99 (0.68)	2.82 (0.64)	904.5 (143.9)	977.4 (225.5)	5.56 (0.20)
Whole cartilage	15.19 (0.61)	3.00 (0.69)	813.3 (117.2)	882.8 (186.2)	5.30 (0.17)

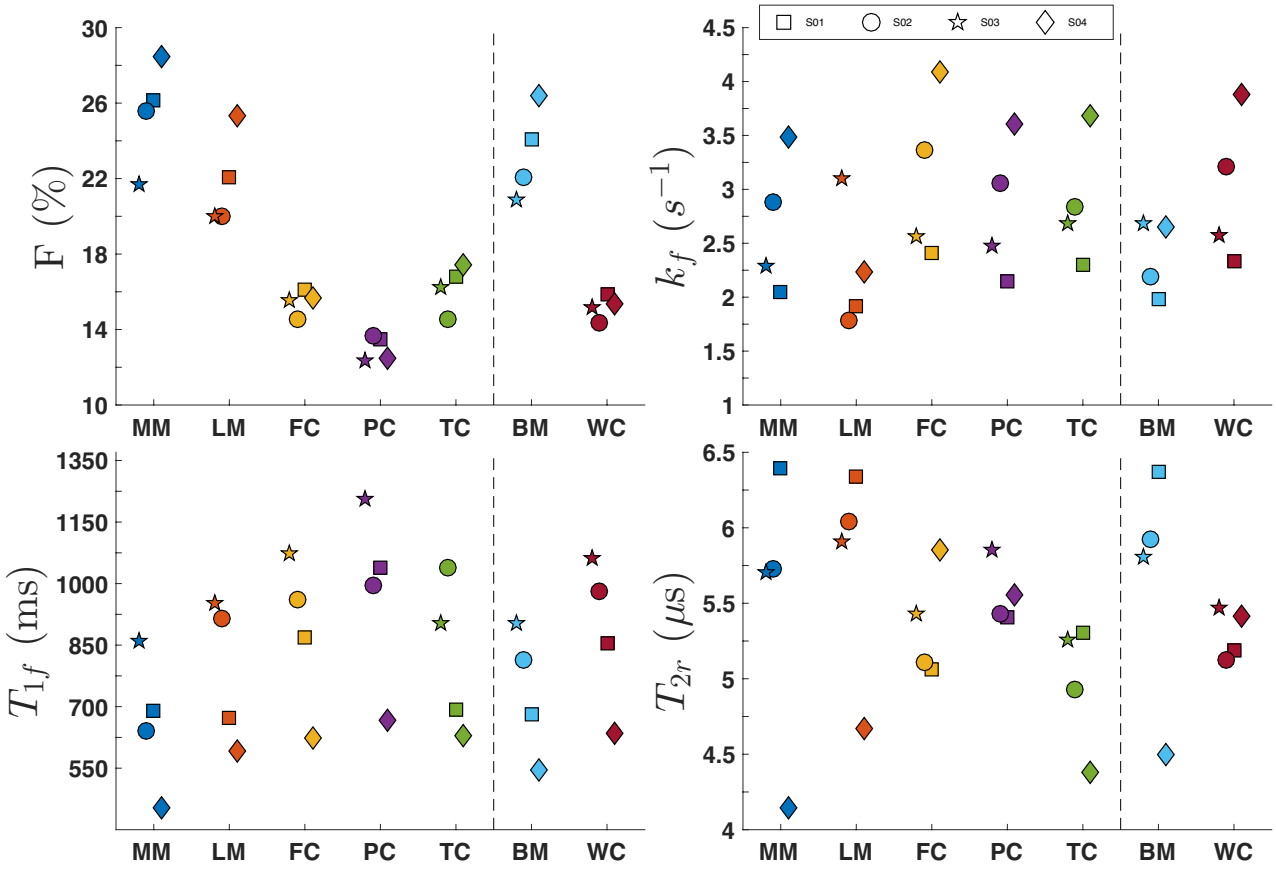

Figure 4.7 – Distribution of mean MT parameters at 3 T in various knee joint tissues for the four whole knee specimens, which are identified with different markers. LM, MM = lateral and medial menisci. FC, PC, TC : femoral, patellar, tibial. Both menisci (BM) and whole cartilage (WC) are also shown.

There were statistically significant differences in F and T_{1f} between cartilage and menisci (P = 0.04), while T_{2r} and k_f did not show significant variation. As shown in figure 4.7, F is systematically higher in the meniscus, consistent with a systematically lower T_{1f}. T_{2r} was also higher in meniscus for 3 out of 4 specimens, while the exchange constant k_f was lower in the meniscus for 3 specimens.

In the menisci, we noted a statistically significant difference in the restricted pool size ratio F (P = 0.04) between lateral (21.84%) and medial (25.48%) menisci. No other obvious trend was observed between both menisci.

In cartilage, there was a statistically significant difference (P = 0.018) in F between the patellar, femoral and tibial cartilage. F was systematically lowest in patellar cartilage and highest in tibial cartilage. There were no other obvious trends observed between different ROIs for the other QMT parameters.

The observed apparent increase in F is plotted in figure 4.8, following the methodology described in section 4.2.2.

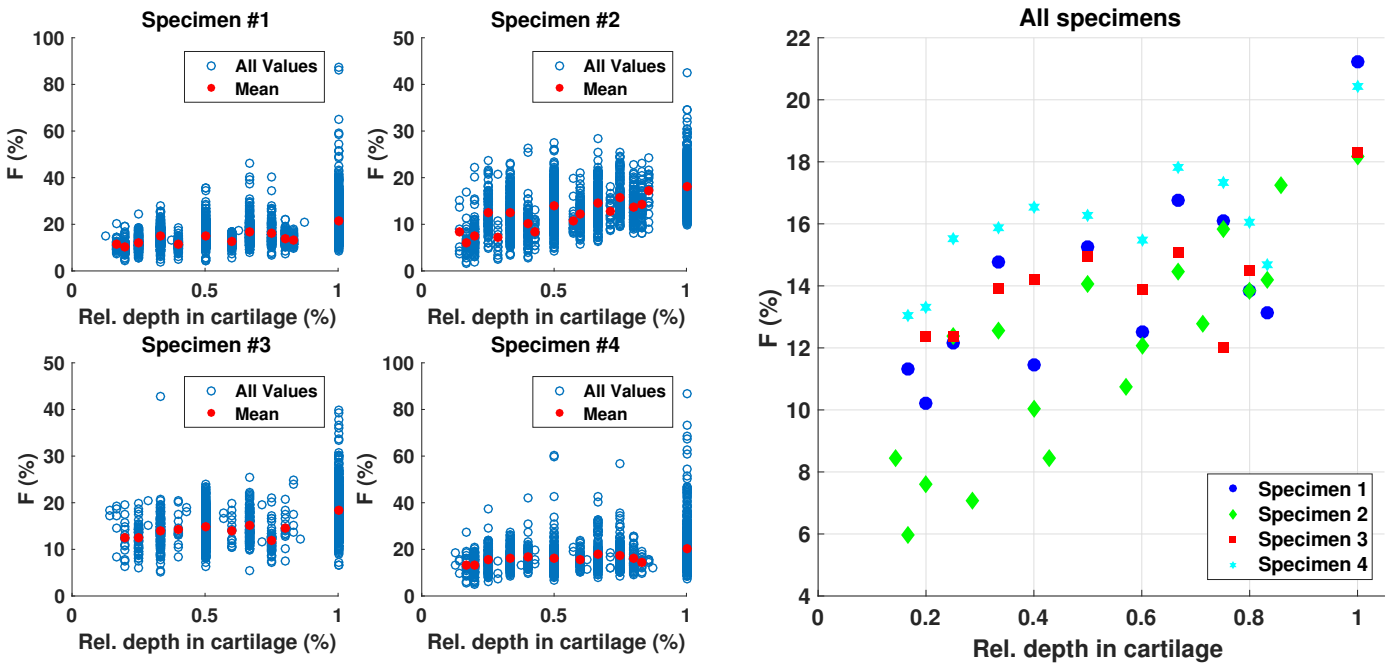

Figure 4.8 – Depth-dependence of F in the tibial cartilage. Left : each subplot shows specimen-wise the distribution of F with relative depth (blue circles) and the mean is identified in filled red circles. Right : the mean F at each relative depth for all specimens are plotted together.

4.4 Discussion

Our study has shown that after excision of the menisci and immersion in perflubron, some parameters showed a statistically significant variation, especially a systematic decrease of F and a systematic increase of T_{1f} and T_{1obs}. In cartilage, we reported values of F and T_{2r} consistent with the literature, while k_f was significantly lower. This could be due in part to the different models of MT and sampling schemes used.

4.4.1 Comparison of *in situ* and *ex situ* menisci

The value of F was systematically lower for *ex situ* meniscus, while T_{1f} and T_{1obs} were systematically higher. This variation in QMT parameters might be explained by the diffusion of perflubron into the extracted samples. Further studies of perflubron dynamics are required to understand the observed differences. Assuming diffusion of perflubron in the tissues, the bound pool fraction F might be reduced due to an increased amount of fluid in the tissue. This might lead to higher relaxation times T_{1f} and T_{1obs}, which are dependent on the amount of fluid in the tissue.

For k_f, although it decreased in 6 out of 8 ROIs, the few samples analyzed combined with the high variability of k_f limits the interpretation on this parameter. T_{2r} also showed no significant change after

the extraction. In the literature, T_{2r} has been interpreted as a measure of the rigidity of the semisolid structure [24]. This would suggest that extraction and conservation have limited effects on the integrity of the structure.

4.4.2 QMT parameters of the post-mortem knee joint - *in situ*

We have reported QMT parameters in the *in situ* meniscus and cartilage. Generally, our estimates of F, T_{1f} and T_{2r} are robust, but confidence in our estimates of k_f is lower based on the high variability in this parameter. This is possibly due to the sampling scheme used in this study, especially the low MT powers used as well as the differences in TR and MT pulse duration. In comparison to the literature, Stikov *et al.* [7] have used a single MT flip angle of 670°, while Sritanyaratana *et al.* [6] have used two MT flip angles of 1550° and 890°. The maximum flip angle in this study was 450°, which limits the sensitivity to the MT effect. In addition, Sritanyaratana *et al.* [6] have used a longer MT preparation pulse (18 ms Fermi pulse) : this leads to a higher saturation of the bound pool, which increases the MT effect.

The mean T_{1obs} value observed in menisci (663.9 ± 90.9 ms), is lower than the literature value of 720 ± 119 ms for both menisci [115], although both studies show similar high variability. The mean T_1 relaxation time of the free pool of the menisci is higher (736.2 ms), and closer to the observed T_1 in the literature [115].

In the menisci, we noted a systematically lower bound pool fraction F in the lateral meniscus than the medial meniscus. This result would suggest that there is a small, but noticeably greater fraction of macromolecular content in the medial meniscus.

The values of F obtained in this work might be slightly underestimated due to the biased fixed T_{1f}/T_{2f} ratio. Indeed, for brain tissue, it was noted that T_{2obs} was consistently higher than T_{2f} [17]. As such, the estimated ratio is possibly underestimated. In menisci datasets, increasing by 10 the fixed ratio and re-evaluating mean QMT parameters leads to a relative increase in F of 4%. In terms of composition, it is reported that the menisci, by wet weight, are composed of approximately 72% of water and 28% of organic matter, which itself is composed mostly of collagen and PGs [116]. This could suggest a maximum bound pool fraction of 28% in the menisci. We observed a mean value for both menisci of 23.36%. Assuming that this value may be slightly underestimated, the value of F obtained seems to accurately infer the macromolecular content in menisci. The restricted pool ratio is much higher in menisci than in most human tissues, which is typically between 5 and 15% [117] and can be associated with the high collagen content related to the role of the menisci. The relaxation time of the bound pool, T_{2r}, was

noted to be lower than most human tissues, which have T_{2r} typically larger than 7.7 μs [117], while the exchange constant k_f was comparable, but lower than most brain tissues, which can range between 1.7 and 5 s^{-1} [24].

In cartilage, it was noted that the average F obtained in patellar cartilage (15.19 $\pm$ 0.61%) was consistent with recently published literature values by Sritanyaratana *et al.* [6] of 14.23 $\pm$ 0.89%. T_{2r} was similar, but lower than the value obtained by Sritanyaratana *et al.* [6] (5.30 $\pm$ 0.17 against 6.49 $\pm$ 0.13 μs). Finally, the exchange constant k_f is considerably lower (3.00 $\pm$ 0.69 against 7.22 $\pm$ 0.95 s^{-1}). Our mean value of k_f is more consistent with Stikov's work in tibial cartilage [7]. Although no mean value is provided in Stikov's work, the mean k_f we obtained in tibial cartilage of 2.12 s^{-1} compares better, but still appears lower than the values between 2 and 5 s^{-1} in their scatter plots.

There are some potential sources of error and differences between studies that might lead to different mean QMT parameters in cartilage. First, the different sampling schemes combined with the different models used (Yarnykh's model used by Stikov and Sritanyaratana [6, 7] against Sled & Pike's model used in this work) can lead to different mean values for underlying similar tissues. Indeed, for the same data, Yarnykh's model consistently provides a higher exchange constant k_f with respect to Sled & Pike's model [32]. This is observed in the current work. Second, in this work, simultaneous fitting of VFA and MT data was done to correct for the biexponential longitudinal relaxation due to MT, while this was not performed for the other studies. We observed, in our datasets, consistently with a previous study [35], that the joint fitting procedure leads to lower F and k_f, higher T_{1f} and leaves T_{2r} unaffected. Third, the ratio T_{1f}/T_{2f} in this study was fixed at 25 as opposed to 18 [6] and 20 [7] in the other studies on cartilage. This can lead to variations in QMT parameters. The amplitude of the introduced bias with the fixed value of T_{2f} is however hard to quantify, as it is sampling-scheme and model dependent. Finally, this and Stikov's work were performed with cadaveric cartilage specimens, while Sritanyaratana's work was performed in vivo with healthy volunteers. The differences that might arise in QMT parameters is unclear and might be related to the large variability in k_f observed between our and Stikov's work against Sritanyaratana's study.

The observed T_1 relaxation time in whole cartilage (813.3 ms) is not in good agreement with observed T_1 at 3 T for cartilage in a study by Stanisz *et al.* [117] (mean value of 1168 ms). This is due to the fact that our observation of T_1 is biased in VFA experiments due to MT, while Stanisz used an inversion recovery (IR) technique to obtain T_1 values, where the bias due to MT is not present [4]. Indeed, their value of 1168 ms is in slightly closer agreement with the mean T_{1f} in cartilage of 882.8 ms that we observed. The difference can be partially explained by the small sample size in this study and the large

variability of T_1 values obtained.

In our specimens, we noted one major difference in QMT parameters between different ROIs (patellar, tibial and femoral cartilage). F was systematically the lowest in patellar cartilage and the highest in tibial cartilage. This is unexpected, as there is no apparent difference in the composition of the 3 cartilage regions [118]. The average SNR in patellar cartilage is typically 30 to 40% higher than that of the tibial cartilage, and 10 to 20% higher than femoral cartilage in all specimens studied. This might be caused by differences in tissue thickness and the positioning relative to the receive coil. For Sled & Pike's model, it can be shown through Monte Carlo simulations that a lower SNR leads to an overestimation of F. The observation that cartilage ROIs with lower SNR have a significantly higher F is consistent with the response of the model as a function of the SNR. The differences in F could be in part explained by SNR variations.

It was observed in figure 4.8 that F increased with depth in tibial cartilage. Accordingly, T_{1f} followed the opposite trend. The same trend was observed in Stikov *et al.*'s work [7]. In articular cartilage, there are four distinct zones that appear with depth : the superficial, middle, deep and calcified zone, which are characterized by different ultrastructure and composition. There is the lowest water concentration in deeper zones [118]. The relative water concentration decreases from about 80% at the superficial zone to 65% in the deep zone [118]. These observations are consistent with the increase in the bound pool fraction, which is an indirect measurement of macromolecular content, with depth in cartilage.

There were significant differences between QMT parameters in cartilage and meniscus. Notably, F was higher in the meniscus, while T_{1f} was reduced. Articular cartilage is composed of 65 to 85% water, 10-20% type II collagen and 5-10% proteoglycan. The meniscus is composed of 60-70% water, 15-25% type I collagen and 1-2% proteoglycans [118]. The differences in F can be explained by the differences in relative water and macromolecular (collagen and proteoglycan) content of each tissue. Although not significant, a lower k_f and higher T_{2r} in meniscus was noted in 3 of the 4 specimens. Significant differences in T_{2r} could be associated with a different rigidity of each tissue [24].

Our study has several limitations. First, the small number of samples scanned limited the comparison between *in situ* and *ex situ* specimens. While a significant variation of F and T_1 relaxation times was observed after excision, we can only conclude that for k_f and T_{2r}, no significant trend was observed with 4 specimens. Second, this study could not identify with certainty a mechanism that would lead to variations of F and T_{1f} while leaving k_f and T_{2r} unaffected. More studies on perflubron dynamics are needed to understand the observed variations in QMT parameters. Another limitation was the non-optimal sampling scheme used that did not allow stable fits of T_{2f}. The value of T_{2f} was fixed as a ratio

of T_{1f}, and the ratio was estimated for meniscus based on T_2 values from the literature, as there are no published values of T_{2f} in meniscus. This means that the T_{1f}/T_{2f} ratio used can be biased, and the amplitude of the bias that propagates to other QMT parameters is currently unknown. Future QMT studies should use an optimized sampling scheme that can provide robust estimates of T_{2f}. Optimizing the Z-spectrum via optimal design [85, 97] could lead to more robust fits of all QMT parameters and is mandatory for future work, especially in meniscus where no value of T_{2f} has been reported.

4.5 Conclusion

This work was a first step to understand the impact of extraction and immersion of joint tissues, provides QMT values of articular cartilage and report for the first time QMT parameters of meniscus.

Our study has shown that when comparing *in situ* and *ex situ* samples of menisci, a significant increase in F and decrease in T_{1f} can be expected and might be attributed to the diffusion of perflubron into the *ex situ* samples. Other QMT parameters were not significantly influenced by the extraction and immersion procedure. It is clear that further studies are needed to understand the interaction of the extracted tissues with perflubron.

Our QMT technique provided QMT parameters in cartilage mostly consistent with the literature. The estimation of F in meniscus was also consistent with the composition by wet weight of the meniscus. It was also observed that in cartilage, F increased with depth in patellar cartilage. These observations suggest that QMT imaging can evaluate the macromolecular content of cartilage tissue and meniscus and identify changes in the macromolecular matrix. Overall, QMT may be used to identify early cartilage and meniscal degeneration and is an interesting candidate as a potential biomarker for OA.

4.6 Acknowledgements

The authors would like to acknowledge the contributions of Marcus Alley for the SPGR pulse sequence used in this work, Braggi Sveinson for the method to map the B1 field, John Sled and Bruce Pike for supplying the original code from which the analysis software was derived, Marianne Black for contouring of anatomical regions, as well as Véronique Fortier, Zaki Ahmed and Stella Xing for useful discussion. This work was funded by le Fonds de recherche sur la nature et les technologies (FQRNT), the Natural Sciences and Engineering Research Council (NSERC), the Montreal General Hospital (MGH) Foundation, the Research Institute of the McGill University Health Center (RI-MUHC), GE Healthcare, NIH Grants 5K24AR062068-02, R01 AR063643-01 and R01 Eb002524-01. MS acknowledges fellowship support from NSERC, FQRNT and partial support by the CREATE Medical Physics Research Training Network grant of the NSERC (Grant number : 432290).

5 Optimization of the sampling scheme

5.1 Introduction

Optimization of the sampling scheme was often mentioned in previous chapters. In chapter 3, it was shown through Monte Carlo simulations that different combinations of sequence parameters (such as the MT pulse frequency offset Δ, flip angle α_{MT}, pulse duration τ, and the total number of points acquired in the Z-spectrum) could lead to various quality of fits for the QMT parameters. This is due to the nonlinear nature of the model.

In chapter 3, it was broadly discussed that MT sequences which seemed to maximize the MT effect (using higher power pulses, notably) allowed a more accurate and precise estimation of QMT parameters for a clinically achievable SNR. It is unclear, however, which specific values of Δ and α_{MT} must be chosen in order to maximize the quality of fits. An optimal acquisition scheme must sample the Z-spectrum where the model is the most sensitive.

The objective of this chapter is to describe a method to optimize the sampling scheme in MT experiments, and show preliminary results that demonstrate the potential gain in accuracy and precision achievable by modifying the sampling scheme.

The approach used here is the one of optimum experimental design. When designing experiments to estimate parameters from a model (such as choosing a Z-spectrum sampling scheme in MRI to which we fit a model of QMT), the optimal design leads to an estimation of parameters with minimal bias and variance [119]. Here, we provide an overview of previous work done in optimum design applied to QMT, detail the methods and show a proof of concept through Monte Carlo simulations that optimizing the sampling scheme can lead to a more robust evaluation of QMT parameters, specifically for meniscus. We also summarize the general improvements that must be made for future QMT studies in cartilage.

5.2 Methods

In optimal design, the sequence parameters must be optimized with respect to an optimality criterion. In the case of fitting experimental MRI data to a model, the sum of the variances of the parameters in the model can be used as the criterion to obtain parameters with minimal variance.

For a simple and linear model, an analytical expression of the variance of parameters can easily be obtained from the model signal equation and the problem is straightforward. However, in the case of complex nonlinear models such as the binary spin bath model of MT, an analytical expression for the variance of the parameters cannot be obtained from the equation that describes the model of signal.

In this situation, one can rely on the Cramér-Rao lower bound (CRLB), which expresses a lower bound on the variance of parameters of a model. Specifically, the CRLB states that the variance of estimators of parameters is equal or larger to the inverse of the Fisher information. For a model S with Q parameters $p_1, ...p_Q$ fitted to N measurements points $\boldsymbol{x}_1, ...\boldsymbol{x}_N$, the Fisher information matrix $\boldsymbol{J_{ij}}$ can be expressed as [85] :

$$\boldsymbol{J_{ij}} = \sum_{n=1}^{N} \frac{\partial S(p_1, ...p_Q; \boldsymbol{x_n})}{\partial p_i} \frac{\partial S(p_1, ...p_Q; \boldsymbol{x_n})}{\partial p_j} \tag{5.1}$$

The ensemble of all measurements $\{\boldsymbol{x_n}\}$ represents the sampling scheme used and are the variables optimized in optimum design. For the specific case of QMT, the parameters p_i are F, k_f, T_{1f}, T_{2r}, T_{2f} and each $\boldsymbol{x_n}$ specifies a given combination of sequence parameters : α_{MT}, Δ, τ, and possibly other MRI pulse sequence parameters. T_{1r} is not considered in the p_i parameters, as it is not fitted in the model but fixed.

In simple terms, the CRLB states that to minimize the variance in parameters, one must extract the maximum information possible from the model. Formally, the CRLB can be expressed as $\boldsymbol{\Sigma} \geq \boldsymbol{J^{-1}}$, where $\boldsymbol{\Sigma}$ is the covariance matrix of the parameters. As we are interested in the variance of the parameters, which are the diagonal elements of the covariance matrix, $\boldsymbol{\Sigma_{ii}}$, we use the inequality $\boldsymbol{\Sigma_{ii}} \geq [\boldsymbol{J^{-1}}]_{ii}$.

In this work, we use the methodology developed by Cercignani and Alexander [85]. The optimization problem is defined as follows. The optimum design $\{\boldsymbol{x_n}\}_{opt}$ is a set of N measurements that minimizes the objective function defined by the sum of the variance of the parameters in the model :

$$V = \sum_{i=1}^{Q} \frac{1}{p_i^2} \boldsymbol{\Sigma_{ii}} \tag{5.2}$$

The variance of each parameter is normalized by the value of the parameter to ensure that the amplitude of each variance is comparable. This is especially important in QMT where parameters differ of many orders of magnitude (for example, T_{2r} is in μs, while T_{1f} is in seconds). Because the variances $\boldsymbol{\Sigma_{ii}}$ are unknown, $\boldsymbol{\Sigma_{ii}}$ is replaced by the CRLB $[\boldsymbol{J^{-1}}]_{ii}$, which gives the final objective function to minimize :

$$V = \sum_{i=1}^{Q} \frac{1}{p_i^2} [\boldsymbol{J^{-1}}]_{ii} \tag{5.3}$$

The function V depends on specifically chosen QMT parameters p_i and the measurement points $\{\boldsymbol{x_n}\}$. Because of the nonlinearity of the model, the derivatives involved in the calculation of the Fisher information matrix depend on the choice of the QMT parameters. As such, the problem of optimum design here is more complex in the sense that the optimum scheme $\{\boldsymbol{x_n}\}_{opt}$ depends on the QMT parameters chosen in the optimization. Therefore, optimizing the sequence for different tissues (brain or cartilage, for example) might lead to different optimum designs. In this work, we optimize with respect to mean QMT parameters of menisci, as detailed in chapter 3. The sequence is then optimal for meniscal tissues. The results could be reproduced using QMT parameters of articular cartilage.

The optimization of V involves searching for a global minimum in a highly dimensional search space. For example, assuming 10 Z-spectrum points where Δ and α_{MT} are optimized, while other sequence parameters (τ,TR) are fixed, the search space will have 20 dimensions (10 measurement points, each with an optimized α_{MT} and Δ). In this case, the technique used to find the global minimum of V, referred to as the optimization algorithm, should perform well in large search spaces. Stochastic algorithms such as simulated annealing (SA) are then typically used instead of gradient descent methods.

There are two main studies that describe optimum experimental design approaches to QMT. The procedure described up to now was first proposed by Cercignani and Alexander [85], for QMT in brain tissue. For the optimization algorithm, they proposed a hybrid method that combines simulated annealing, often used for global optimization problems, with the downhill simplex method. While robust, simulated annealing (SA) is a slow optimization technique, each optimization typically taking a few days. The reader is referred to [85] for more details on the optimization procedure. As they used a different model of QMT (the approach of Ramani *et al.* [29]), a different parameterization and optimized for brain QMT parameters, their optimal scheme cannot be used in the current work. The optimized schemes they proposed provided a substantial improvement to the evaluation of QMT parameters in brain. Another optimum design approach was proposed by Levesque *et al.* [97] which used iterative reduction of a discrete sampling of the Z-spectrum to reach an optimum design. As opposed to Cercignani and Alexander, there was no constraint on the number of Z-spectrum points. Their results also suggested that using two

TRs could yield more precise estimates of MT parameters and that no clear benefit would be obtained with more than 15 distinct points in the Z-spectrum.

In this work, we combined elements of both studies and use a fixed number of 10 Z-spectrum points and optimized for 1 and 2 TRs separately. We used the objective function proposed by Cercignani and Alexander, but with a different optimization algorithm, stochastic region contraction (SRC). SRC was proposed in 1991 [120] as a global optimization technique. While stochastic in nature like simulated annealing, it is much more efficient, and converges to a solution much faster. SRC can also constrain the search space with simple lower/upper bounds on each variable. The reader is referred to [120] for the mathematical formulation of SRC. Here, we provide a conceptual description of SRC.

Consider the optimization of the function V in a M-dimensional search space. There are M parameters to be optimized. For each parameter, lower and upper bounds LB_i and UB_i are defined. These boundaries define the initial search space.

1. First, generate randomly $N_{samples}$ combinations of the M parameters, each defined within the prescribed upper and lower bounds.
2. Then, evaluate the function V for each of the $N_{samples}$ combinations of the M parameters. This results in $N_{samples}$ values of the function V.
3. These $N_{samples}$ evaluations of V are sorted in increasing order, and the N_t smallest ones are kept, along with the N_t combinations of the M parameters that provided these smallest values of V.
4. For each of the M optimization parameter, new updated boundaries LB_i and UB_i are generated based on the minimum and maximum value of this parameter within the N_t values conserved.

Then, the entire procedure is repeated, each time generating $N_{samples}$ combination of the parameters within the new boundaries. The search space is thus reduced at each iteration. When the difference between the upper and lower bound of all optimization parameters is less than ε %, convergence is reached. The name *stochastic region contraction* comes from the fact that the search space is randomly sampled at each iteration, hence the stochastic nature, and that the search space is increasingly constrained at each iteration, leading to the contraction of the *region* where a solution is searched for.

Based on our own experience and parameters suggested in another study [121], we used $N_{samples} = 4000$, $N_t = 50$ and $\varepsilon = 0.5$. When searching in a 22-dimension space (10 Δ, 10 α_{MT} and 2 TRs), we observed that approximately 150 iterations were required to reach convergence. The computation time was approximately 5 hours (performed in MATLAB 2016a on a 3.5 GHz Core i7 processor with 32 Gb of RAM).

Although T_{2f} was fixed in this work, the optimization was made with respect to QMT parameters F, k_f, T_{1f}, T_{2f} and T_{2r}, as future studies should evaluate T_{2f} in cartilage and meniscus because no current values are available. To evaluate the Fisher information matrix, we used the same QMT parameters as the ones in chapter 3 for menisci simulations. The MT pulse duration was fixed to 8 ms, a Fermi pulse shape was used and the flip angle of the excitation pulse was 10°. For initial boundaries, α_{MT} was bounded between [150°, 1550°] and Δ between [1.5, 50] kHz. TR was bounded between [20,70] ms.

The maximum MT pulse angle was limited to 1550° following the maximum angle found in the literature for QMT in cartilage [6], and the minimum was set to 150°. Practically, no optimal MT angle was found under 200°. The lower bound for Δ was set to 1.5 kHz following our own observations that Sled and Pike's model of MT inaccurately represents the solution to the Bloch-McConnell equations under 1.5 kHz. The upper bound was initially set at 100 kHz where the MT effect becomes negligible, but then refined to 50 kHz following the observation that no optimal offset was found over 45 kHz. For TR, the boundaries were initially first fixed to 8 and 100 ms. No optimal TR was found outside of the range [25,65] and the boundaries were then refined to [20, 70] ms.

5.3 Results and discussion

As the SRC algorithm is stochastic in nature, running the algorithm multiple times can give different solutions. In figure 5.1, we present the final value of the objective function V at the solution for 28 distinct evaluations of the algorithm using the final boundaries for sequence parameters defined in the previous paragraph. Each of the 28 distinct evaluations is referred to as a "design". Each design is a combination of 10 Z-spectrum points at possibly different Δ, α_{MT} and TR. A sampling scheme is a synonym for design, but we use design to identify optimal sampling schemes obtained with the methodology presented here.

Each value of V corresponds to the minimum at which the algorithm converged. 13 designs were produced while optimizing two TRs (in blue, on the left part of figure 5.1) and 15 were produced optimizing a single TR (in red, on the right). Because the algorithm is stochastic and the search space has a large number of dimensions, local minima are expected. For example, designs #3 and #4 provided a value of V around 4×10^5, close to half the value of 10.5×10^5 of design #10. Between the two categories of schemes explored (one TR and two TRs), similar values of V were obtained, although a slightly lower minimum was reached for the single TR case (SRC design #21, at 3.5×10^5). In some cases (SRC designs 1 and 2, 3 and 4, as well as 5 and 6), the algorithm converged to the same local minimum.

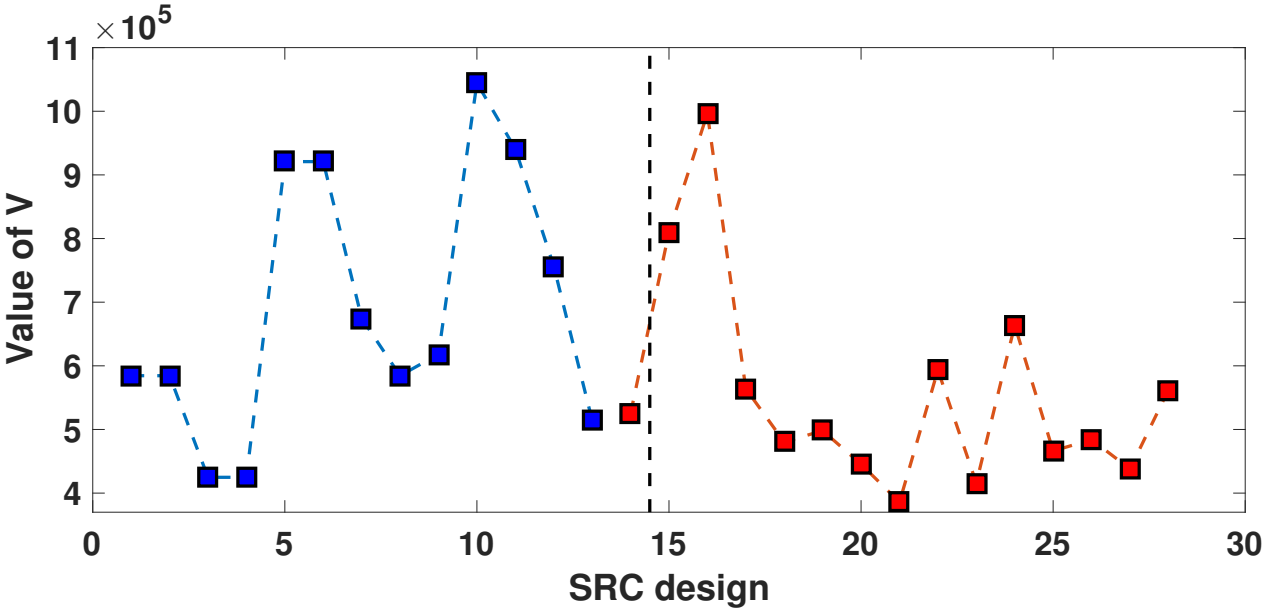

Figure 5.1 – Value of the objective function V for different optimal designs.

Based on figure 5.1, one may wonder if a noticeable difference in precision and accuracy of QMT parameter would arise when using different optimized sampling schemes. We decided to evaluate how three optimal schemes obtained from SRC designs (#3, #10 and #21) perform in the presence of noise (SNR=100). Designs #3 and #21 were chosen as they provided the minimum value of V of all designs respectively for two TR and single TR experiments. Design #10 was chosen to compare directly with design #3 to see if an optimized sampling scheme with a higher value of V still provided an improvement over the quality of fits. In table 5.1, we present the optimal sampling scheme parameters for the 3 chosen design. Offsets are in kHz, angles are in degrees and TR is in ms.

Table 5.1 – Optimized sampling schemes for QMT in the meniscus.

Design #3			Design #10			Design #21		
Δ	α_{MT}	TR	Δ	α_{MT}	TR	Δ	α_{MT}	TR
11.87	808	33	35.05	746	38	29.93	435	34
8.67	522	33	24.48	1010	38	7.10	1204	34
10.08	635	33	2.13	1031	38	6.88	450	34
1.67	1263	33	22.04	1169	38	39.49	356	34
36.56	526	33	16.06	771	38	20.59	943	34
37.42	559	52	6.74	1210	45	6.60	1209	34
9.34	1206	52	28.07	761	45	22.91	1073	34
25.52	1104	52	11.54	1192	45	8.42	1255	34
7.23	1215	52	10.21	715	45	8.23	467	34
24.44	1038	52	17.13	574	45	1.53	1321	34

In addition, we show in figure 5.2 how the values of table 5.1 are distributed in a (Δ, α_{MT}) space.

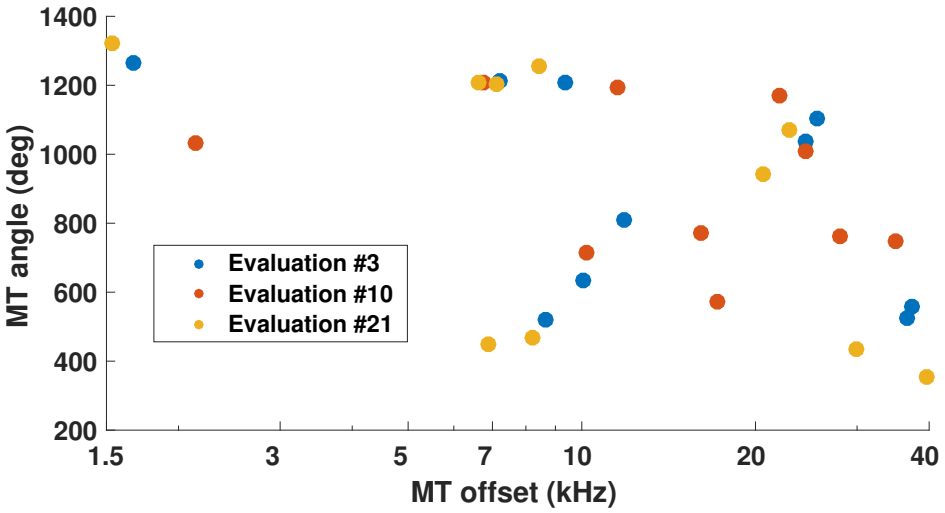

Figure 5.2 – Distribution of Z-spectrum sampling points for various SRC designs.

It can be noted that all 3 design sample a similar high power, close to resonance Z-spectrum point. There was no optimal Z-spectrum point between 3 and 7 kHz. In addition, the three optimal schemes often sample two Z-spectrum points in proximity, in agreement with the results of Cercignani and Alexander [85].

In figure 5.3, we show the distribution of QMT parameters obtained from Monte Carlo simulations with 10,000 repetitions for the 3 optimized schemes presented in table 5.1. For comparison, we also included the sampling scheme used the data acquisition for this study (see chapter 4).

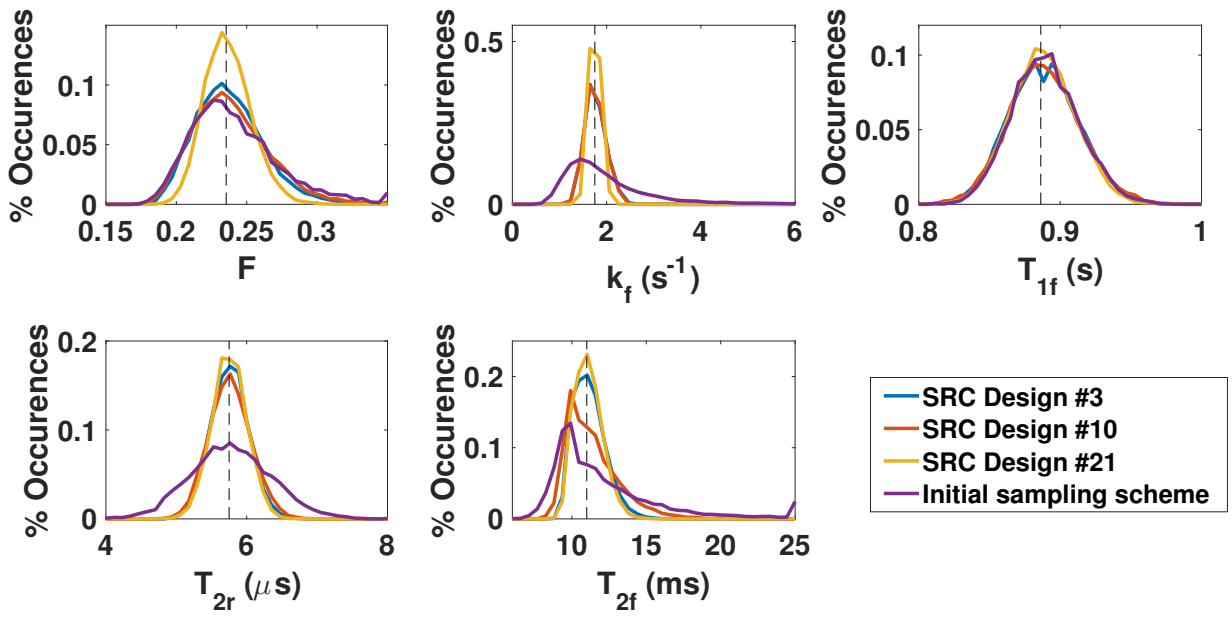

Figure 5.3 – Distribution of QMT parameter estimates for various sampling schemes obtained from Monte Carlo simulations.

Figure 5.3 shows that design #21 provides sharper QMT parameters distributions for all QMT parameters. Table 5.2 presents the coefficient of variance (COV) in percentage of each QMT parameter for the 4 sampling schemes. The COV is defined as the standard deviation of the distribution divided by the mean value.

Table 5.2 – Coefficient of variance (in percentage) of QMT parameters for various sampling schemes obtained from Monte Carlo simulations.

QMT parameter	Design #3	Design #10	Design #21	Current scheme
F	10.2	11.4	7.1	13.7
k_f	12.2	11.9	6.5	53.0
T_{1f}	2.8	2.9	2.6	2.7
T_{2f}	9.5	15.8	8.3	119.6
T_{2r}	4.6	5.1	4.3	9.9

Design #21, which provided the lowest value of V in the 28 designs obtained, greatly reduces the COV when compared to the sampling scheme used in the rest of this work. The only parameter unaffected by the optimization is T_{1f}, most likely because the VFA measurement is the most important determinant of that parameter.

When compared with the sampling scheme used experimentally, design #21 reduces the variance of parameters F and T_{2r} approximately by half, and approximately by a factor of 10 for k_f and T_{2f}. With the optimized sampling schemes, the evaluation of all QMT parameters, including T_{2f}, becomes feasible with a 10-point sampling of the Z-spectrum. It should be noted that to obtain robust estimates of T_{2f}, when using off-resonance pulses above 1.5 kHz, most of the Z-spectrum points must be acquired at high powers : indeed, the most optimal design, #21, has 60% of the Z-spectrum points acquired with $\alpha_{MT} > 900^\circ$. Frequency offsets closer to zero should not be added due to the inaccuracies of the model closer to resonance, which could lead to a biased evaluation of T_{2f}.

Overall, there are minimal differences between designs #3 and #10, both of where two TRs were optimized, but where the former (#3) yielded a slightly lower value of V. Although we recommend always using the scheme that provides the minimal value of V, the gain in accuracy and precision is small when comparing two well-optimized sampling schemes. Ideally, one can repeat the SRC optimization multiple times, as it was done here, and take the scheme with the minimum V.

There is a noticeable reduction in the COV of F and k_f when comparing design #21 (which was a single TR optimization) with the other designs. The values of V were similar for designs #3 and #21, but design #21 shows a reduced COV for all QMT parameters. These results suggest that a scheme with

a single TR (as opposed to two TRs) provides a better precision in all QMT parameters, in agreement with the work of Cercignani *et al.* [85] and contrasting with the recommendation of Sled and Pike [17] and the findings of Levesque *et al.* [97]. However, it is unclear if this conclusion holds for other QMT parameters than those of meniscus and if the use of a different number of Z-spectrum points would lead to similar conclusions. We did not seek to optimize the number of Z-spectrum points in this preliminary work. Such an optimization would need to take into account the added scan time and overall SNR benefit of additional data samples by weighting the additional scan time in a negative way in the optimization procedure.

5.4 Conclusion

The results from this chapter demonstrate that the QMT sampling scheme can be optimized by approximating the variance of parameters with the Cramér-Rao lower bound and seeking a variance-optimal solution with the stochastic region contraction algorithm. Specifically, the optimized design #21 detailed in table 5.1 provided the sharpest theoretical QMT parameters distributions and the smallest coefficients of variance for a model of meniscus. With an optimized scheme, robust estimates of all QMT parameters can be obtained in Monte Carlo simulations, while robust estimates of T_{2f} and k_f had not been obtained with the scheme used experimentally in chapters 3 and 4.

This chapter offers a limited contribution to the optimization of MRI acquisitions for QMT. The optimization could have been done with respect to a subset of QMT parameters instead of F, k_f, T_{1f}, T_{2f} and T_{2r}. Optimization could also be performed by preferentially weighting certain parameters more than others. The sequence could also be optimized with respect to the MT pulse duration, pulse waveform and excitation pulse flip angle, for example. Schemes with fewer than 10 QMT points should also be considered to reduce scan time if the method ultimately becomes used in the clinic. For the SRC algorithm, the impact of choosing different values of $N_{samples}$, N_t and ε were not investigated and are left as future work.

However, the objective of presenting a methodology to optimize the sampling scheme was reached, and preliminary results show that optimization can greatly reduce the coefficient of variance of QMT parameters.

While it was concluded in chapter 4 that robust estimates of F, T_{1f} and T_{2r} could be obtained with the sampling scheme used experimentally, we have shown here that this scheme is far from optimal, and that future studies must explore optimized schemes such as the ones proposed in table 5.1. The optimized schemes can lead to robust fits of T_{2f}, which is critically important in future QMT studies of articular

cartilage for the early evaluation of OA. Using an optimized scheme that can provide robust fits of all QMT parameters would remove the additional variability in QMT parameters caused by the fixed T_{2f} and allow a more precise comparison between in situ and ex situ specimens to quantify the effect of extraction and conservation. In addition, using an optimal scheme such as the one presented in this chapter seems the best current solution to improve estimates of T_{2f}. While UTE measurements conjugated with multi-component T_2 fits can be performed in order to extract T_2 relaxation times of tissues with small T_2 values [122] (such as the menisci), as discussed in chapter 2 there remains an unexplained discrepancy between T_{2f} and direct T_2 measurements (T_{2obs}).

6 Conclusion

This thesis presented and characterized an adapted framework for quantitative magnetization transfer imaging in joint tissues as well as the QMT analysis of 4 knee joint samples. We also presented an optimization technique to maximize the quality of the data acquired in QMT.

The objectives of this thesis were to develop a feasible method for the evaluation of MT parameters in the whole knee joint, to perform measurements in situ and ex situ to evaluate how extracting and immersing tissues influence QMT parameters, and to evaluate MT parameters in cartilage and compare these with published studies.

A modified technique for QMT estimation based on Sled and Pike's approach for pulsed MT experiments. In this technique, we fix T_{2f} to a specific ratio of T_{1f} and the other QMT parameters are obtained by simultaneously fitting the VFA and MT-SPGR datasets. We have shown that a robust estimation of F, T_{1f} and T_{2r} was possible, and that measurement noise as well as the choice of the ratio T_{1f}/T_{2f} that fixed T_{2f} has a minimal impact on those parameters. It was demonstrated in simulations that fits of k_f are not as accurate and show more variability. This might be explained partially by an inability of the model to constrain k_f with the current scheme.

With this modified technique for QMT estimation, we obtained a QMT analysis of 4 knee joint samples. Our study showed that, in meniscus, there was a statistically significant decrease in the restricted pool fraction F and increase in T_{1f} and T_{1obs} after the meniscus were extracted and immersed in perflubron before scanning. This is currently attributed to the diffusion of perflubron into the ex situ samples, although further studies are required to understand the interaction of tissues with perflubron. Other QMT parameters did not significantly vary after the extraction.

The analysis of the 4 knee joint samples also provided QMT parameters in cartilage that were mostly consistent with the literature. In addition, we obtained the first estimates of F in the meniscus, which are consistent with the composition by wet weight of the meniscus. We have observed other trends in the in situ joint tissue datasets, notably an increase of F with depth in patellar cartilage, and a significantly

higher F in medial meniscus. These observations suggest that QMT imaging can evaluate the macromolecular content of cartilage tissue and meniscus and identify changes in the macromolecular matrix. Overall, QMT may be used to identify early cartilage and meniscal degeneration and is an interesting candidate as a potential biomarker for OA.

We investigated if the current issues with the QMT framework, such as the inability to constrain adequately T_{2f} and k_f, which must be solved for future QMT studies, could be resolved with an optimized sampling scheme. In chapter 5, we have shown that the sampling scheme can be optimized by using the Cramer-Rao lower bound and seeking a variance-optimal solution with a stochastic region contraction algorithm. Robust estimates of all QMT parameters could be obtained with a 10-point sampling scheme.

The use of QMT in articular cartilage, especially as a potential biomarker for the disease of osteoarthritis, seems promising. However, many improvements must be made to the QMT framework. Ideally, an optimized sampling scheme that can provide values of T_{2f} should be used. More comparisons with histological and biochemical markers are required, and the impact of perfluorochemicals used for scanning ex situ samples should be investigated further.

Appendices

A

Derivation of the signal equation in the RP model

The Bloch equations 2.18 to 2.21 can be rewritten in the matrix form

$$\frac{d\mathbf{M}(t)}{dt} = \mathbf{A}(t)\mathbf{M}(t) + \mathbf{B}\mathbf{M}_0 \tag{A.1}$$

More explicitly,

$$\begin{bmatrix} \frac{dM_{x,f}}{dt} \\ \frac{dM_{y,f}}{dt} \\ \frac{dM_{z,f}}{dt} \\ \frac{dM_{z,r}}{dt} \end{bmatrix} = \begin{bmatrix} -\frac{1}{T_{2f}} & -\Delta & -\mathrm{Im}(\omega_1) & 0 \\ \Delta & -\frac{1}{T_{2f}} & \mathrm{Re}(\omega_1) & 0 \\ \mathrm{Im}(\omega_1) & -\mathrm{Re}(\omega_1) & -k_f - \frac{1}{T_{1f}} & \frac{k_f}{F} \\ 0 & 0 & k_f & -\frac{1}{T_{1r}} - \frac{k_f}{F} - W \end{bmatrix} \begin{bmatrix} M_{x,f} \\ M_{y,f} \\ M_{z,f} \\ M_{z,r} \end{bmatrix} + \begin{bmatrix} 0 & 0 & 0 & 0 \\ 0 & 0 & 0 & 0 \\ 0 & 0 & \frac{1}{T_{1f}} & 0 \\ 0 & 0 & 0 & \frac{1}{T_{1r}} \end{bmatrix} \begin{bmatrix} M_{0,x,f} \\ M0_{0,y,f} \\ M0_{0,z,f} \\ M0_{0,z,r} \end{bmatrix} \tag{A.2}$$

In the situation of free precession of the magnetization, the MT pulse is not considered (ω_1, Δ and W are set to 0) and the transverse magnetization is neglected. Redefining $\boldsymbol{M}(t)$ as $[M_{z,f} \;\; M_{z,r}]^T$, the Bloch equations have the form

$$\frac{d\mathbf{M}(t)}{dt} = \mathbf{A}_{fp}\mathbf{M}(t) + \mathbf{B}\mathbf{M}_0 \tag{A.3}$$

With

$$\mathbf{A}_{fp} = \begin{bmatrix} R_{1f} + k_f & -k_r \\ -k_f & R_{1r} + k_r \end{bmatrix} \tag{A.4}$$

Because the coefficients in the equations A.3 are time-independent, the general solution to the set of differential equations A.3 can be obtained and is of the form

$$F_{fp}(\mathbf{M}, \tau) = \mathrm{e}^{-\mathbf{A}_{fp}\tau}\mathbf{M} + \left[\mathbf{I} - \mathrm{e}^{-\mathbf{A}_{fp}\tau}\right]\mathbf{M}_0 \tag{A.5}$$

Where $e^{-\mathbf{A}_{fp}\tau}$ denotes the matrix exponential. The magnetization $\boldsymbol{M_0}$ is by definition $[1 \;\; F]^T$, assuming that the acquired data is normalized. In the CW irradiation of the semi-solid pool, we consider the saturation of the semi-solid pool through the instantaneous saturation rate W. The solution is of the same form as the free precession case, that is :

$$F_{cw}(\mathbf{M}, \tau) = e^{-\mathbf{A}_{cw}\tau}\mathbf{M} + \left[\mathbf{I} - e^{-\mathbf{A}_{cw}\tau}\right]\mathbf{M}_{cw}^{ss} \tag{A.6}$$

With

$$\mathbf{A}_{cw} = \begin{bmatrix} R_{1f} + k_f & -k_r \\ -k_f & R_{1r} + k_r + W_e \end{bmatrix} \tag{A.7}$$

In the RP model, W_e is equal to the instantaneous saturation rate $\langle W \rangle$ for an equivalent rectangular pulse that replaces the actual pulse waveform. To calculate the duration of the equivalent pulse, one assumes a rectangular waveform and finds the pulse duration that leads to equal powers for both rectangular and actual pulses. $\boldsymbol{M_{cw}^{ss}}$ is defined as the steady state of the magnetization established after a long period of CW-irradiation of the semi-solid pool,

$$\mathbf{M}_{cw}^{ss} = \begin{bmatrix} \mathbf{M}_{0,f} \cdot \left(\dfrac{R_{1r}fk_f + R_{1r}fR_{1f} + R_{1f}k_f + W_efR_{1f}}{R_{1r}fR_{1f} + R_{1r}fk_f + R_{1f}k_f + W_efR_{1f} + W_efk_f} \right) \\ \mathbf{M}_{0,f} \cdot f \cdot \left(\dfrac{R_{1r}fk_f + R_{1r}fR_{1f} + R_{1f}k_f}{R_{1r}fR_{1f} + R_{1r}fk_f + R_{1f}k_f + W_efR_{1f} + W_efk_f} \right) \end{bmatrix} \tag{A.8}$$

For the RP model of MT-SPGR, the pulse sequence is approximated with the following steps : instant saturation of the free pool from MT and excitation pulses, CW-irradiation of the semi-solid pool for a time $\tau/2$, a period $TR - \tau$ of free precession and a final CW-irradiation period of $\tau/2$. Following the nomenclature of Sled & Pike [17], the magnetization $\boldsymbol{M}$ after one repetition of the sequence is obtained through the concatenation of these steps :

$$\mathbf{M} = F_{cw}\left(F_{fp}\left(F_{cw}\left(S_2S_1\mathbf{M}^-, \frac{\tau}{2}\right), TR - \tau\right), \frac{\tau}{2}\right) \tag{A.9}$$

Where $\boldsymbol{M^-}$ is the magnetization at the beginning of the sequence, $\boldsymbol{S_1}$ represents the instantaneous saturation by the MT pulse $[S_f \;\; 1]^T$ and $\boldsymbol{S_2}$ is the instantaneous saturation due to the excitation pulse, $[\cos(\alpha) \;\; 1]^T$. The solution is obtained by solving $\boldsymbol{M}(t) = \boldsymbol{M}(t + TR)$, that is $\boldsymbol{M^-} = \boldsymbol{M}$:

$$\mathbf{M} = F_{cw}\left(F_{fp}\left(F_{cw}\left(S_2S_1\mathbf{M}, \frac{\tau}{2}\right), TR - \tau\right), \frac{\tau}{2}\right) \tag{A.10}$$

Using equations A.5 to A.8, one can isolate $\boldsymbol{M}$ and obtain an expression for the longitudinal magnetization of the free pool :

$$\begin{bmatrix} M_{z,f} \\ M_{z,r} \end{bmatrix} = \mathbf{inv}\left(\mathbf{I} - e^{\left(-\mathbf{A}_{cw}\cdot\frac{\tau}{2}\right)}\cdot e^{\left(-\mathbf{A}_{fp}\cdot(TR-\tau)\right)}\cdot e^{\left(-\mathbf{A}_{cw}\cdot\frac{\tau}{2}\right)}\cdot\begin{bmatrix} S_f\cos\alpha & 0 \\ 0 & 1 \end{bmatrix}\right) \cdot\left(\mathbf{I} + e^{\left(-\mathbf{A}_{cw}\cdot\frac{\tau}{2}\right)}\cdot e^{\left(-\mathbf{A}_{fp}\cdot(TR-\tau)\right)}\right)\cdot\left(\mathbf{I} + e^{\left(-\mathbf{A}_{cw}\cdot\frac{\tau}{2}\right)}\right)\mathbf{M}_{cw}^{ss} + e^{\left(-\mathbf{A}_{cw}\cdot\frac{\tau}{2}\right)}\cdot\left(\mathbf{I} - e^{\left(-\mathbf{A}_{fp}\cdot(TR-\tau)\right)}\right)\mathbf{M}_0 \tag{A.11}$$

The final signal equation is the transverse magnetization that arises from the steady-state longitudinal magnetization. Transverse relaxation is neglected, because the signal is normalized with a volume acquired without MT :

$$M_{xy,f} = M_{z,f}\sin(\alpha)S_f \tag{A.12}$$

Equation A.12 is the signal equation from a pulse sequence with parameters $\alpha_M T$, Δ, TR and α. The MT pulse shape and duration also influences the value of W. While complex, equation A.12 is straightforward to compute numerically, as software such as Matlab can evaluate exponential matrices. The dependence on T_{1f}, F and k_f is explicit in matrices $\boldsymbol{A_{fp}}$ and $\boldsymbol{A_{cw}}$, while the dependence in T_{2f} is implicit within S_f. The dependence in T_{2r} comes from the lineshape $G(\Delta)$, which influences the value of W.

B

Removal of low SNR data in *ex situ* meniscus

This appendix describes in more detail the procedure for the removal of low SNR data in *ex situ* meniscus, which was mentioned briefly in chapter 4.

The *ex vivo* menisci datasets have very different signal intensities throughout the images due to the use of a surface coil. Therefore, the SNR shows a large variation and this results in a large fraction of QMT parameters fits that are presumed to be more biased. It was shown in previous chapters that the SNR influences largely the quality of fits.

The idea is to identify a threshold SNR in the *ex situ* datasets under which the QMT parameters from the voxels with a SNR lower than the threshold are not taken in account when calculating mean values. This is because the quality of fits is severely reduced at low SNR with Sled and Pike's model of MT. To choose a correct threshold, the distribution of the SNRs in the *in situ* and *ex situ* meniscus datasets was first evaluated. To calculate the distribution of the SNR, at each slice k, a $\approx 30\times30$ voxels noise region was selected and the standard deviation of the signal, σ_k, was calculated. Then, at each voxel (i, j) on the slice k, the SNR was evaluated as [114]

$$SNR_{i,j,k} = \frac{S_k(i,j)}{\sqrt{\frac{2}{4-\pi}}\sigma_k} \tag{B.1}$$

Where $S_k(i, j)$ is the signal, on slice k, of voxel located at indexes (i, j). The factor in front of σ_k takes in account the Rayleigh distribution of background noise in magnitude images. The distribution of noise for in situ and *ex situ* menisci (4 specimens) is shown in figure B.1. In figure B.1, a threshold SNR in red (83) was identified. It was decided that the best practice was to use similar SNRs when comparing QMT values of the *in situ* and *ex situ* menisci. Therefore, the first percentile of the SNR distribution for *in situ* menisci was chosen as the threshold and set as a minimum SNR to consider an acceptable QMT fit in the *ex situ* datasets. The first percentile was taken instead of the minimal value in case there were outliers with very low SNR in the *in situ* datasets.

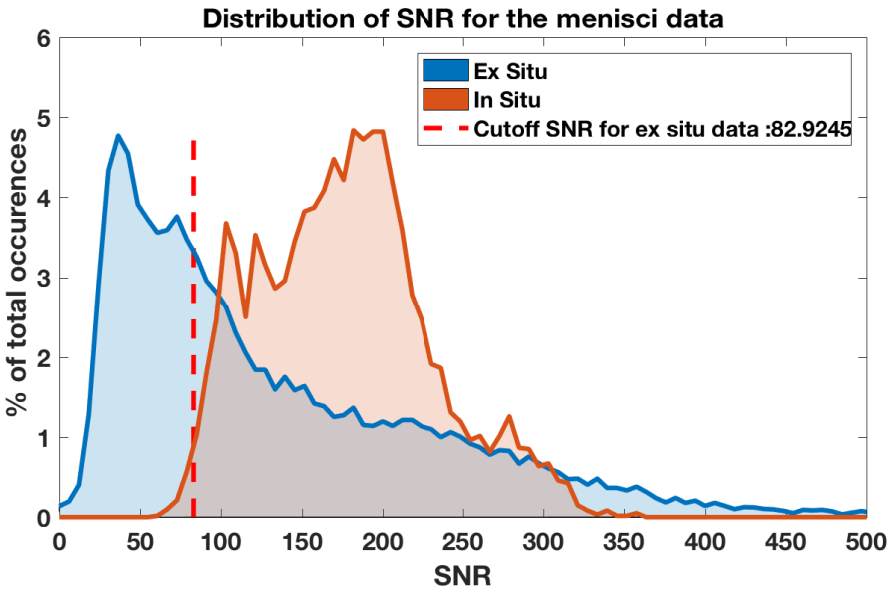

Figure B.1 – Distribution of the SNR for *in situ* and *ex situ* menisci.

Thus, only the voxels in the *ex situ* datasets which satisfy the following inequality were considered :

$$SNR_{k,ex\ situ}(i,j) \geq percentile(SNR_{\text{in situ}}, 1) \tag{B.2}$$

Where the percentile is evaluated over all voxels of all in situ samples. Figure B.2 shows the distributions of QMT parameters for the *ex situ* voxels with a voxel-wise SNR higher or lower than the threshold :

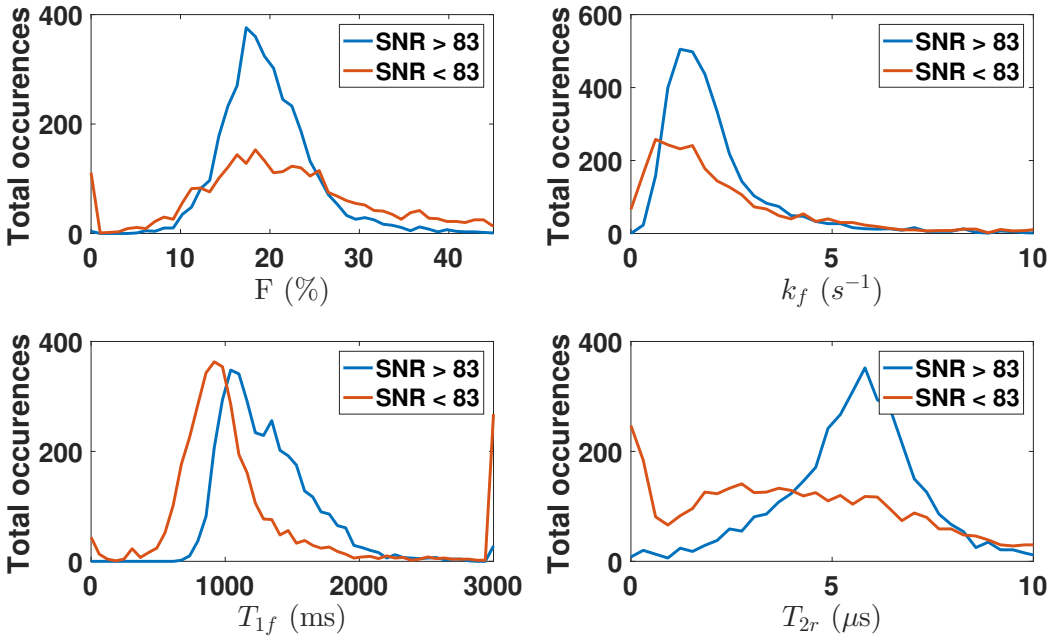

Figure B.2 – Distribution of fitted QMT parameters for the *ex situ* menisci datasets for voxels with higher and lower SNR than the selected threshold.

The first observation made from figure B.2 was that this procedure removes roughly 40% of QMT fits in the whole datasets. This is a large number, but is a consequence of the extremely non uniform SNR provided by the surface coil.

The distributions of QMT parameters for *ex situ* menisci are sharper when only considering the values with a SNR higher than the threshold. For F, a tail of large values is removed and, accordingly, this removes a large number of smaller T_{1f} values. These results support earlier conclusions from chapter 3 that using a low SNR will result in an overestimation of F. For T_{2r}, the procedure removes a very large number of low T_{2r}, which could possibly not be well fitted. For k_f, a tail of larger values and some very small values ($< 1\ \mathrm{s}^{-1}$) are removed.

Additionally, figure B.3 shows two typical slices of the *ex situ* menisci. The pixel values are not the signal intensities but the SNR. Regions where the SNR is over the threshold are superposed in red. As discussed, about 40% of the image is kept in the analysis.

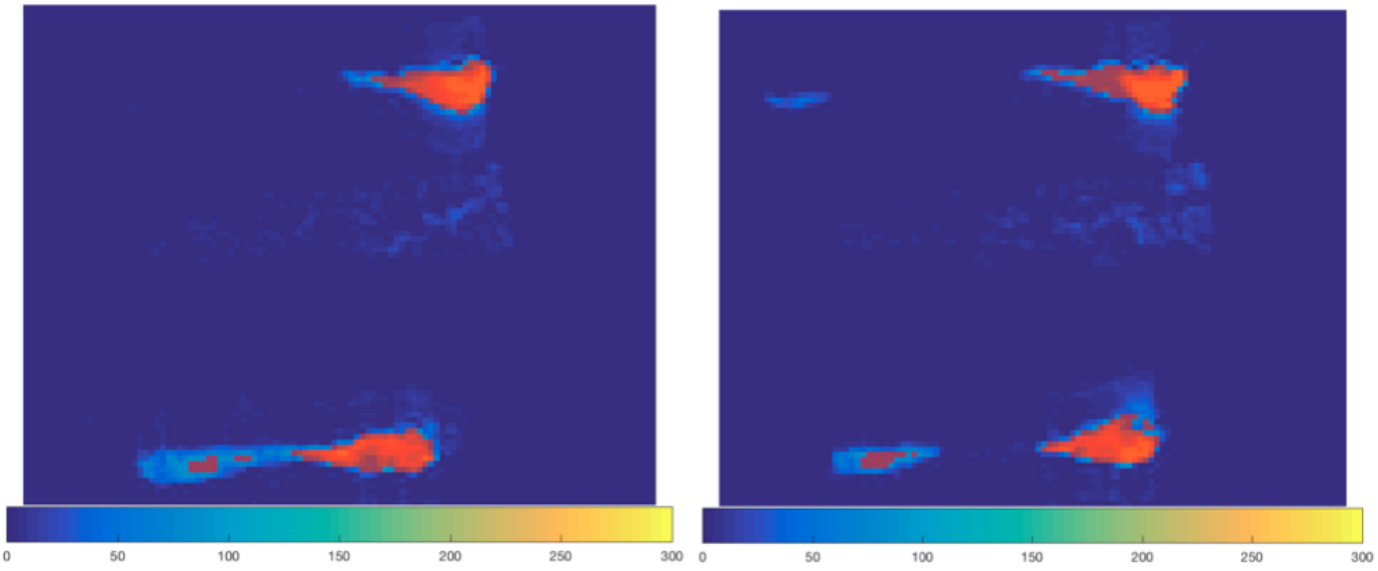

Figure B.3 – Typical SNR maps of an *ex situ* meniscus. The red area shows where the SNR is higher than the threshold.

C

T_2 values in joint tissues at 3.0 T

Here, we report T_2 values (T_{2obs}) in healthy cartilage and meniscus (with standard deviations ΔT_2 and N samples) from various sources at 3.0 T. The mean values are reported in chapter 3.

Table C.1 – T_2 values in healthy meniscus at 3 T

T_2	ΔT_2	N	ROI	Source
11.4	3.9	23	Both menisci	Rauscher et al, 2008 [109]
10.8	4.1	23	Lateral meniscus	Rauscher et al, 2008 [109]
11.8	3.5	23	Medial meniscus	Rauscher et al, 2008 [109]
11.2	1.5	23	Both menisci	Stehling et al, 2011 [112]
10.9	1.9	23	Lateral Meniscus	Stehling et al, 2011 [112]
11.5	1.9	23	Medial Meniscus	Stehling et al, 2011 [112]
11	2.5	34	Lateral Meniscus	Wang et al, 2015 [111]
11	2.5	34	Medial Meniscus	Wang et al, 2015 [111]
10.5	1.5	60	Both menisci	Chiang et al, 2013 [113]
10.1	1.5	60	Lateral Meniscus	Chiang et al, 2013 [113]
10.9	1.5	60	Medial Meniscus	Chiang et al, 2013 [113]

For cartilage, because of the broader range of T_2 values, we also report extra information about the sequence and the fitting technique used in the study when available. Some acronyms are used in table C.2. MESE : Multi Echo Spin Echo, ETL : Echo Train Length, MSME : Multi Spin Multi Echo, CPMG : Car-Purcell Meiboom Gill sequence, NLLS : non linear least squares fitting algorithm, SE : spin echo. The symbol " denotes the same extra information as the previous.

We tried to evaluate if correlations existed between T_2 and TR, T_2 and the number of TE, T_2 and the values of TE, and T_2 with the minimal or maximal TE used. No significant correlation was found. Therefore, the mean T_2 reported in chapter 3 was the average of all values in table C.2.

Table C.2 – T_2 values in healthy cartilage at 3 T

T_2	ΔT_2	N	ROI	Extra information	Source
34.7	2.4	16	Whole Cartilage	Spiral sequence, TR/TE = 2000/6.7, 12, 28,60 ms	[100]
37.8	3.3	11	Patellar Cartilage	TR/TE = 2100/13 to 150 ms.	[101]
36.9	3.81	5	Whole Cartilage	Spiral sequence, TR/TE = 3000/ 5.4, 17, 27.6, 38.3, 54.3, 102 ms	[102]
30	5	42	Patellar Cartilage	MESE, TR/TE = 1200/ 13.8, 27.6, 41.4, 55.2, 69, 82.8, NLLS	[103]
44.4	7	10	Femoral Cartilage	SE TR/TE1/TE2 3600/8.5/34.1 ms, ETL 6.	[104]
37.8	7	10	Tibial Cartilage	"	[104]
40	5	43	Femoral Cartilage	MESE, TR/TE = 1650, 12.9, 25.8, 38.7, 51.6, 65.5, 77.4 ms	[105]
33	3	450	Patellar Cartilage	MSME, TR = 2700 ms, TE = 20 - 70 ms. "Noise correction algorithm".	[106]
36	3	450	Femoral Cartilage	"	[106]
31.75	3	450	Tibial cartilage	"	[106]
30	-	10	Patellar Cartilage	Spiral sequence, TR/TE = 2000/6.7, 12, 28, 60 ms	[107]
33.8	2.8	17	Tibial Cartilage	MESE (CPMG) TR/TE = 16 * n (n = 1 .. 7) ms/4, 613 ms	[108]
27	-	23	Tibial Cartilage	Add a nonselective T2 preparation imaging sequence to SPGR. TR/TE = 2000/4.1,14.5,25.0,45.9	[109]
31	-	23	Femoral Cartilage	"	[109]
39.1	1.3	5	Whole Cartilage	MESE, TR/TE = 4500/10, 20, 40, 80,160,320,640. NLLS fitting M0, T2, T1.	[110]

D

Ethics approval for the cadaver work

Cadaver work was done at Stanford University, where no ethics is required. Only living subjects require institutional review board approval. This is stated in page 2 of the document from Stanford's Research Compliance Office available at the following url :

http://humansubjects.stanford.edu/research/documents/HSresearch_definitionsAID03H11.pdf

References

[1] J. Cohen Adad, "Principe d'imagerie biomédicale - GBM3318 - Cours 9 - Imagerie Par Résonance Magnétique," tech. rep., École Polytechnique de Montréal, 2014.

[2] R. Brown, Y. Cheng, E. Haacke, and M. Thompson, *Magnetic resonance imaging : physical principles and sequence design*. Wiley, 2014.

[3] H. Yeung, R. Adler, and S. Swanson, "longitudinal magnetization in heterogeneous spin systems under selective saturation. IV. Reformulation of the spin-bath-model equations by the Redfield-Provotorov . . . ," *Journal of Magnetic Resonance*, 1994.

[4] R. M. Henkelman, X. Huang, Q.-S. Xiang, G. J. Stanisz, S. D. Swanson, and M. J. Bronskill, "Quantitative interpretation of magnetization transfer," *Magnetic Resonance in Medicine*, vol. 29, pp. 759–766, jun 1993.

[5] S. J. Matzat, J. van Tiel, G. E. Gold, and E. H. G. Oei, "Quantitative MRI techniques of cartilage composition.," *Quantitative imaging in medicine and surgery*, vol. 3, pp. 162–74, jun 2013.

[6] N. Sritanyaratana, A. Samsonov, P. Mossahebi, J. J. Wilson, W. F. Block, and R. Kijowski, "Cross-relaxation imaging of human patellar cartilage in vivo at 3.0 T," *Osteoarthritis and Cartilage*, vol. 22, no. 10, pp. 1568–1576, 2014.

[7] N. Stikov, K. E. Keenan, J. M. Pauly, R. L. Smith, R. F. Dougherty, and G. E. Gold, "Cross-relaxation imaging of human articular cartilage," *Magnetic resonance in medicine*, vol. 66, no. 3, pp. 725–734, 2011.

[8] C. Slichter, *Principles of magnetic resonance*. Springer, 1990.

[9] G. B. Levesque, Ives R., Stikov, Nikola, Pike, "Methods for quantitative magnetization transfer imaging," in *ISMRM proceedings*, 2012.

[10] N. Bloembergen, E. M. Purcell, and R. V. Pound, "Relaxation Effects in Nuclear Magnetic Resonance Absorption," *Physical Review*, vol. 73, pp. 679–712, apr 1948.

[11] E. Insko and L. Bolinger, "Mapping of the Radiofrequency Field." 1993.

[12] L. Sacolick, F. Wiesinger, and I. Hancu, "B1 mapping by Bloch-Siegert Shift," *Magnetic Resonance in Medicine*, 2010.

[13] S. Deoni, T. Peters, and B. Rutt, "High Resolution T1 and T2 mapping of the brain in a clinically acceptable time with DESPOT1 and DESPOT2," *Magnetic Resonance in Medicine*, 2005.

[14] R. R. Ernst and W. A. Anderson, "Application of Fourier Transform Spectroscopy to Magnetic Resonance Relaxation and spectral line shape in Fourier transform ion resonance spectroscopy Application of Fourier Transform Spectroscopy to Magnetic Resonance," *J. Chem. Phys. J. Vac. Sci. Technol.*, vol. 37, no. 1, 1966.

[15] M. Gray, D. Burstein, and L. Lesperance, "Magnetization transfer in cartilage and its constituent macromolecules," *Magnetic Resonance in Medicine*, 1995.

[16] S. Koenig and R. B. III, "A molecular theory of relaxation and magnetization transfer : Application to cross-linked BSA, a model for tissue.," *Magnetic resonance in medicine*, 1993.

[17] J. G. Sled and G. B. Pike, "Quantitative imaging of magnetization transfer exchange and relaxation properties in vivo using MRI," *Magnetic Resonance in Medicine*, vol. 46, pp. 923–931, nov 2001.

[18] A. Gass, G. Barker, D. Kidd, and J. Thorpe, "Correlation of magnetization transfer ration with clinical disability in multiple sclerosis," *Annals of Neurology*, 1994.

[19] G. Pike, N. D. Stefano, S. Narayanan, and K. Worsley, "Multiple Sclerosis : Magnetization Transfer MR Imaging of White Matter before Lesion Appearance on T2-weighted Images 1," *Radiology*, 2000.

[20] M. Gloor, K. Scheffler, and O. Bieri, "Quantitative magnetization transfer imaging using balanced SSFP.," *Magnetic resonance in medicine : official journal of the Society of Magnetic Resonance in Medicine / Society of Magnetic Resonance in Medicine*, vol. 60, no. 3, pp. 691–700, 2008.

[21] D. Gochberg and J. Gore, "Quantitative imaging of magnetization transfer using an inversion recovery sequence," *Magnetic resonance in medicine*, 2003.

[22] G. Liu, X. Song, and K. Chan, "Nuts and bolts of chemical exchange saturation transfer MRI," *NMR in Biomedicine*, 2013.

[23] I. Levesque and G. Pike, "Characterizing healthy and diseased white matter using quantitative magnetization transfer and multicomponent T2 relaxometry : A unified view via a four-pool model.," *Magnetic resonance in medicine*, 2009.

[24] J. Sled, I. Levesque, A. Santos, S. Francis, S. Narayanan, S. Brass, D. Arnold, and G. Pike, "Regional variations in normal brain shown by quantitative magnetization transfer imaging," *Magnetic Resonance in Medicine*, vol. 51, pp. 299–303, feb 2004.

[25] S. Graham and R. Henkelman, "Understanding pulsed magnetization transfer," *Journal of Magnetic Resonance*, 1997.

[26] I. Lowe and R. Norberg, "Free-induction decays in solids," *Physical Review*, 1957.

[27] C. Morrison and R. M. Henkelman, "A model for magnetization transfer in tissues," *Magnetic Resonance in Medicine*, 1995.

[28] V. L. Yarnykh, "Pulsed Z-spectroscopic imaging of cross-relaxation parameters in tissues for human MRI : Theory and clinical applications," *Magnetic resonance in medicine*, vol. 47, no. 5, pp. 929–939, 2002.

[29] A. Ramani, C. Dalton, D. H. Miller, P. S. Tofts, and G. J. Barker, "Precise estimate of fundamental in-vivo MT parameters in human brain in clinically feasible times," *Magnetic Resonance Imaging*, vol. 20, pp. 721–731, 2002.

[30] D. K. Müller, A. Pampel, and H. E. Möller, "Matrix-algebra-based calculations of the time evolution of the binary spin-bath model for magnetization transfer," *Journal of Magnetic Resonance*, vol. 230, pp. 88–97, 2013.

[31] M. Cercignani and G. J. Barker, "A comparison between equations describing in vivo MT : the effects of noise and sequence parameters," *Journal of Magnetic Resonance*, vol. 191, no. 2, pp. 171–183, 2008.

[32] S. Portnoy and G. J. Stanisz, "Modeling pulsed magnetization transfer," *Magnetic Resonance in Medicine*, vol. 58, no. 1, pp. 144–155, 2007.

[33] J. Sled and G. Pike, "Quantitative interpretation of magnetization transfer in spoiled gradient echo MRI sequences," *Journal of Magnetic Resonance*, 2000.

[34] G. Caines, T. Schleich, and J. M. Rydzewski, "Incorporation of magnetization transfer into the formalism for rotating-frame spin-lattice proton NMR relaxation in the presence of an off-resonance-irradiation field," *Journal of Magnetic Resonance (1969)*, vol. 95, pp. 558–566, dec 1991.

[35] P. Mossahebi, V. L. Yarnykh, and A. Samsonov, "Analysis and correction of biases in cross-relaxation MRI due to biexponential longitudinal relaxation," *Magnetic Resonance in Medicine*, vol. 71, pp. 830–838, feb 2014.

[36] S. M. Seed, K. C. Dunican, and A. M. Lynch, "Osteoarthritis : a review of treatment options," *Formulary*, vol. 44, pp. 143–152, may 2009.

[37] K. R. Vincent, B. P. Conrad, B. J. Fregly, and H. K. Vincent, "The Pathophysiology of Osteoarthritis : A Mechanical Perspective on the Knee Joint," *PM & R : the journal of injury, function, and rehabilitation*, vol. 4, pp. S3–S9, may 2012.

[38] D. Lajeunesse, G. Hilal, J.-P. Pelletier, and J. Martel-Pelletier, "Subchondral bone morphological and biochemical alterations in osteoarthritis," *Osteoarthritis and Cartilage*, vol. 7, pp. 321–322, may 1999.

[39] D. T. Felson, R. C. Lawrence, P. A. Dieppe, R. Hirsch, C. G. Helmick, J. M. Jordan, R. S. Kington, N. E. Lane, M. C. Nevitt, Y. Zhang, M. Sowers, T. McAlindon, T. D. Spector, A. R. Poole, S. Z. Yanovski, G. Ateshian, L. Sharma, J. A. Buckwalter, K. D. Brandt, and J. F. Fries, "Osteoarthritis : New Insights. Part 1 : The Disease and Its Risk Factors," *Annals of Internal Medicine*, vol. 133, pp. 635–646, oct 2000.

[40] G. Nuki, "Osteoarthritis : a problem of joint failure," *Zeitschrift für Rheumatologie*, vol. 58, pp. 142–147, jun 1999.

[41] V. C. Mow, M. H. Holmes, and W. Michael Lai, "Fluid transport and mechanical properties of articular cartilage : A review," *Journal of Biomechanics*, vol. 17, no. 5, pp. 377–394, 1984.

[42] J. A. Buckwalter and H. J. Mankin, "Articular cartilage : degeneration and osteoarthritis, repair, regeneration, and transplantation.," *Instructional course lectures*, vol. 47, pp. 487–504, 1997.

[43] M. Venn and A. Maroudas, "Chemical composition and swelling of normal and osteoarthrotic femoral head cartilage. I. Chemical composition.," *Annals of the Rheumatic Diseases*, vol. 36, no. 2, pp. 121–129, 1977.

[44] G. R. Squires, S. Okouneff, M. Ionescu, and A. R. Poole, "The pathobiology of focal lesion development in aging human articular cartilage and molecular matrix changes characteristic of osteoarthritis," *Arthritis & Rheumatism*, vol. 48, no. 5, pp. 1261–1270, 2003.

[45] R. C. Billinghurst, L. Dahlberg, M. Ionescu, A. Reiner, R. Bourne, C. Rorabeck, P. Mitchell, J. Hambor, O. Diekmann, H. Tschesche, and Others, "Enhanced cleavage of type II collagen by collagenases in osteoarthritic articular cartilage.," *Journal of Clinical Investigation*, vol. 99, no. 7, p. 1534, 1997.

[46] D. A. Binks, R. J. Hodgson, M. E. Ries, R. J. Foster, S. W. Smye, D. McGonagle, and A. Radjenovic, "Quantitative parametric MRI of articular cartilage : a review of progress and open challenges," *The British journal of radiology*, vol. 86, no. 1023, p. 20120163, 2013.

[47] M. Englund, A. Guermazi, and L. S. Lohmander, "The Meniscus in Knee Osteoarthritis," *Rheumatic Disease Clinics of North America*, vol. 35, pp. 579–590, aug 2009.

[48] A. J. Fox, A. Bedi, and S. A. Rodeo, "The basic science of human knee menisci structure, composition, and function," *Sports Health : A Multidisciplinary Approach*, vol. 4, no. 4, pp. 340–351, 2012.

[49] C. Ding, F. Cicuttini, and G. Jones, "How important is MRI for detecting early osteoarthritis ?," *Nature Clinical Practice Rheumatology*, vol. 4, no. 1, pp. 4–5, 2008.

[50] U. Duvvuri, R. Reddy, S. D. Patel, J. H. Kaufman, J. B. Kneeland, and J. S. Leigh, "T1ρ-relaxation in articular cartilage : Effects of enzymatic degradation," *Magnetic resonance in medicine*, vol. 38, no. 6, pp. 863–867, 1997.

[51] S. V. Akella, R. Reddy Regatte, A. J. Gougoutas, A. Borthakur, E. M. Shapiro, J. B. Kneeland, J. S. Leigh, and R. Reddy, "Proteoglycan-induced changes in T1ρ-relaxation of articular cartilage at 4T," *Magnetic resonance in medicine*, vol. 46, no. 3, pp. 419–423, 2001.

[52] W. R. Witschey, A. Borthakur, M. Fenty, B. J. Kneeland, J. H. Lonner, E. L. McArdle, M. Sochor, and R. Reddy, "T1ρ MRI quantification of arthroscopically confirmed cartilage degeneration," *Magnetic Resonance in Medicine*, vol. 63, no. 5, pp. 1376–1382, 2010.

[53] S. V. Akella, R. R. Regatte, A. J. Wheaton, A. Borthakur, and R. Reddy, "Reduction of residual dipolar interaction in cartilage by spin-lock technique," *Magnetic resonance in medicine*, vol. 52, no. 5, pp. 1103–1109, 2004.

[54] A. Bashir, M. L. Gray, and D. Burstein, "Gd-DTPA2- as a measure of cartilage degradation," *Magnetic resonance in medicine*, vol. 36, no. 5, pp. 665–673, 1996.

[55] A. Williams, L. Sharma, C. A. McKenzie, P. V. Prasad, and D. Burstein, "Delayed gadolinium-enhanced magnetic resonance imaging of cartilage in knee osteoarthritis : Findings at different radiographic stages of disease and relationship to malalignment," *Arthritis & Rheumatism*, vol. 52, no. 11, pp. 3528–3535, 2005.

[56] T. C. B. Pollard, E. G. McNally, D. C. Wilson, D. R. Wilson, B. Mädler, M. Watson, H. S. Gill, and A. J. Carr, "Localized cartilage assessment with three-dimensional dGEMRIC in asymptomatic hips with normal morphology and cam deformity," *J Bone Joint Surg Am*, vol. 92, no. 15, pp. 2557–2569, 2010.

[57] A. Borthakur, E. Mellon, S. Niyogi, W. Witschey, J. B. Kneeland, and R. Reddy, "Sodium and T1ρ MRI for molecular and diagnostic imaging of articular cartilage," *NMR in Biomedicine*, vol. 19, no. 7, pp. 781–821, 2006.

[58] B. Schmitt, S. Zbyn, D. Stelzeneder, V. Jellus, D. Paul, L. Lauer, P. Bachert, and S. Trattnig, "Cartilage quality assessment by using glycosaminoglycan chemical exchange saturation transfer and 23Na MR imaging at 7 T," *Radiology*, vol. 260, no. 1, pp. 257–264, 2011.

[59] R. Reddy, E. K. Insko, E. A. Noyszewski, R. Dandora, J. B. Kneeland, and J. S. Leigh, "Sodium MRI of human articular cartilage in vivo," *Magnetic resonance in medicine*, vol. 39, no. 5, pp. 697–701, 1998.

[60] A. Borthakur, E. M. Shapiro, J. Beers, S. Kudchodkar, J. B. Kneeland, and R. Reddy, "Sensitivity of MRI to proteoglycan depletion in cartilage : comparison of sodium and proton MRI," *Osteoarthritis and Cartilage*, vol. 8, no. 4, pp. 288–293, 2000.

[61] E. M. Shapiro, A. Borthakur, A. Gougoutas, and R. Reddy, "23Na MRI accurately measures fixed charge density in articular cartilage," *Magnetic Resonance in Medicine*, vol. 47, no. 2, pp. 284–291, 2002.

[62] P. van Zijl and N. N. Yadav, "Chemical exchange saturation transfer (CEST) : what is in a name and what isn't ?," *Magnetic resonance in medicine*, vol. 65, no. 4, pp. 927–948, 2011.

[63] K. M. Ward, A. H. Aletras, and R. S. Balaban, "A new class of contrast agents for MRI based on proton chemical exchange dependent saturation transfer (CEST)," *Journal of magnetic resonance*, vol. 143, no. 1, pp. 79–87, 2000.

[64] W. Ling, R. R. Regatte, G. Navon, and A. Jerschow, "Assessment of glycosaminoglycan concentration in vivo by chemical exchange-dependent saturation transfer (gagCEST)," *Proceedings of the National Academy of Sciences*, vol. 105, no. 7, pp. 2266–2270, 2008.

[65] B. J. Dardzinski, T. J. Mosher, S. Li, M. A. Van Slyke, and M. B. Smith, "Spatial variation of T2 in human articular cartilage.," *Radiology*, vol. 205, no. 2, pp. 546–550, 1997.

[66] T. C. Dunn, Y. Lu, H. Jin, M. D. Ries, and S. Majumdar, "T2 Relaxation Time of Cartilage at MR Imaging : Comparison with Severity of Knee Osteoarthritis 1," *Radiology*, vol. 232, no. 2, pp. 592–598, 2004.

[67] C. Stehling, H. Liebl, R. Krug, N. E. Lane, M. C. Nevitt, J. Lynch, C. E. McCulloch, and T. M. Link, "Patellar Cartilage : T2 values and morphologic abnormalities at 3.0-T MR imaging in relation to physical activity in asymptomatic subjects from the osteoarthritis initiative 1," *Radiology*, vol. 254, no. 2, pp. 509–520, 2010.

[68] D. Burstein, M. L. Gray, A. L. Hartman, R. Gipe, and B. D. Foy, "Diffusion of small solutes in cartilage as measured by nuclear magnetic resonance (NMR) spectroscopy and imaging," *Journal of orthopaedic research*, vol. 11, no. 4, pp. 465–478, 1993.

[69] V. Mlynarik, I. Sulzbacher, M. Bittsansky, R. Fuiko, and S. Trattnig, "Investigation of apparent diffusion constant as an indicator of early degenerative disease in articular cartilage," *Journal of Magnetic Resonance Imaging*, vol. 17, no. 4, pp. 440–444, 2003.

[70] K. L. Miller, B. A. Hargreaves, G. E. Gold, and J. M. Pauly, "Steady-state diffusion-weighted imaging of in vivo knee cartilage," *Magnetic resonance in medicine*, vol. 51, no. 2, pp. 394–398, 2004.

[71] K. M. Friedrich, T. C. Mamisch, C. Plank, G. Langs, S. Marlovits, E. Salomonowitz, S. Trattnig, and G. Welsch, "Diffusion-weighted imaging for the follow-up of patients after matrix-associated autologous chondrocyte transplantation," *European journal of radiology*, vol. 73, no. 3, pp. 622–628, 2010.

[72] S. K. De Visser, R. W. Crawford, and J. M. Pope, "Structural adaptations in compressed articular cartilage measured by diffusion tensor imaging," *Osteoarthritis and Cartilage*, vol. 16, no. 1, pp. 83–89, 2008.

[73] D. M. Pierce, W. Trobin, J. G. Raya, S. Trattnig, H. Bischof, C. Glaser, and G. A. Holzapfel, "DT-MRI based computation of collagen fiber deformation in human articular cartilage : a feasibility study," *Annals of biomedical engineering*, vol. 38, no. 7, pp. 2447–2463, 2010.

[74] M. J. Nissi, J. Rieppo, J. Töyräs, M. S. Laasanen, I. Kiviranta, J. S. Jurvelin, and M. T. Nieminen, "T 2 relaxation time mapping reveals age-and species-related diversity of collagen network architecture in articular cartilage," *Osteoarthritis and cartilage*, vol. 14, no. 12, pp. 1265–1271, 2006.

[75] Y. Xia, "Magic-angle effect in magnetic resonance imaging of articular cartilage : a review," *Investigative radiology*, vol. 35, no. 10, pp. 602–621, 2000.

[76] S. Zheng and Y. Xia, "Effect of phosphate electrolyte buffer on the dynamics of water in tendon and cartilage," *NMR in biomedicine*, vol. 22, no. 2, pp. 158–164, 2009.

[77] D. K. Kim, T. L. Ceckler, V. C. Hascall, A. Calabro, and R. S. Balaban, "Analysis of water-macromolecule proton magnetization transfer in articular cartilage," *Magnetic resonance in medicine*, vol. 29, no. 2, pp. 211–215, 1993.

[78] M. L. Gray, D. Burstein, L. M. Lesperance, and L. Gehrke, "Magnetization transfer in cartilage and its constituent macromolecules," *Magnetic resonance in medicine*, vol. 34, no. 3, pp. 319–325, 1995.

[79] P.-J. Lattanzio, K. W. Marshall, A. Z. Damyanovich, and H. Peemoeller, "Macromolecule and water magnetization exchange modeling in articular cartilage," *Magnetic resonance in medicine*, vol. 44, no. 6, pp. 840–851, 2000.

[80] H. T. Edzes and E. T. Samulski, "Cross relaxation and spin diffusion in the proton NMR of hydrated collagen," *Nature*, 1977.

[81] W. Li, L. Hong, G. Zhang, and R. Magin, "Quantitative magnetization transfer imaging for evaluating the tissue-engineered cartilage," in *Proc. Intl. Soc. Mag. Reson. Med.*, vol. 16, p. 1716, 2008.

[82] W. Li, J. Li, C. Muehleman, and R. Magin, "Reduction of the magic angle effect on contrast in magnetization transfer imaging of human cartilage," in *Proc. Intl. Soc. Mag. Reson. Med.*, vol. 17, p. 3963, 2009.

[83] V. L. Yarnykh and C. Yuan, "Cross-relaxation imaging reveals detailed anatomy of white matter fiber tracts in the human brain," *Neuroimage*, vol. 23, no. 1, pp. 409–424, 2004.

[84] H. R. Underhill, C. Yuan, and V. L. Yarnykh, "Direct quantitative comparison between cross-relaxation imaging and diffusion tensor imaging of the human brain at 3.0 T," *NeuroImage*, vol. 47, no. 4, pp. 1568–1578, 2009.

[85] M. Cercignani and D. C. Alexander, "Optimal acquisition schemes for in vivo quantitative magnetization transfer MRI," *Magnetic resonance in medicine*, vol. 56, no. 4, pp. 803–810, 2006.

[86] F. Liu, R. Chaudhary, W. F. Block, A. Samsonov, and R. Kijowski, "Multicomponent T 2 analysis of articular cartilage with synovial fluid partial volume correction," *Journal of Magnetic Resonance Imaging*, pp. n/a–n/a, oct 2015.

[87] F. Liu, A. Samsonov, J. J. Wilson, D. G. Blankenbaker, W. F. Block, and R. Kijowski, "Rapid in vivo multicomponent T2 mapping of human knee menisci," *Journal of Magnetic Resonance Imaging*, vol. 42, pp. n/a–n/a, nov 2015.

[88] D. A. Reiter, P.-C. Lin, K. W. Fishbein, and R. G. Spencer, "Multicomponent T2 relaxation analysis in cartilage," *Magnetic Resonance in Medicine*, vol. 61, pp. 803–809, apr 2009.

[89] F. Liu, W. F. Block, R. Kijowski, and A. Samsonov, "Rapid multicomponent relaxometry in steady state with correction of magnetization transfer effects," *Magnetic Resonance in Medicine*, vol. 75, pp. 1423–1433, apr 2016.

[90] S. Deoni, B. Rutt, and T. Arun, "Gleaning multicomponent T1 and T2 information from steady state imaging data," *Magnetic Resonance*, 2008.

[91] E. Y. Chang, "Evaluation of Meniscal Pathology Using Quantitative Magnetic Resonance Imaging," in *Proc. Intl. Soc. Magn. Reson. Med.*, vol. 23, 2015.

[92] E. Wiener, C. W. A. Pfirrmann, and J. Hodler, "Spatial variation in T1 of healthy human articular cartilage of the knee joint," *The British journal of radiology*, vol. 83, pp. 476–485, 2010.

[93] E. Wiener, K. Woertler, G. Weirich, E. J. Rummeny, and M. Settles, "Contrast enhanced cartilage imaging : comparison of ionic and non-ionic contrast agents," *European journal of radiology*, vol. 63, no. 1, pp. 110–119, 2007.

[94] M. J. Nissi, J. Rieppo, J. Töyräs, M. S. Laasanen, I. Kiviranta, M. T. Nieminen, and J. S. Jurvelin, "Estimation of mechanical properties of articular cartilage with MRI–dGEMRIC, T 2 and T 1 imaging in different species with variable stages of maturation," *Osteoarthritis and Cartilage*, vol. 15, no. 10, pp. 1141–1148, 2007.

[95] I. Hannila, S. S. Räinä, O. Tervonen, R. Ojala, and M. T. Nieminen, "Topographical variation of T2 relaxation time in the young adult knee cartilage at 1.5 T," *Osteoarthritis and Cartilage*, vol. 17, no. 12, pp. 1570–1575, 2009.

[96] E. Lammentausta, P. Kiviranta, J. Töyräs, I. Kiviranta, M. T. Nieminen, and J. S. Jurvelin, "Degeneration-induced depth-wise variation in T2 relaxation time of human patellar cartilage at 1.5 T," in *Proc. Intl. Soc. Mag. Reson. Med.*, 2007.

[97] I. R. Levesque, J. G. Sled, and G. B. Pike, "Iterative optimization method for design of quantitative magnetization transfer imaging experiments," *Magnetic resonance in medicine*, vol. 66, no. 3, pp. 635–643, 2011.

[98] S. C. Deoni, T. M. Peters, and B. K. Rutt, "Determination of optimal angles for variable nutation proton magnetic spin-lattice, T1, and spin-spin, T2, relaxation times measurement," *Magnetic resonance in medicine*, vol. 51, no. 1, pp. 194–199, 2004.

[99] R. Stollberger and P. Wach, "Imaging of the active B1 field in vivo," *Magnetic Resonance in Medicine*, vol. 35, no. 2, pp. 246–251, 1996.

[100] L. Xiaojuan, M. Benjamin, L. Thomas, and Others, "In vivo T1Rho and T2 mapping of articular cartilage in osteoarthritis of the knee using 3 tesla MRI," *Osteoarthritis Cartilage*, vol. 15, pp. 789–797, 2007.

[101] W. Yao, N. Qu, Z. Lu, and S. Yang, "The application of T1 and T2 relaxation time and magnetization transfer ratios to the early diagnosis of patellar cartilage osteoarthritis," *Skeletal radiology*, vol. 38, no. 11, pp. 1055–1062, 2009.

[102] G. E. Gold, E. Han, J. Stainsby, G. Wright, J. Brittain, and C. Beaulieu, "Musculoskeletal MRI at 3.0 T : relaxation times and image contrast," *American Journal of Roentgenology*, vol. 183, no. 2, pp. 343–351, 2004.

[103] S. Apprich, T. C. Mamisch, G. H. Welsch, D. Stelzeneder, C. Albers, U. Totzke, and S. Trattnig, "Quantitative T2 mapping of the patella at 3.0 T is sensitive to early cartilage degeneration, but also to loading of the knee," *European journal of radiology*, vol. 81, no. 4, pp. e438–e443, 2012.

[104] R. Stahl, G. Blumenkrantz, J. Carballido-Gamio, S. Zhao, T. Munoz, M. H. Le Graverand-Gastineau, X. Li, S. Majumdar, and T. M. Link, "MRI-derived T2 relaxation times and cartilage morphometry of the tibio-femoral joint in subjects with and without osteoarthritis during a 1-year follow-up," *Osteoarthritis and Cartilage*, vol. 15, no. 11, pp. 1225–1234, 2007.

[105] S. Apprich, G. H. Welsch, T. C. Mamisch, P. Szomolanyi, M. Mayerhoefer, K. Pinker, and S. Trattnig, "Detection of degenerative cartilage disease : comparison of high-resolution morphological MR and quantitative T2 mapping at 3.0 Tesla," *Osteoarthritis and Cartilage*, vol. 18, no. 9, pp. 1211–1217, 2010.

[106] G. B. Joseph, C. E. McCulloch, M. C. Nevitt, U. Heilmeier, L. Nardo, J. A. Lynch, F. Liu, T. Baum, and T. M. Link, "A reference database of cartilage 3 T MRI T2 values in knees without diagnostic evidence of cartilage degeneration : data from the osteoarthritis initiative," *Osteoarthritis and Cartilage*, vol. 23, no. 6, pp. 897–905, 2015.

[107] X. Li, A. Pai, G. Blumenkrantz, J. Carballido-Gamio, T. Link, B. Ma, M. Ries, and S. Majumdar, "Spatial distribution and relationship of T1ρ and T2 relaxation times in knee cartilage with osteoarthritis," *Magnetic resonance in medicine*, vol. 61, no. 6, pp. 1310–1318, 2009.

[108] H. Nishioka, J. Hirose, E. Nakamura, Y. Oniki, K. Takada, Y. Yamashita, and H. Mizuta, "T1ρ and T2 mapping reveal the in vivo extracellular matrix of articular cartilage," *Journal of Magnetic Resonance Imaging*, vol. 35, no. 1, pp. 147–155, 2012.

[109] I. Rauscher, R. Stahl, J. Cheng, X. Li, M. B. Huber, A. Luke, S. Majumdar, and T. M. Link, "Meniscal Measurements of T1ρ and T2 at MR Imaging in Healthy Subjects and Patients with Osteoarthritis 1," *Radiology*, vol. 249, no. 2, pp. 591–600, 2008.

[110] C. D. Jordan, M. Saranathan, N. K. Bangerter, B. A. Hargreaves, and G. E. Gold, "Musculoskeletal MRI at 3.0 T and 7.0 T : a comparison of relaxation times and image contrast," *European journal of radiology*, vol. 82, no. 5, pp. 734–739, 2013.

[111] A. Wang, V. Pedoia, F. Su, E. Abramson, M. Kretzschmar, L. Nardo, T. M. Link, C. E. McCulloch, C. Jin, C. B. Ma, and Others, "MR T1ρ and T2 of meniscus after acute anterior cruciate ligament injuries," *Osteoarthritis and Cartilage*, 2015.

[112] C. Stehling, A. Luke, R. Stahl, T. Baum, G. Joseph, J. Pan, and T. M. Link, "Meniscal T1rho and T2 measured with 3.0 T MRI increases directly after running a marathon," *Skeletal radiology*, vol. 40, no. 6, pp. 725–735, 2011.

[113] S.-W. Chiang, P.-H. Tsai, Y.-C. Chang, C.-Y. Wang, H.-W. Chung, H.-S. Lee, M.-C. Chou, Y.-C. Hsu, and G.-S. Huang, "T2 values of posterior horns of knee menisci in asymptomatic subjects," *PLOS one*, vol. 8, no. 3, p. e59769, 2013.

[114] O. Dietrich, J. G. Raya, S. B. Reeder, M. F. Reiser, and S. O. Schoenberg, "Measurement of Signal-to-Noise Ratios in MR Images : Influence of Multichannel Coils, Parallel Imaging, and Reconstruction Filters," *Journal of Magnetic Resonance Imaging*, vol. 26, pp. 375–385, 2007.

[115] M. E. Mayerhoefer, G. Riegler, G. H. Welsch, T. C. Mamisch, M. Weber, and S. Trattnig, "The in vivo effects of unloading and compression on T1-Gd (dGEMRIC) relaxation times in healthy articular knee cartilage at 3.0 Tesla," (C-2249), 2010.

[116] E. A. Makris, P. Hadidi, and K. A. Athanasiou, "The knee meniscus : structure–function, pathophysiology, current repair techniques, and prospects for regeneration," *Biomaterials*, vol. 32, no. 30, pp. 7411–7431, 2011.

[117] G. J. Stanisz, E. E. Odrobina, J. Pun, M. Escaravage, S. J. Graham, M. J. Bronskill, and R. M. Henkelman, "T1, T2 relaxation and magnetization transfer in tissue at 3T," *Magnetic Resonance in Medicine*, vol. 54, no. 3, pp. 507–512, 2005.

[118] V. Mow and R. Huiskes, *Basic orthopaedic biomechanics & mechano-biology*. 2005.

[119] L. Pronzato and A. Pázman, "Design of experiments in nonlinear models," *Lecture notes in statistics*, 2013.

[120] M. Berger and H. Silverman, "Microphone array optimization by stochastic region contraction," *IEEE Transactions on Signal*, 1991.

[121] S. C. Deoni and S. H. Kolind, "Investigating the stability of mcDESPOT myelin water fraction values derived using a stochastic region contraction approach," *Magnetic Resonance in Medicine*, vol. 73, pp. 161–169, jan 2015.

[122] R. Horch, J. Gore, and M. Does, "Origins of the ultrashort T21H NMR signals in myelinated nerve : A direct measure of myelin content ?," *Magnetic resonance in Medicine*, 2011.